Fermilab FERMILAB-THESIS-1999-20

A Dalitz Analysis of the Decay $D_s^+ \to \pi^+\pi^-\pi^+$

Scott Allan Radeztsky

Under the supervision of Professor Francis Halzen
and Senior Scientist Emerita Marleigh Sheaff
At the University of Wisconsin–Madison

Fermilab experiment E791 took data during six months in 1991 using a 500 GeV π^- beam on platinum and diamond targets for the purpose of studying the production and decay of particles containing a charm quark. In this dissertation, a set of events with a well-separated three-track secondary vertex were extracted from the E791 data set. A Dalitz analysis is performed on the events consistent with coming from the decay $D_s^+ \to \pi^+\pi^-\pi^+$ (and charge conjugate). A model for the Dalitz analysis using the Zemach Formalism was presented, and a maximum likelihood fit was performed. From the fit, amplitudes and phases from the coherent sum of signal resonances were obtained, and the decay fractions for the resonances were extracted. Results presented include the obtained amplitudes, phases and fractions, as well as an improved measurement of the mass and width of the $f_0(980)$ and $f_0(1370)$ scalar resonances.

Acknowledgments

The moon moves slowly, but it crosses the town.

1962 – 1999
Thanks, everyone.
For picking me up, for keeping me up, and for putting up with me.
I couldn't have done this without you.

CONTENTS

Abstract i
Acknowledgement ii

1. Introduction to the Analysis 1
1.1 Introduction and Overview 1
1.2 Measurement to be Made 4

2. Beamline and Spectrometer 8
2.1 Introduction and Overview 8
2.2 Beam 9
2.3 Target 11
2.4 TPL Spectrometer 14
2.5 E791 Coordinate System 15
2.6 Upstream Tracking of the Beam Particle 16
2.6.1 Beam Track Proportional Wire Chambers 16
2.6.2 The Beam Silicon Microstrip Detectors 17
2.7 Downstream Charged Particle Tracking 19
2.7.1 The Downstream SMDs 19
2.7.2 The Drift Chambers and Analysis Magnets 23
2.8 Particle Identification 27
2.8.1 The Čerenkov Detector 27
2.8.2 The Calorimeters 28

3. Event Trigger and Data Acquisition System 29
3.1 Introduction and Overview 29
3.2 The E791 Trigger 30
3.2.1 The Pretrigger Logic 30
3.2.2 The E_t and E_{tot} Trigger Logic 30
3.3 The E791 Data Acquisition System 31

4. The E791 Monte Carlo 35
4.1 Introduction and Overview 35
4.2 Modeling the Events and Spectrometer 35
4.3 Uses of the E791 Monte Carlo 37

5. Event Reconstruction and Filtering 39
5.1 Introduction and Overview 39
5.2 General Track Reconstruction Methodology 41
5.3 Vertex Reconstruction 43
5.4 Definition of Cuts 44
5.4.1 The SDZ Cut 45
5.4.2 The DIP Cut 46
5.4.3 The PTB Cut 47
5.4.4 The SIGMA Cut 47
5.4.5 The PISO Cut 48
5.4.6 The PISE Cut 48
5.4.7 The RATIO Cut 49
5.5 Filtering and Stripping 50

6. Event Selection for the Analysis 52
6.1 Introduction and Overview 52
6.2 Motivation of Cut Selection Methodology 52
6.3 Final Cut Selection Methodology 53
6.4 Final Cut Selection 65
6.5 Background Studies 65
6.5.1 Visible Structure in the D_s Mass Plot 67
6.5.2 Visible Structure in the Background Dalitz Plot . . . 68
6.5.3 Analysis of Visible Structure in Background Dalitz Plot 69
6.5.4 Other Sources of Charm Background 85
6.5.5 Sum of Contributions of Background Sources 88

7. The Maximum Likelihood Fitting Technique 90
7.1 Introduction and Overview 90
7.2 Resonant Mass Distributions 91
7.3 Maximum Likelihood Function 93
7.3.1 Signal Probability Distribution Function. 93
7.3.2 Background Probability Distribution 94
7.3.3 Form of the Likelihood Function 95

7.3.4 Evaluation of Integrals 96
7.3.5 Normalized Physical Fractions 97
7.4 Signal Matrix Elements 98
7.4.1 Breit Wigner Functions 99
7.4.2 Form Factors 99
7.4.3 Angular Distributions 100
7.4.4 Symmetrization of the Signal Amplitudes 101
7.5 Background Amplitudes 101

8. The Maximum Likelihood Fit Implementation 102
8.1 Introduction and Overview 102
8.2 Signal PDF 102
8.3 Background PDF 105
8.4 Efficiency Calculation 108
8.5 Fit Formalism 115
8.6 Fit Results 117
8.7 Goodness of Fit 120

9. Measurement Errors 123
9.1 Introduction and Overview 123
9.2 Check of Statistical Errors Reported by MINUIT 123
9.3 Systematic Studies 124
9.3.1 Variation of Background Exponential 126
9.3.2 Variation of Blatt Weisskopf Form Factors 130
9.3.3 Bins of D_s Charge 131
9.3.4 Bins of D_s Momentum 132
9.3.5 Bins of D_s Transverse Momentum 134
9.3.6 Removal of Edge Bins 136
9.3.7 Varying Mass and Width of $f_0(980)$ 137
9.3.8 Varying Mass and Width of $f_0(1370)$ 139

10. Conclusions 141
10.1 Introduction and Overview 141
10.2 Comparison of Results With Published Measurements 141
10.3 Final Remarks 143

LIST OF TABLES

2.1 E791 Target Information 11
2.2 E791 Proportional Wire Chambers 17
2.3 E791 Beam Tracking SMD Planes 18
2.4 E791 Downstream SMD Planes 22
2.5 E791 Magnets 23
2.6 E791 Drift Chambers 25

3.1 E791 Front End Digitization Systems and Read Out Controllers 34

5.1 E791 Track Categories 43
5.2 Summary of Cuts at Each Stage of the Analysis 51

6.1 Final Analysis Cut Values 66
6.2 Track Matching Criteria 70
6.3 Summary of Surviving Monte Carlo Events in Dalitz Corner Plots 72
6.4 Calculated Number of Expected Background Events in Data Dalitz Corner Plot 84

7.1 Properties of Possible Intermediate Resonances 91
7.2 Zemach Amplitudes for the decay $D \to r\pi_3 \to \pi_1\pi_2\pi_3$ 101

8.1 Final Solution 117
8.2 Second Final Solution 117
8.3 Final Solution—Tight Cuts 118
8.4 Second Final Solution—Tight Cuts 119
8.5 Fit Background Fractions and Resonance Masses and Widths 120

9.1 Final Result with Statistic and Systematic Errors 125
9.2 Fit Result With Exponential Slope Fixed at –5.434 127
9.3 Fit Result With Exponential Slope Fixed at –6.090 127
9.4 Fit Result With 19.8% D^0 Background 128

9.5 Fit Result With 17.6% D^0 Background 128
9.6 Fit Result With 5.8% $D_s \to \eta'\pi$ Background 129
9.7 Fit Result With 4.6% $D_s \to \eta'\pi$ Background 129
9.8 Fit Result With $F_D = 1$ and $F_r = 1$ 130
9.9 Fit Result For D_s^+ 131
9.10 Fit Result For D_s^- 131
9.11 Fit Result For $0\ GeV/c^2 < P_{D_s} < 39\ GeV/c^2$ 132
9.12 Fit Result For $39\ GeV/c^2 \leq P_{D_s} < 62\ GeV/c^2$ 133
9.13 Fit Result For $P_{D_s} \geq 62\ GeV/c^2$ 133
9.14 Fit Result For $0\ GeV/c \leq P_t < 0.65\ GeV/c$ 134
9.15 Fit Result For $0.65\ GeV/c \leq P_t < 1.15\ GeV/c$ 135
9.16 Fit Result For $P_t \geq 1.15\ GeV/c$ 135
9.17 Fit Result Removing Edge Bins 136
9.18 Fit Result For $f_0(980)$ Mass at 0.975 GeV/c^2 137
9.19 Fit Result For $f_0(980)$ Mass at 0.983 GeV/c^2 137
9.20 Fit Result For $f_0(980)$ Width at 0.035 GeV/c^2 138
9.21 Fit Result For $f_0(980)$ Width at 0.045 GeV/c^2 138
9.22 Fit Result For $f_0(1370)$ Mass at 1.422 GeV/c^2 139
9.23 Fit Result For $f_0(1370)$ Mass at 1.460 GeV/c^2 139
9.24 Fit Result For $f_0(1370)$ Width at 0.136 GeV/c^2 140
9.25 Fit Result For $f_0(1370)$ Width at 0.194 GeV/c^2 140

10.1 Comparison of Thesis Results With Published Measurements 142
10.2 Presentation of the $f_0(980)$ and $f_0(1370)$ Mass and Width . . 143

LIST OF FIGURES

1.1 Diagrams for $D_s^+ \to \pi^+\pi^-\pi^+$ final states 2
1.2 Final Sample Three Pion Mass Hypothesis 5
1.3 Final Sample Dalitz Plot 6

2.1 Beamline Schematic to TPL 9
2.2 Particle selection using magnetic field and collimator 10
2.3 E791 Target Configuration Schematic (not to scale) 12
2.4 E791 Vertex Reconstruction 13
2.5 The E791 Spectrometer 14
2.6 E791 SMD View Directions 19
2.7 Downstream SMD Layout and Track Hits 20
2.8 Double Hit Ambiguity 26

3.1 E791 Data Acquisition System 33

5.1 E791 Data Reduction Stages 40
5.2 Schematic of SDZ Cut Variable 45
5.3 Schematic of DIP Cut Variable 46
5.4 Schematic of PTB Cut Variable 47
5.5 Schematic of SIGMA Cut Variable 48
5.6 Schematic of PISO Cut Variable 49

6.1 Data $\pi^+\pi^-\pi^+$ Mass Hypothesis 54
6.2 Final Cut Selection Dependence on SDZ 56
6.3 Final Cut Selection Dependence on PTB 57
6.4 Final Cut Selection Dependence on SIGMA 58
6.5 Final Cut Selection Dependence on RATIO 59
6.6 Final Cut Selection Dependence on D_s lifetime 60
6.7 Final Cut Selection Dependence on Minimum Decay Track χ^2 Contribution to Primary Vertex 61

6.8 Final Cut Selection Dependence on Event Primary Vertex Multiplicity 62
6.9 Final Cut Selection Dependence on PISO 63
6.10 Final Cut Selection Dependence on PISE 64
6.11 Data $D^+ \to K^-\pi^+\pi^+$ events, plotted as $\pi^+\pi^-\pi^+$ events, after Final Selection Cuts 67
6.12 E791 Data Events in the Dalitz Corners for Signal, Midwing and Highwing Regions 71
6.13 Monte Carlo $D^* \to D^0\pi, D^0 \to K\pi$ Events in the Dalitz Corners for Signal, Midwing and Highwing Regions 73
6.14 Monte Carlo $D^0 \to K\pi$ (no D^*) Events in the Dalitz Corners for Signal, Midwing and Highwing Regions 74
6.15 Monte Carlo $D^0 \to Ke\nu$ Events in the Dalitz Corners for Signal, Midwing and Highwing Regions 75
6.16 Monte Carlo $D^0 \to K\mu\nu$ Events in the Dalitz Corners for Signal, Midwing and Highwing Regions 76
6.17 Monte Carlo $D^0 \to \pi\pi$ Events in the Dalitz Corners for Signal, Midwing and Highwing Regions 77
6.18 Monte Carlo $D^0 \to \pi\pi\pi^0$ Events in the Dalitz Corners for Signal, Midwing and Highwing Regions 78
6.19 Monte Carlo $D^0 \to K\pi\pi^0$ Events in the Dalitz Corners for Signal, Midwing and Highwing Regions 79
6.20 Monte Carlo $D^0 \to K^0\pi\pi$ Events in the Dalitz Corners for Signal, Midwing and Highwing Regions 80
6.21 Monte Carlo $D^0 \to K\pi\pi^0\pi^0$ Events in the Dalitz Corners for Signal, Midwing and Highwing Regions 81
6.22 Monte Carlo $D^0 \to K\rho$ Events in the Dalitz Corners for Signal, Midwing and Highwing Regions 82
6.23 Distribution of the $D_s^+ \to \eta'\pi^+$ MC events in the $\pi^+\pi^-\pi^+$ invariant mass spectrum. 86
6.24 $D_s \to \eta'\pi^+$, $\eta' \to \rho^0\gamma$, $\rho^0 \to \pi^+\pi^-$ MC events.a) all events with 1.4< $M_{\pi\pi\pi}$ <2.05 GeV/c^2; b) $m^2_{\pi_1\pi_2}$ projection of all events from a); c) $m^2_{\pi_1\pi_2}$ projection of events within D^+ mass window; d) $m^2_{\pi_1\pi_2}$ projection of events within D_s mass window. 87
6.25 Plotting $\Lambda_c \to pK\pi$ as $\pi\pi\pi$ and Looking in the D_s Mass Window 89

7.1 Possible Resonance Contributions 92
7.2 Analysis Dalitz Plot 92

7.3 Feynman Diagram for the process $D \to (r)\pi_3 \to \pi_1\pi_2\pi_3$ . . . 99

8.1 Fit to Projection Gives Centroid and Width of Double Gaussian Representing D^0 plus π Background 106
8.2 Generated Non-resonant $D_s^+ \to \pi^+\pi^-\pi^+$ Monte Carlo Dalitz Plot 109
8.3 Surviving Non-resonant $D_s^+ \to \pi^+\pi^-\pi^+$ Monte Carlo Dalitz Plot 110
8.4 Binned Efficiency Function 111
8.5 Rotated View of Figure 8.2 Showing Low-Population Edge Bins 113
8.6 Binned Data Dalitz Plot 114
8.7 Final Data Sample After Tight Cuts 119
8.8 a) Final Data Sample Distribution; b) Monte Carlo Distribution; c) χ^2/bin comparing MC and fit; d) s_{12} and s_{23} projections for data (plotted) and MC (points with error bars) . . . 122

1. INTRODUCTION TO THE ANALYSIS

1.1 Introduction and Overview

In 1953, R Dalitz [1, 2] suggested that a study of the energy distribution of the three pions in K meson decays would give information about the spin and parity of the K meson. This idea has since been used to extract information about the properties of many decay mode substructures.

This thesis analysis uses those ideas to analize the substructure of the decay of the D_s meson into three pions. Throughout this thesis, the charge conjugate is implicitly included unless explicitly stated to the contrary, so this analysis of the D_s meson decay into three pions is really the combination of the decay $D_s^+ \to \pi^+\pi^-\pi^+$ and the decay $D_s^- \to \pi^-\pi^+\pi^-$. The convention to use the positively charged D_s^+ decay ($D_s^+ \to \pi^+\pi^-\pi^+$) to represent the combination was selected only to shorten notation.

The differences among the charmed meson lifetimes are not well understood. The explanations often given involve "final state interactions" or "destructive interference". This has motivated studies of exclusive processes that can provide a means to distinguish among these effects. The process $D_s^+ \to \pi^+\pi^-\pi^+$ offers one such opportunity—the opportunity to observe and directly contrast the spectator and annihilation contributions. Without the existence of final state interactions, the absence of strange particles in the final state can only be explained through the Cabibbo allowed annihilation sub-process $cs \to \mathrm{W} \to ud$, as seen in Figures 1a and 1b. The diagram in Figure 1c illustrates another mechanism for the s and $\overline{s}$ to form an f_0 state (to choose a particularly telling $s\overline{s}$ resonance), and the process $D_s^+ \to \pi^+\pi^-\pi^+$ could occur via the spectator decay $D_s^+ \to f_0\pi^+$, followed by $f_0 \to \pi^+\pi^-$.

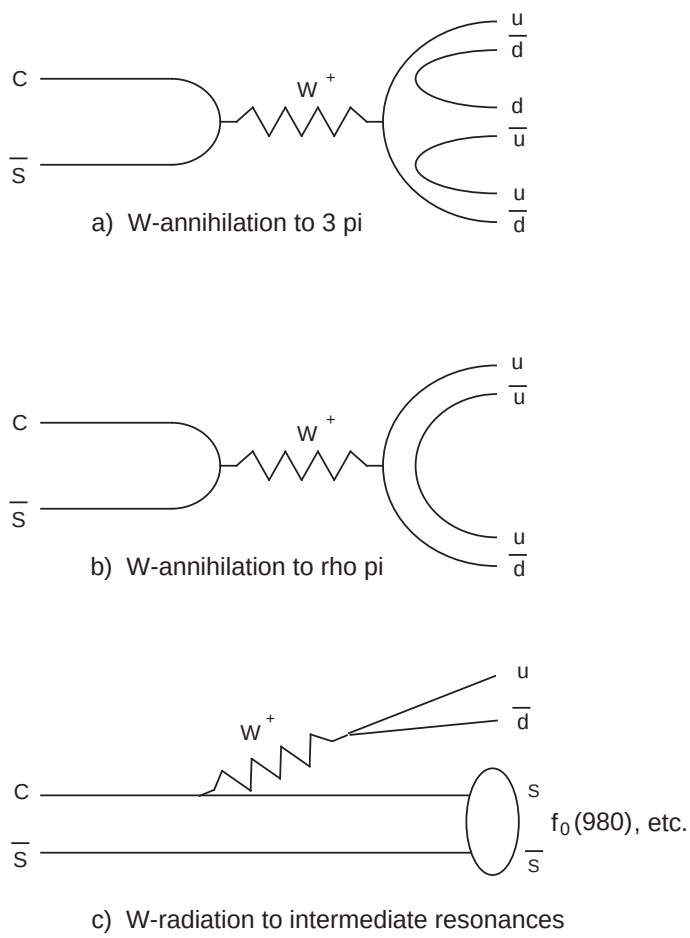

Fig. 1.1: Diagrams for $D_s^+ \to \pi^+\pi^-\pi^+$ final states

The decay to three pions shown in Figure 1a should occur isotropically, since there is no particular final state configuration prefered over any other. The diagram in Figure 1c, however, will have structure—two of the three pions will have come from a specially created intermediate resonance. These $\pi^+\pi^-$ structures should be seen in a Dalitz analysis of D_s decays into three pions. The observation of any structure can be taken as a measure of the relative importance of various quark diagrams and of final state interactions in fragmentation and decay. The diagram in Figure 1b is included to demonstrate a possible channel for the production of three pions through the creation of a $\rho_0\pi$ intermediate state. Due to their similar production mechanisms, one would expect similar contributions to the $D_s^+ \to \pi^+\pi^-\pi^+$ decay from the two annihilation-diagram channels shown.

E791's large charm sample allows for the highest statistics analysis yet on the $D_s^+ \to \pi^+\pi^-\pi^+$ decay, and this thesis presents results of the study of this decay and its substructure.

Though the observation and measurement of final state interactions are in themselves interesting, the existence of final state interactions (Dalitz plot structure) also will yield states to further investigate. Measuring the decay product distributions and their quantum numbers provides a means to categorize and understand the properties of these final state interactions and the decay products that are observed to form [3, 4]. As an example, the $f_0(978)$ is one of the states of matter seen that has not yet been given a $q\overline{q}$ assignment in the PDG Review of Particle Properties [5]. Both experimentally and theoretically, the identification of the scalar mesons (i.e., those with $I^G(J^{PC}) = 0^+(0^{++})$) among the data collected by physicists has long been a puzzle. Many have large decay widths allowing a strong overlap of individual resonances within the incident partial waves. Although this thesis studies the $\pi\pi$ final state, several other decay channels open up for the scalar mesons within a relatively short mass interval [6, 7]. The $K\overline{K}$ and $\eta\eta$ thresholds produce sharp discontinuities in the energy dependence of the final resonant amplitudes [8]. Further complicating matters is the theoretical expectation to have non-$q\overline{q}$ scalar objects in the mass range below 1800 MeV/c^2 [9]. This is in marked contrast to the relative order of the rest of the nonets surmised to exist in standard quark theory and observed in experiments.

An understanding of the low-lying pseudoscalar, vector and tensor mesons has been quite successfully developed from a theoretical point of view, using the framework of a simple quark model assuming the mesons are quark-antiquark ($q\overline{q}$) states and the baryons are qqq states grouped together in

flavor nonets. Data on meson and baryon resonances show regularities and patterns among the hadron states observed. These patterns imply that the hadron states can be described as being constructed from quark constituents. The experimental evidence for the existence of quarks is strong, and it is now believed that the states observed in nature consist of either three-quark combinations (baryons) or quark-antiquark combinations (mesons).

In contrast, data from studies of the lightest scalars have been confusing and even controversial [10, 11, 12]. There are many experimental I=0 candidates in the literature, although assigning the observed candidates their correct quantum numbers has proved to be difficult, due to the large number of possible candidates, the inability for physicists to decipher which actually belong to the lightest scalar $q\overline{q}$ nonet, and the sometimes conflicting results presented by experimental collaborations [13, 14]. Many of the candidate scalars have poorly measured masses and widths. Besides the Dalitz fit results for the fractional signal amplitudes and phases, as a side product of the high statistics enjoyed by E791, a more accurate determination of the mass and width of several candidate I=0 resonances will be made.

1.2 Measurement to be Made

An appropriate set of selection criteria provide the events for the $\pi^+\pi^-\pi^+$ mass spectrum to be studied in the Dalitz analysis. The methods used to choose cuts and select events are described in the analysis chapters. The cuts are intended to select events that have distinguishable three-track secondary vertices from the decay of charm mesons (including the D_s). Using the track information for these events, the analysis assumes the hypothesis that the three tracks are all pions, and calculates the invariant mass of the three charged tracks. The invariant mass calculated with this assumption for the E791 candidate events that remain after all final cuts is shown in Figure 1.2 for the range 1.78 GeV/c^2 – 2.08 GeV/c^2.

There are two peaks (meaning an excess of events) over a smooth background (the background fit, a combination of two exponentials, is drawn to help guide the eye for later discussions). The peak at higher mass, centered at 1.97 GeV/c^2, represents the D_s signal events for the Dalitz plot analysis presented in this thesis. The peak at lower mass, centered at 1.87 GeV/c^2, is consistent with coming from the decay $D^+ \to \pi^+\pi^-\pi^+$. Further discussion of this plot's features and fit parameters is left for development in the

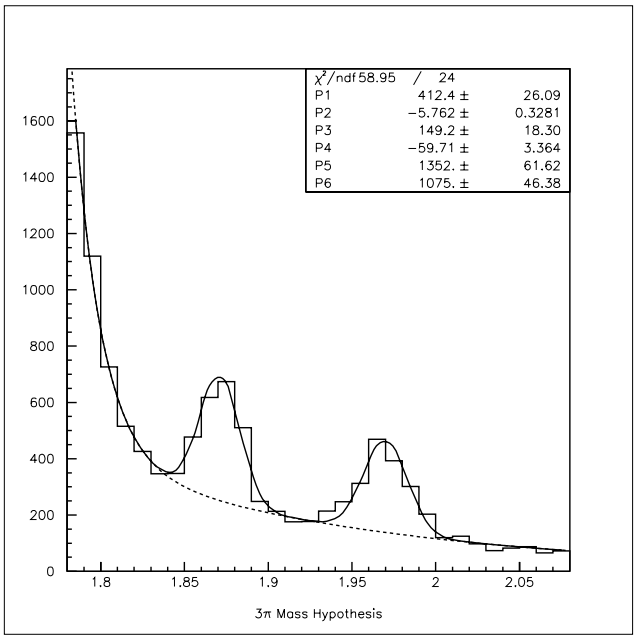

Fig. 1.2: Final Sample Three Pion Mass Hypothesis

appropriate thesis chapters.

Note that there are two $\pi^+\pi^-$ combinations in the decay products of the decay $D_s^+ \to \pi^+\pi^-\pi^+$. Since the analysis is interested in studying the decays of the D_s particle, the next step is to select the events that are contained within the D_s mass range. This thesis analysis examines those events whose invariant mass hypothesis is within $\pm$ 50 MeV/c^2 of the known D_s mass. Since this analysis is especially interested in studying any substructure of D_s decays, additional studies are undertaken for the tracks in these selected events. The analysis studies the distribution of the square of the invariant mass of the two plus-minus combinations in each event. The Dalitz analysis uses the fact that these decay combinations should be evenly distributed on the Dalitz plot in the absence of resonance substructure. For each event in the defined D_s signal region, the squared invariant mass of the two $\pi^+\pi^-$ combinations are plotted against each other in Figure 1.3.

Each event contributes one point to the plot. The plotting mechanism

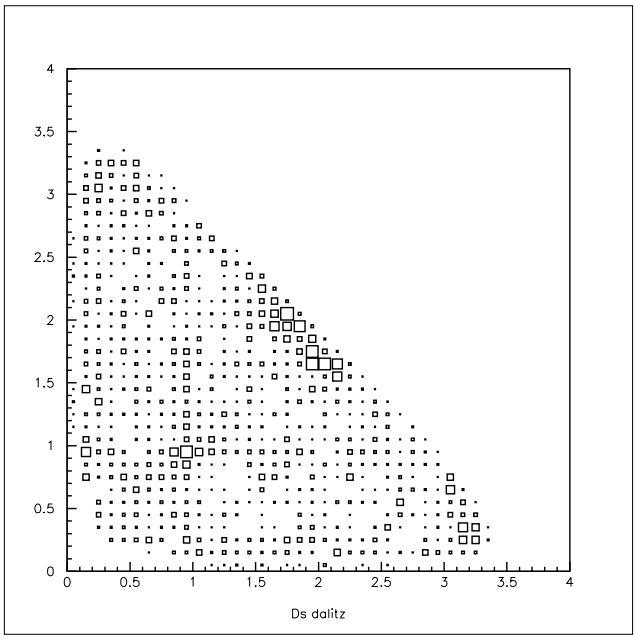

Fig. 1.3: Final Sample Dalitz Plot

in PAW uses larger boxes to denote regions with a higher density of events. Note how the plot has interesting voids and areas that seem to be more densely populated.

The Dalitz distribution will be fit using a maximum likelihood technique, with contributions from sources that are hypothesized to make up any structure that is present. The development of the formalism to model these sources is more fully discussed in Chapter 7. Any structure seen will need to be investigated and understood, in order to correctly incorporate it into the maximum likelihood fit. Incorrect assumptions regarding substructure quantum numbers and interference terms will show up by giving a poor fit to the Dalitz distribution being investigated. Contributions from these possible sources of error are investigated in the error analysis chapter. A contribution from background events will also have to be incorporated since the signal events in Figure 1.2 are not free of background. Once the best combination is found, the final fit result will report the amplitudes of the various resonant compo-

nents and the relative phases between them. These amplitudes and phases can be related to the fractional contributions of the resonant substructures contributing to the Dalitz plot fit. It is the goal of this thesis analysis to report these fractional contributions and the systematic errors associated with the model and methods used to derive them.

2. BEAMLINE AND SPECTROMETER

2.1 Introduction and Overview

Experiment E791 is a fixed target experiment at the Fermi National Accelerator Laboratory which recorded data from July 1991 to January 1992. The experiment was designed to collect and reconstruct a large number of events containing the decay products of charm particles. The experiment was performed in the Tagged Photon Laboratory (TPL), the same experimental hall as some previous "charm" experiments, and the design of E791 reflected what had been learned in these precursor experiments, through the choice of beam and the upgrades performed on the TPL spectrometer.

Particles were produced by colliding a 500 GeV/c π^- beam onto thin platinum and carbon target foils. Not all beam pions caused an interaction, and even fewer produced the charm quark events E791 was designed to study—about 2 of every 100 beam pions incident on the target foils produced an interaction in the target, and of those, one in $\sim 10^{-3}$ contained a charm quark.

The particles produced in a collision travel through the spectrometer, allowing information about the charged and neutral particles produced to be collected in the various detectors that comprise the spectrometer. Due to the nature of the detectors chosen, charged particles interact with all detectors along their path in the spectrometer, while neutral particles only interact with calorimeters near the end of the spectrometer.

Incident beam particles were separated in time on average by about 500 nanoseconds, which provided ample time for the experiment to take a "snapshot" of the event—to collect the charged and neutral particle information for an individual collision where particles are produced.

During the run, E791 wrote over 20 billion events to 8mm tape. The original goal of reconstructing 100,000 charm decays has been exceeded by more than a factor of two. This thesis measurement was performed on 2,468 events selected from the 20 billion originally collected.

The next two sections discuss the production of the beam that reached the TPL targets, and the detectors that were used to make measurements of the charged and neutral particles.

2.2 Beam

The source of the 500 GeV/c π^- beam used at TPL was the 800 GeV/c Tevatron proton beam. Figure 2.1 shows the Tevatron and beamlines which served TPL.

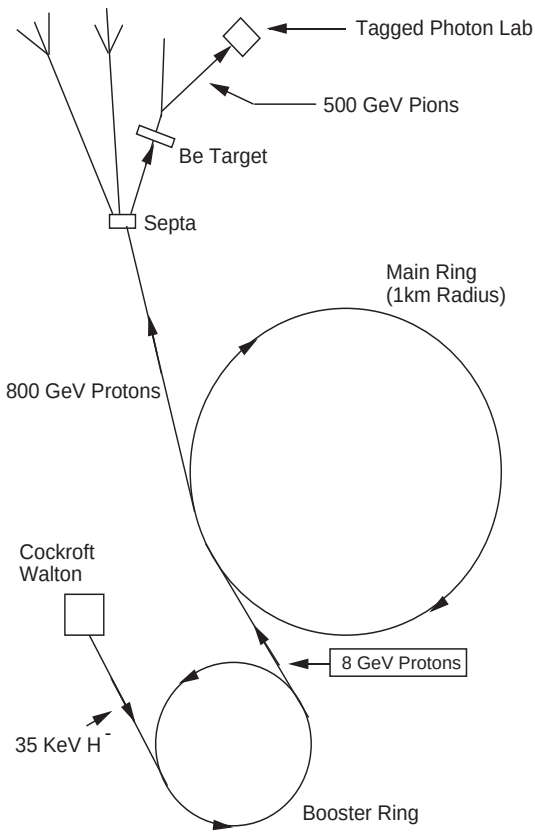

Fig. 2.1: Beamline Schematic to TPL

Extraction of the 800 GeV/c protons occurred once every 57 seconds. The extraction process, called a spill, lasted 23 seconds. There were approximately 10^{13} protons extracted from the Tevatron during this 23 second spill.

Between spills, the Tevatron was refilled with protons, and the proton energy was ramped up to 800 GeV/c^2 in preparation for the next spill.

The 10^{13} protons were split electrostatically, and sent to three experimental areas called the Meson, Neutrino, and Proton lines. There were 14 experiments in these lines during the 1991 fixed target run waiting for their allocated beam each spill. The 800 GeV/c^2 protons entering the proton area were again split electrostatically into Peast, Pcenter, Pwest, and Wideband beam lines. TPL is located in the Proton line, specifically, the Peast line. The 2x10^{12} protons from each spill that were allocated to the Peast beam line were focussed on a 30 cm Beryllium (Be) target approximately 800 meters upstream of the E791 target. Some of the protons interact with the Be, producing a spray of secondary particles.

Downstream of the Beryllium target, dipole and quadrupole magnet field strengths and polarities were chosen to insure that particles of the appropriate momentum and charge would be selected out of the spray of particles and would be steered through the collimators. Figure 2.2 shows a simplified schematic of this selection process.

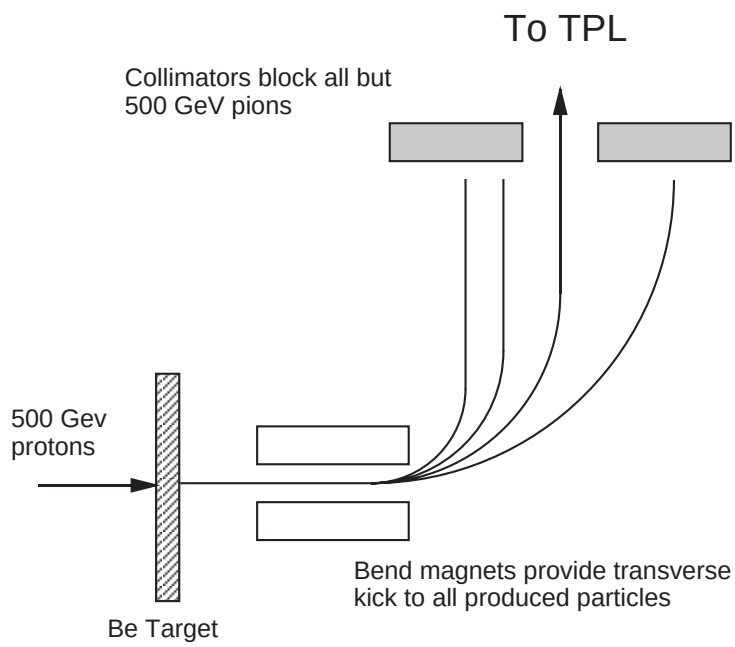

Fig. 2.2: Particle selection using magnetic field and collimator

The 500 GeV/c π^- were then further focussed and directed to the TPL

Tab. 2.1: E791 Target Information

z-position (cm)	material	thickness (cm)	radiation length (%)	interaction length(%)
-8.191	platinum	0.052	0.169	0.00584
-6.690	carbon	0.157	0.012	0.00589
-5.154	carbon	0.157	0.012	0.00586
-3.594	carbon	0.153	0.012	0.00582
-2.060	carbon	0.158	0.012	0.00582

experiment hall and onto the E791 target foils.

The typical yield from the Be target was 42 million secondary pions per spill directed onto the E791 target. Note that 42 million pions in a 23 second spill is an average instantaneous rate of about $2\text{x}10^6$/sec (ie., 2 per microsecond). This rate incident on E791's 2% target produced about 40,000 interactions per second.

2.3 Target

The target was a platinum cylinder of 1 cm diameter and 0.052 cm thickness, followed by four carbon (diamond) cylinders of 1 cm diameter and 0.157 cm thickness. The target cylinders were mounted one after another in a Lexan holder, and were separated from each other by about 1.5 cm center-to-center. The target assembly dimensions and positions were determined using a traveling microscope. Exact target information can be seen in Table 2.1.

Figure 2.3 shows a schematic of the target foils. The schematic is a drawing of the target and trigger scintillator assembly in cross section, viewed in a plane that parallels the beam direction. The scintillator wave guides and readout have been omitted in this schematic. The Beam Spot Counter is really a square paddle of scintillator material, 0.1 inch thick and extending 0.5 inch by 0.5 inch in area perpendicular to the beam. The Beam Halo Counter is another square paddle 0.25 inch thick and 3 inch by 3 inch in area, with a 0.375 inch circular hole in the center (large enough to allow the beam to pass). The Interaction Counter downstream of the target assembly is a circular disc of scintillator material, 1.5 inch diameter and 0.125 inch thick. A discussion of function of the trigger scintillation assembly is presented in Chapter 3.

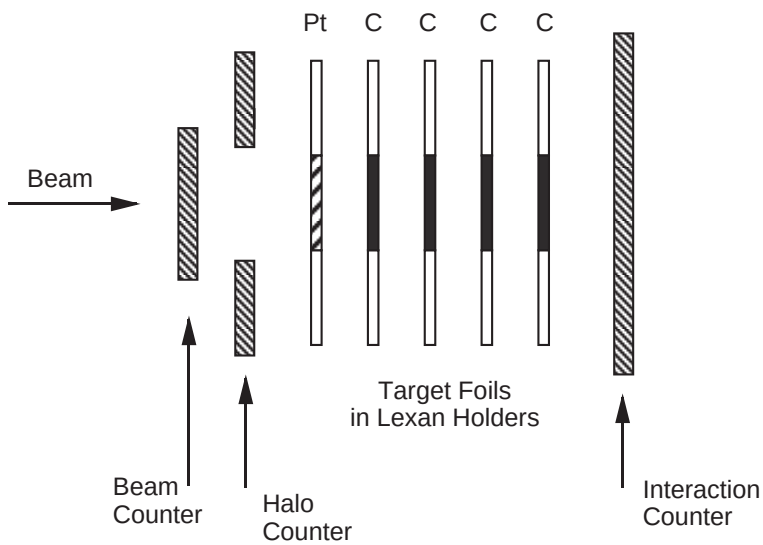

Fig. 2.3: E791 Target Configuration Schematic (not to scale)

The fact that the foils were so thin provided a strong constraint on the position of any 500 GeV/c π^- primary interaction vertex, and the air gaps between the disks provided a volume for reconstructing secondary vertices uncontaminated by possible secondary interactions. A plot of the Z position of reconstructed primary and secondary vertices from E791 data is provided in Figure 2.4.

The E791 average D meson energy is about 60 GeV/c, so $\gamma\beta c\tau$ is about 4 mm for a D^0 and about 10 mm for a D^+. Dense materials were chosen

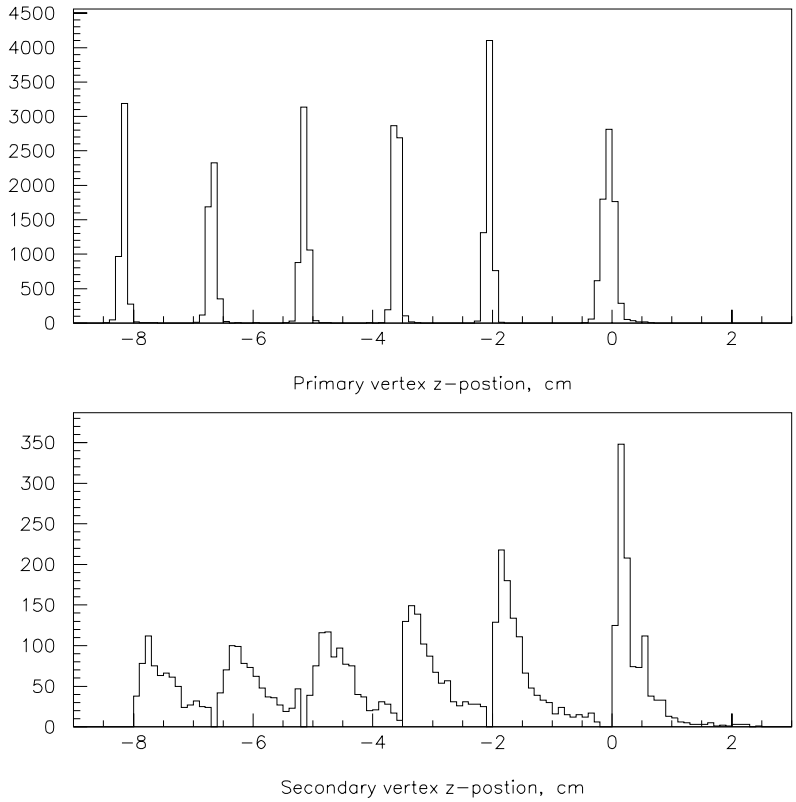

Fig. 2.4: E791 Vertex Reconstruction

to allow thin targets which would still provide enough material for ∼2-3% of the incident pions to interact. It is also important to note that this is an interaction rate that could be handled by the E791 Data Acquisition system. The target separated two spectrometer regions—an "upstream" section, traversed by the beam before reaching the target location, and a "downstream" section, defined as the region past the target location. The E791 notions of "farther upstream" or "farther downstream" will be useful in describing

certain detector positions ("plane 23 is farther downstream than plane 1") in the descriptions that follow.

2.4 TPL Spectrometer

This section will discuss each of the spectrometer components, describing its characteristics, how it was used, and its actual performance during the run. After a definition of the E791 Coordinate System, the discussion is divided into "upstream" beam tracking, which locates the beam track and provides information to further constrain the primary vertex, and the "downstream" components of the spectrometer that collected the information when an interaction occurred, combined to make each event's "snapshot".

The spectrometer, in the configuration used by E791, is shown in detail in Figure 2.5.

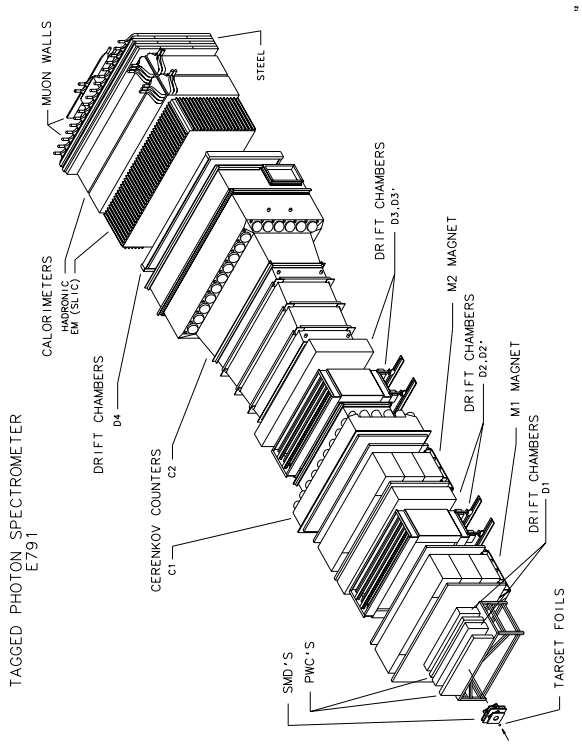

Fig. 2.5: The E791 Spectrometer

The TPL spectrometer had two magnets, which were used with 35 Drift Chamber planes and two Proportional Wire Chambers (PWCs) to provide charged particle momentum information. The 23 silicon microstrip detectors provided high-resolution vertexing and beam tracking. Other parts of the spectrometer were two Cerenkov counters to provide non-destructive charged particle identification over a wide momentum range, an electromagnetic shower calorimeter to detect electrons and photons, a hadronic calorimeter to detect neutral hadrons and to measure particle energy, and two muon scintillation-counter "walls" for muon identification. Not all components of the spectrometer were explicitly used in the analysis; only those that were are discussed in detail.

2.5 E791 Coordinate System

As charged particles traveled through the spectrometer, they interacted with the position-measuring detector planes. Defining a consistent coordinate system allowed for each of the detector plane locations to be known. Therefore, the points in space where the particle trajectories intersect the measuring planes (which we call "hits") can be related. The series of these intersecting points is called a "track" through the detector. When one takes a "snapshot" of each event, it merely consists of a series of these intersection points. The three dimensional reconstruction of these points is what allows the snapshot made to be used in an analysis. If there were only one track in each event, reconstruction would be easy. However, the mean charged track multiplicity of E791 events is about 7, and the typical X and Y views of the hits in the SMD planes looks like those seen in Figure 2.7.

The Z axis of the E791 coordinate system was defined as being perpendicular to the plane of SMD detector number 7. The zero of this Z direction was defined to be very near the interaction counter (just downstream of the target assembly), with Z increasing in the downstream direction. As a convention, centimeters were used to measure lengths in E791. This put the first beam PWC plane at a Z position of -3117 cm, and the last muon wall at a Z position of +2243 cm—our spectrometer was over 53 meters in length.

Looking downstream towards more positive Z, the Y axis was defined as pointing up, and the X axis as pointing towards the left, thus forming a mutually perpendicular right-handed global coordinate system. All the detector planes in the spectrometer were approximately centered around the

Z axis. Exact plane locations and configurations will be presented as each detector system is discussed.

This coordinate system allowed the actual detector plane positions to be measured with respect to this global coordinate system through simple tilts and a rotation, as measured by alignment runs. These measured tilts and rotations were applied to the recorded X' and Y' hit positions to obtain the true X and Y hit position in the global coordinate system. It was these hit positions that were used in the fitting programs to construct three dimensional tracks.

2.6 Upstream Tracking of the Beam Particle

A series of Proportional Wire Chambers [15] (PWCs) and Silicon Microstrip Detectors (SMDs) were used upstream of the target to locate the incoming beam particle(s). There were two stations of PWCs—one more than 31 meters upstream of the target, the other positioned closer to the target. The farthest upstream station provides a long lever arm for precise measurement of the beam track's incoming angle, while the combination of the other station of PWCs and two SMDs planes located close to the target assembly provides good spatial resolution on the beam track immediately upstream of the target assembly. Good spatial resolution on the beam track provides an important contribution to the precision with which the X and Y position of the primary vertex can be measured. This precise determination can be used as either an anchor for downstream track searches or a comparison check with the vertex location obtained from the tracks in the downstream tracking detectors.

2.6.1 Beam Track Proportional Wire Chambers

The PWCs consist of a series of evenly spaced sense wires held at ground sandwiched between planes held at a high negative voltage. Each sense plane contained 64 wires, spaced 1 mm apart. Each station of PWCs was made of four sense wire planes, arranged to measure different views. The enclosed volume is filled with a gas mixture of 82.7% Argon, 17% CO2, and 0.3% Freon. When a charged particle crossed this gas, it ionized atoms, leaving a trail of free electrons and ions. The electrons were forced to migrate in the PWC electric field, moving towards the nearest sense wires. As the electrons were accelerated in the high-field region near the cathode, they reach velocities that ionize more atoms, creating an even larger number of free

Tab. 2.2: E791 Proportional Wire Chambers

PWC assembly	number of planes	cell size(cm)	active area x×y (cm^2)	z-position (cm)
upstream	8	0.1	6.4 × 3.2	-3117.0
downstream	2	0.1	53.0 × 28.8	118.5

electrons, called an avalanche. This excess of free electrons in combination with the subsequent migration of the positive ions away from the sense wire creates an electrical pulse on the sense wire, registering the position of the charged particle.

The charge from the electrical pulse was amplified and discriminated, which turned any signal over 0.7V into a digital signal (ie, a 1 if there was a hit, or a 0 if there was not). With the small wire spacing, electron drift times were nearly negligible, and the current signal peak was sensed at the amplifier about 15ns after the ionizing particle passed through the chamber. Because the PWCs were so far upstream of the trigger electronics, the total charge collection and discrimination time was too long to allow use of this information in the trigger process (for instance, to include the number of incident particles in the beam in the trigger logic). Instead, the information was written out along with the rest of the event data, allowing events with multiple beam tracks to possibly be removed at a later time. There was more than one beam particle in a bucket about 0.5% of the time.

Details of the E791 Proportional Wire Chambers are given in Table 2.2.

The wire spacing of 1mm allowed for a $1\text{mm}/\sqrt{12}$ resolution. This resolution, over the 10m lever arm between the upstream and downstream PWCs, gives a beam track angular resolution of about 58 micro radians.

2.6.2 The Beam Silicon Microstrip Detectors

As stated, the SMDs were used to complement the angular resolution provided by the PWCs. There were six SMDs upstream of the target. SMDs

Tab. 2.3: E791 Beam Tracking SMD Planes

plane	orientation	z-position (cm)	pitch (μm)	width (cm)	efficiency
1	y	-80.250	25	5.08	0.85
2	x	-79.919	25	5.08	0.85
3	u	-74.529	25	5.08	0.98
4	u	-33.163	25	5.08	0.98
5	x	-30.133	25	5.08	0.98
6	y	-29.483	25	5.08	0.98

operate by sensing charges as charged particles pass through an SMD plane. An SMD plane consists of a wafer of Silicon 300μm thick, ion-implanted on both sides. Boron was implanted on the upper face to form p-type strips. Aluminum was deposited over the boron to serve as an ohmic contact. The strip spacing was 25μm on planes close to the target, and 50μm on the other planes. The opposite side of the silicon wafer was doped with a continuous layer of arsenic. Aluminum was also deposited over the arsenic to allow for a good ohmic contact to be made. A reverse bias voltage applied to the pn junction structure creates a region depleted of charge carriers. When a charged particle passes through the detector, it liberates about 24,000 electron hole pairs into the conduction band. This charge migrates under the electric field, and its image is sensed at the nearest strips in about 10ns. The amount of charge collected was too small to travel through signal wires more than about a meter without amplification, so the signals were preamplified and then fanned out to amplifier-discriminator cards before being sent to the Data Acquisition System. A table of upstream SMD characteristics is presented in Table 2.3.

There were several different orientations of the upstream (as well as the downstream) silicon strips. These orientations were named according to the orientation of their strips as defined in this schematic of the view directions:

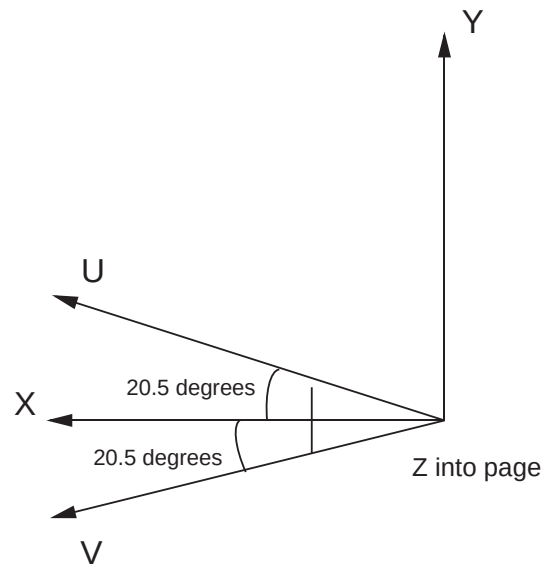

Fig. 2.6: E791 SMD View Directions

By assembling the SMD planes in groups with three different orientations (X, Y and V or X, Y and U), there is enough information to associate the hits and locate the track SMD plane intercept point without ambiguity. Redundant information helped to resolve instances of multiple hits or SMD strip noise.

2.7 Downstream Charged Particle Tracking

2.7.1 The Downstream SMDs

There were seventeen downstream SMD planes [16], which were used to capture the particle trail "hits" for later track and vertex reconstruction. The angular acceptance of the SMD vertex system was approximately ± 100mrad around the beam axis. The seventeen SMD planes were grouped into six individual sets of SMDs in the E791 Spectrometer, and captured information in four different views of each event's charged tracks. A schematic of the grouped E791 downstream silicon system is depicted in Figure 2.7a.

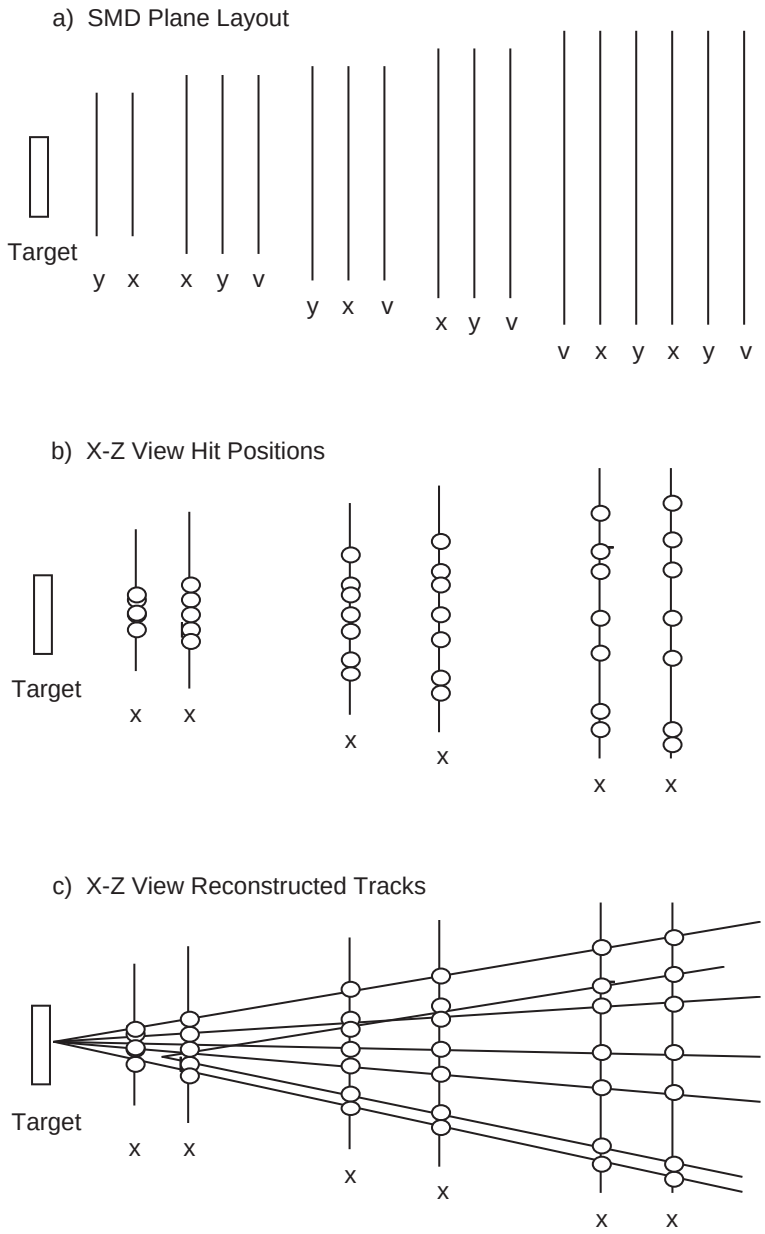

Fig. 2.7: Downstream SMD Layout and Track Hits

As will be shown in the analysis section, the ability to use the SMDs to provide track hit information used to separate secondary from primary vertices substantially reduces non-charm backgrounds. The seventeen SMD planes help to constrain the Z position of a secondary vertex to $\sigma_z \approx 400\mu$m, and the transverse position to $\approx 10\mu$m. The SMDs were very important to the success of E791's spectrometer.

Figure 2.7b) demonstrates how difficult it can be to successfully reconstruct an event's charged tracks from the SMD hit information. The X-Z view presented shows many particles originating from a primary vertex in the target foil, as well as a two-prong secondary vertex from a decay that took place between the first two X-view planes (peek at Figure 2.7c for a depiction of the clean event). The difficulty to even correctly reconstruct the X-Z view is compounded by the fact that the two dimensional schematic shown represents only one of the four SMD views (there is also a Y-Z view, an V-Z view, and a W-Z view) that must be reconstructed and combined to provide the actual three dimensional charged track reconstruction for an event.

While the upstream SMDs usually had only one track passing through, the downstream SMDs saw the E791 average multiplicity of about 12 tracks per event.

Two final added difficulties which affect charged track reconstruction are the presence of noise in the strips or electronics which will add additional "hits" that are not actually associated with a track, and the existence of SMD plane inefficiency which will cause some 'hits' to be lost. This makes low noise and high efficiency very important for detection, and a good reconstruction program important to be able to then reconstruct any captured vertices. Clearly, adding additional "hits" or removing some of the "hits" in Figure 2.7b) would make the view's reconstruction more difficult. The SMD efficiency was about 90%, with about 0.1% noise. A table of downstream SMD characteristics is presented in Table 2.4.

There is no magnetic field in the SMD section of the spectrometer, so charged tracks experience only multiple scattering effects to pull them off of their straight-line trajectories. The 300μm SMD plane thickness is thin enough so that the charged track multiple scattering road width that must be considered when attempting to reconstruct tracks is kept small. Charged track momentum information is also very useful. Having this information allows high momentum tracks to be weighted as being more certain to be straight lines in the reconstruction programs. The longer lever arm provided

Tab. 2.4: E791 Downstream SMD Planes

plane	orientation	z-position (cm)	pitch (μm)	width (cm)	efficiency
7	y	0.670	25	2.54	0.83
8	x	1.000	25	2.54	0.85
9	x	1.931	50	2.54	0.93
10	y	3.015	50	2.54	0.95
11	v	6.684	50	2.54	0.96
12	y	11.046	50	5.08	0.98
13	x	11.342	50	5.08	0.97
14	v	14.956	50	5.08	0.94
15	x	19.915	50	5.08	0.90
16	y	20.254	50	5.08	0.88
17	v	23.878	50	5.08	0.98
18	v	27.558	50	9.00	0.98
19	x	31.848	50	9.00	0.96
20	y	34.548	50	9.00	0.98
21	x	37.248	50	9.00	0.99
22	y	39.948	50	9.00	0.99
23	v	45.508	50	9.00	0.99

Tab. 2.5: E791 Magnets

	M1	M2
Z-position (cm)	273.5	617.7
aperture (cm^2)	174×86	171×88
length (cm)	165	208
current (amps)	2500	1800
p_T kick (Gev/c)	0.21	0.32

by the next section's Drift Chambers, when hits from the two sections are matched, also helps to insure the correct set of hits has been connected in three-space.

2.7.2 The Drift Chambers and Analysis Magnets

The momentum of charged particles is determined by measuring their change in direction from passing through a magnetic field. Two large-aperature magnets provide the field, and the trajectories are measured with drift chambers. The details of the magnets are given in Table 2.5.

A particle with unit charge and velocity $\vec{v}$ passing through a magnetic field $\vec{B}$ experiences a force $\vec{F} = \mathrm{d}\vec{p}/\mathrm{dt} = \mathrm{q}\vec{v} \times \vec{B}$. The main component of the magnetic field was in the +Y direction and the main component of the particle velocities was in the +Z direction, so depending on their charge, charged particles were bent in the +X or –X direction. The magnetic field was mapped by Fermilab's "ziptrack" apparatus before data taking, and fine-tuned each run for possible current fluctuations by reconstructing K^0 particles. Ziptrack is a Fermilab magnet mapping machine that uses three small mutually-perpendicular coils with a common center to measure a magnetic field's components at a given point in space[17].

The drift chamber is a device that uses the drift time of ionization electrons in a gas to measure the spacial position of an ionizing particle. They are composed of sets of sense planes, which comprise a plane of alternating field-shaping wires and sense wires sandwiched between cathode planes to form drift cells around each sense wire.

While the mechanism to produce and collect the ionizing free electrons is the same as the PWCs, the DCs have field-shaping wires to optimize the shape of the electric field within a cell. From the known drift time for a particular gas and voltage combination, the particle's distance from the sense wire (d) can be determined by the relationship $\mathrm{d} = \Delta t \times \vec{v}_D$. The gas combination and field strength in our detectors resulted in a drift velocity of 50 μm/nsec.

There were four separate drift chamber modules in the E791 spectrometer, containing a total of thirty five planes measuring four different views, namely X,X',U and V. The X and X' views were vertically strung wires (ie, they ran in the $\pm$Y direction), with the X' view shifted by one half cell relative to the X planes. The U and V views had their wires at ± 20.5 degrees from the vertical. Details of the E791 Drift Chambers are given in Table 2.6.

The first chamber D1 was located upstream of the first magnet M1, and along with the SMDs and PWCs, provided an initial measurement of the charged particle trajectories in a non-magnetic field region (ie, the trajectories would be straight lines). The second chamber D2 was positioned between the two bend magnets. The third chamber D3 was located just after the second bend magnet M2, and provided tracking information for charged particles with high enough momentum to make it through both bend magnets. The last chamber D4 was positioned far downstream. Despite its long lever arm, this chamber was less useful due to noise from backscattering from the calorimeter and poorer spatial resolution (D4 drift cells were twice as large as those in D3). The central-most region of the first three drift chambers had very low efficiency due to the simultaneous existence of many charged particles during a spill—space charge (drifting ions from charged particles in the previous events) degraded the performance of regions of the detector that were highly populated.

The Drift Chamber planes were grouped in assemblies, because each view cannot by itself be used to determine the exact location of a hit due to left-right and double-hit ambiguities. The left-right ambiguity occurs from the fact that the time the electrons take to reach a sense wire is the same no matter which side of the sense wire the charged particle passed. Double-hit

Tab. 2.6: E791 Drift Chambers

DC assembly	cell size (cm) U/V	X	active area x×y (cm^2)	z-position (cm)
D1-A	0.476	0.446	86 × 65	156
D1-A	0.476	0.446	114 × 65	192
D2-1	0.892	0.953	182 × 130	384
D2-2	0.892	0.953	182 × 130	426
D2-3	0.892	0.953	210 × 130	468
D2-4	0.892	0.953	228 × 130	499
D3-1	1.487	1.588	254 × 130	930
D3-2	1.487	1.588	254 × 130	972
D3-3	1.487	1.588	254 × 130	1014
D3-4	1.487	1.588	302 × 130	1045
D4	2.97	3.18	508 × 240	1744

ambiguity arises when more than one wire in a particular view has a signal. Complete reconstruction of the X and Y position of a particle requires information from at least three different views. See Figure 2.8 for an illustration of how an extra X' view, offset by half a cell width from the X view, helps to eliminate the hit ambiguity in the X direction.

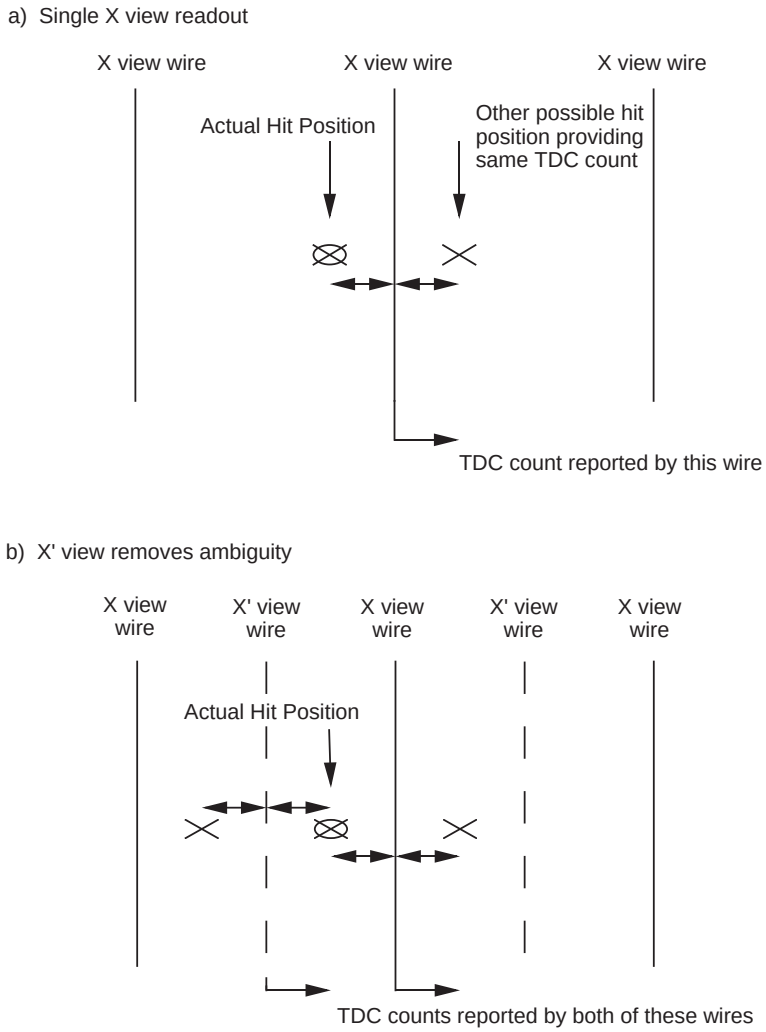

Fig. 2.8: Double Hit Ambiguity

The small pulse collected by sense wires was first passed through an amplifier/discriminator before reaching the time-to-digital convertors (TDCs). TDCs are programmable units that can store in memory and automatically

subtract off the value of the electronic time offset for each wire. The offset times were regularly measured by sending computer-generated pulses to each Drift Chamber channel and reading the arrival time at the TDCs. The drift time was measured backwards from a common stop for all channels of all chambers. While SMD channels register either a 1 (a hit) or a 0 (no charged particle registered), drift chambers report the actual distance from the particle to the sense wire by sending each wire's recorded TDC time for an event to the Data Acquisition (DA) system. Alignment constants were determined at regular intervals by turning off the analysis magnets and recording low-rate muon calibration runs. Muons were directed towards the chambers by closing upstream collimators so only muons reached TPL. Straight tracks through all chamber assemblies allowed for accurate determination of individual plane offsets, tilts, and rotations. The drift time was also corrected for the Z-position of the individual planes before being recorded in the DA system. The DA system was located in a space outside of the hall that housed the spectrometer—even with particles moving near the speed of light, and signals moving through wires at the speed of light, each individual detector interacts with the event particles at a slightly different time and has its own individual signal wire path to the DA system. Even at 3×10^8 m/sec, every extra 30m of wire adds an additional 0.1 μsec of signal travel time.

2.8 Particle Identification

2.8.1 The Čerenkov Detector

Charm particles decay predominantly into final states containing a strange quark—those containing K mesons, or hyperons (Σ, Ξ) which decay into protons (or neutrons) and pions. The two threshold Čerenkov counters [18] in the TPL spectrometer can be used to distinguish the electrons, kaons and protons from the more abundant pions. The first counter, C1, was positioned partially inside of M1 and the second counter, C2, was positioned after magnet M2. This analysis was performed without using the information that could be obtained from the Čerenkov counters to avoid introducing systematic errors that could not be adequately modeled in the E791 Monte Carlo. The Čerenkov detector was not used in this analysis.

2.8.2 The Calorimeters

In experiment E791, the calorimeters at the end of the spectrometer provided the first opportunity to detect the presence of both neutral and charged particles. A calorimeter is a device that measures the energy deposited by a particle (or a group of particles). The TPL calorimeters were sampling calorimeters, which means they periodically sample the development of a shower initiated by an incident particle. E791 has two types of sampling calorimeters, distinguished by material composition and sampling frequency[19, 20, 21]. While not specifically used in the analysis, the calorimeters were used as part of the decision-making process when deciding whether to discard or keep a particular event and record it to tape. The E791 triggering and DA system is discussed in the next chapter.

3. EVENT TRIGGER AND DATA ACQUISITION SYSTEM

3.1 Introduction and Overview

E791 chose to record data with a very open trigger. The method implemented was to impose only loose acceptance constraints on the data during the actual run, and to select events of interest during the offline analysis which was performed after the completion of the run. Imposing loose constraints when recording data and selecting events offline with software provided E791 several advantages. First, E791 was able to avoid the large expense of developing specialized high-speed trigger logic and hardware. Next, an open trigger introduced minimal bias on the data taken, allowing for less biased charm production studies to be performed on a variety of parent and decay modes. Third, having the unbiased sample stored on tape allowed for several streams of event selection to occur, as well as allowing any analysis to quickly back-track one selection stage to benefit from new analysis methods or discovered temporary analysis errors. Finally, the purchase of needed offline computing resources could be put off, allowing E791 to benefit by purchasing cheaper and more powerful machines that would be available when offline analysis was finally performed.

E791 built a high-speed Data Acquisition (DA) system to be able to collect data with such an open trigger. Event information collected by each detector was sent to the detector's digitization system and then output to the DA. The DA read out the digitized information supplied by each spectrometer component, and combined it with trigger information before writing the event to 8mm tape. E791 recorded over 20 billion events on 24,000 8mm tapes between July 1991 and January 1992, which represents a 50 Terabyte data sample.

The following sections outline how the trigger logic selected events to keep, and how DA system collected and combined detector output into discrete events that could be written to tape and kept for analysis.

3.2 The E791 Trigger

Not every event was selected to be output to 8mm tape. While loose, E791's trigger logic was designed to throw out events that did not meet certain selection criteria. The trigger logic was divided into two levels, each providing information with which to accept or reject events. A pretrigger used information from three scintillation counters located near the target to try to minimize multiple or spurious beam particle events. The second part of the E791 trigger examined the energy deposited in the electromagnetic and hadronic calorimeters as a basis for additional trigger logic decisions.

3.2.1 The Pretrigger Logic

A schematic of the scintillator counters used in the pretrigger was presented in Figure 2.3. The upstream beam spot and beam halo counters were used to reject events with multiple or off-target beam particles. The downstream interaction counter was used to record the presence of interactions in the target foils—the latch threshold for a signal from the interaction counter was set to 4-5 times the signal from a minimum-ionizing particle. An event that passes the pretrigger logic conditions has a hit in the beam spot counter, has no hit in the beam halo counter, and has an interaction in the target foils with enough particles to be able to leave enough light in the interaction counter to generate a signal. The logic to calculate whether the pretrigger criteria was satisfied could be performed in about 160 nanoseconds (160×10^{-9} seconds). This speed allowed a positive pretrigger to be sent to all detector digitization systems, since none of the detector systems in E791's spectrometer had signals that would reach their digitizing systems sooner that the quick pretrigger latch. The pretrigger signal was used to tell the digitizing systems to open their latches to accept and begin digitizing the detector information for this event, since the event passed the pretrigger.

3.2.2 The E_t and E_{tot} Trigger Logic

The intent of the second part of the trigger logic was to enrich the event sample sent to the DA with events that contain heavy quarks and to reject events with multiple beam particles. Since several detector systems could read out their electronics and have signals already in their digitizing systems in the 470 nanoseconds it took to make this second trigger logic calculation,

it was decided to let the digitization start (upon receipt of a valid pretrigger condition), and to send a cancellation if the second trigger criteria was not met.

As stated earlier, this trigger used energy deposit information from the calorimeters. The calorimeter phototubes were read through two different outputs—the full anode signal was sent to the calorimeter digitization system, and the dynode signal was sent to the trigger logic modules (NIM and CAMAC modules). The trigger logic performed two sums with the signals it received, corresponding to the two energy sums listed in this subsection's title.

A weighted sum of the calorimeter dynode signals was made, where the logic modules assigned a higher weight to signals from calorimeter segments farther away from the beam axis. The weighted sum provides an estimate of the transverse energy of the current event for the E_t trigger decision. The E_t trigger logic is calibrated using reconstructed tracks during calibration runs, so the value of the weighted sum obtained in the trigger logic can be related to the actual E_t in an event. From these calibration runs, a discriminator value was set to reject events whose weighted sum corresponded to an event with transverse energy less than about 3 GeV/c^2. The decision to eject events with lower E_t is based on the fact that decay products of particles that contain heavy quarks are produced with more transverse momentum than decay products of particles that contain light quarks.

A non-weighted sum of the calorimeter dynode signals was also made, to obtain the total energy deposited in the calorimeters for the current event. Events with more than 700 GeV/c^2 deposited were rejected to eliminate events that contained more than one beam particle. The cutoff was set higher that the nominal incoming beam energy (500 GeV/c^2) to allow for fluctuations in the measured energy.

If an event passed both triggers and was written to tape, trigger information was always included along with the rest of the digitized event information.

3.3 The E791 Data Acquisition System

As discussed earlier, the Fermilab Tevatron delivered beam during a 23 second spill, with a 34 second interspill period to allow the Tevatron to be refilled. This means that data is only collected in the E791 hall during 23 of

every 57 seconds. The E791 DA system [22] took advantage of this schedule by using buffering to collect event data during the entire 23 seconds, and by using the entire 57 second interval to write the event data out to 8mm tape. A schematic of the DA system components is presented in Figure 3.1.

Events were digitized in a variety of front-end systems and delivered into Event FIFO Buffers (EFB) along eight parallel data paths. The buffers stored 80 Mb of data apiece, enough to allow the rest of the DA system to be active during both the spill and the interspill period. Care was taken to ensure that each data path carried about the same amount of data. Data are distributed through Event Buffer Interfaces (EBI) to processors housed in six VME crates. The processors (CPU) read event segments from the buffers, compressed them into formatted events, and recorded them on tape through a SCSI magnetic tape controller (MTC).

The DA system is *parallel* in several respects. Data arrives along parallel data paths. Processors act in parallel to prepare data for logging. Many parallel tape drives record data concurrently.

To capture the discrete events, raw data from the detector elements was digitized by various electronics systems, which were in turn managed by front-end controllers which delivered data to the DA system. The front-end hardware is summarized in Table 3.1.

Events arrived at the DA system at an average rate of 26 MB/sec during the beam spill. To be able to correctly assemble and keep track of this flood of data, each event segment (from the SMDs, the DCs, the calorimeters, etc.) on the data paths was delimited by a leading word count, which was calculated and placed there by the data path's front-end controller. A 4-bit event synchronization number was generated for each event by a scalar module and distributed to all front-end controllers (the scalar module was incremented by a signal from the event trigger logic). The controllers accepted this number and made it part of the each event's segments. The DA system used the synchronization number to assure that all event segments presented to the DA at a given moment derived from the same event in the detector (a 4-bit number was enough to distinguish the small number of unsynchronized events that might temporarily exist in any one data stream). Event segments with matching synchronization numbers were combined and written to 8mm tape at a rate of 9 MB/sec during both spill and interspill, using 42 Exabyte 8200 tape drives. An average E791 event was about 2500 kB in size.

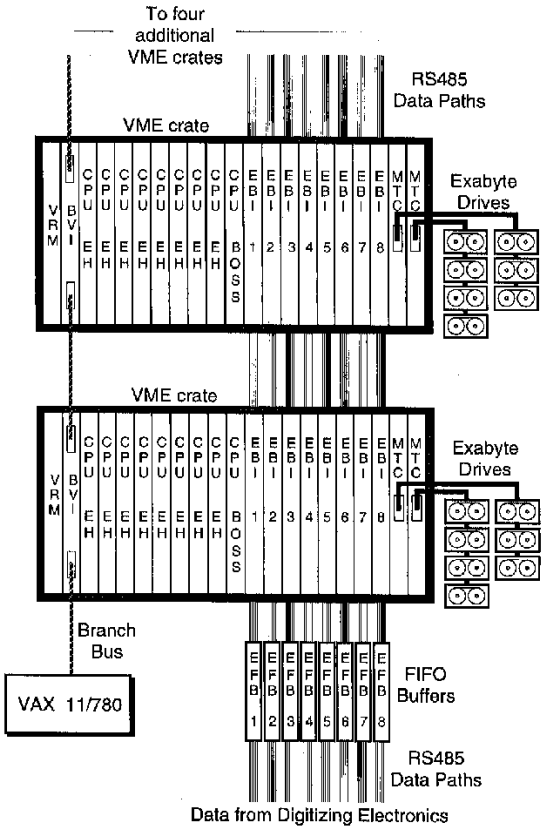

Fig. 3.1: E791 Data Acquisition System

Tab. 3.1: E791 Front End Digitization Systems and Read Out Controllers

System	Drift Chamber	Cerenkov, Calorimeter	Silicon Micro-vertex Detector	Proportional Wire Chamber	CAMAC
Digitizer	Phillips[23] 10C6 TDC	LeCroy 4300B FERA ADC [25]	Ohio State[24], Nometric N339P, Nanometric S710/810 [26] Latches	LeCroy 2731A Latch	LeCroy 4448 Latch 4508 PLU, 2251 Scaler
Mean Dead Time	30 μs	30 μs	50 μs	4 μs	30 μs
Pre-Controllers	none	2 LeCroy 4301s	81 Princeton Scanners	2 LeCroy 2738s	none
Controller	FSCC [27]	Damn Yankee [28]	Princeton [29]	Damn Yankee	SCC [30]
Number of Controllers	10	2	2	1	1
System Channels	6304	554	15896	1088	80

4. THE E791 MONTE CARLO

4.1 Introduction and Overview

Any analysis depends on understanding how a spectrometer is able to detect charged and neutral particles. It also depends on being able to trigger on events and to be able to keep and write these events to tape. Additional dependencies are to be able to read and unpack events from a tape, and to be able to reconstruct tracks and infer particle information from the event information stored on the tape, whether reading from raw data or from Data Summary Tapes (DSTs). A final dependency is to then use computer programs to to be able to sort events into collections of events with the types of features believed will best demonstrate the success of the analysis.

A Monte Carlo (MC) simulation of events in the E791 spectrometer is a powerful tool that can help address how each of the above stage's equipment and technique inefficiencies affects what actually ends up in the analysis. Generating MC events allows complete control over what is created, and thus can contribute in different ways to resolve the problems encountered in each of the above stages.

4.2 Modeling the Events and Spectrometer

The E791 Monte Carlo uses the Pythia and Jetset programs [31, 32] for event generation. These programs can be tuned to generate complete events using simulated target and incident beam particles that match those present in E791's environment. The beam and target particles are simulated to have interacted through known and postulated physical processes; these processes control the types of final state particles that are produced, as well as the properties of the produced particles. For the case of E791, the software was set up to create a $c\overline{c}$ pair from hard processes ($q\overline{q} \rightarrow Q\overline{Q}$ and $gg \rightarrow Q\overline{Q}$) involving constituents in the beam (500 GeV/c π^-) and target (protons and

neutrons in platinum and diamond foils).

The $c\overline{c}$ pair is hadronized into specific charm hadrons (D^0, D^+, D_s, Λ_c, etc.) according to the results of previous production experiments. The charm particles are decayed using previously measured branching ratios. Jetset handles the complicated hadronization model, and also provides plenty of additional tuning levers to allow specific functionality to be enhanced or disabled. Since the Pythia and Jetset software programs are generalizable for a wide range of energy scales and incident or produced particle types, tuning is needed to select out as accurate a behavior as can be obtained to match the environment one is attempting to model.

For instance, the software allows the energy-momentum four-vectors of the produced $c\overline{c}$ pair to be tuned so the generated Monte Carlo D_s distribution in momentum closely matches the distribution observed in E791 data. Another example is the ability to tune the Lund String Fragmentation Model so that the event multiplicity produced closely matches the distribution observed in E791 data.

The end result of the simulated event is a list of particles, from the initial constituents all the way down through the decay chain of the particles that were produced. For each of these particles, their energy-momentum four-vectors and their decay lengths (randomly chosen along each individual particle's lifetime distribution) are known. To make this information useful, the E791 target and spectrometer must now be placed in the way of this generated event.

With an event in hand, the next stage of the MC simulation uses an exponential distribution algorithm of the target material interaction lengths to choose in which of the 5 target foils this event occurred, and associates the generated event's primary interaction point to an X and Y position at that target foil's Z position. Since the rest of the spectrometer detector plane X, Y and Z positions are known, the simulation projects the charged track trajectories from their production points (whether at the primary, or further "downstream" from a later decay) through the spectrometer, recording the X and Y intersection points at each detector plane's Z position. By knowing the granularity and starting and ending points of detector silicon strips and Drift Chamber cells, the track can now be thought of as having hit a particular strip or to have passed a certain distance from a DC wire. By knowing how these strips and cells are read out, the electronics of the SMD digitizing system can be simulated (including adding noise or inefficiency on a per-strip basis, based on the particular strip's performance during actual data taking).

The distance from a DC wire can be converted to TDC counts by knowing the cell's drift time (again based on performance during actual data taking, and again being able to add neighboring noise hits or drop the hit based on the cell's noise and efficiency).

Since there is complete user control in the MC—each event, once generated and digitized, can be analyzed with user code before being written out. This allows events with the user-desired characteristics to be selected from those generated, and only these special events written out to tape. The ability to quickly generate 10-100-1000 times the statistics observed in real data to study a particular behavior or distribution is a powerful tool.

For instance, MC events can be generated with no detector noise or inefficiencies, to examine expected reconstruction code inefficiencies. Conversely, MC events can be generated with very noisy and inefficient detectors, to determine how well reconstruction code actually works.

MC events can be selected out that do (or do not) populate a certain area of the spectrometer so that trigger efficiency code can be tested.

Once all the tracks are propagated, the hit information (including the calorimeter, Čerenkov and PWC or beam tracking information) is assembled and written out to tape in a format that exactly matches that of the E791 data tapes themselves. This allow any analysis that can be done on E791 data tapes to also be performed on E791 MC tapes. In fact, the ordering of that analysis is usually opposite to that just listed.

4.3 Uses of the E791 Monte Carlo

In addition to the reconstructable MC "data" for an event, the MC tapes also contained a special "truth table" for each event. The amount of information that would appear in the truth table was controllable by program flags that could be set before the MC simulation was run. Among the level of detail that could be written out were the actual X, Y, and Z position and X, Y and Z momentum at the particle's production point, the actual X and Y position of each charged track at each detector's Z position, and which tracks in the truth table are associated with a particle's decay products. Each of these pieces of information are very useful in many different ways.

Since the particles in an MC event and the positions they intersect detector planes are completely known before an MC event is output, they can be used to debug tape reading and writing code. Additionally, once MC events

are read in and reconstructed, matching tracks and vertices to those in the "truth table" help to debug and improve reconstruction code. Reconstruction code that correctly matches what is in the truth table can be used with confidence on data itself.

Finally, MC events can be used to determine the effectiveness of a particular cut, or how applying a particular cut biases the efficiency to reconstruct an event in a particular region of phase space.

The techniques outlined in this chapter are used in Chapter 6 to arrive at a set of final analysis cuts, and in Chapters 6 and 7 to investigate possible $D_s^+ \to \pi^+\pi^-\pi^+$ backgrounds.

5. EVENT RECONSTRUCTION AND FILTERING

5.1 Introduction and Overview

Several stages of processing were used to extract events of interest from the large number of E791 events collected. The initial selection stage for this analysis used partially reconstructed events with mild cuts to select events with secondary vertices. The initial filtering [33, 34, 35] discarded about 82% of the original E791 events. Those passing the filtering selection cuts were written to data summary tapes (DSTs), which allowed the physics analyses to start from a reduced number of tapes as well as with the full reconstruction information available for those events that passed the initial filtering. Not having to re-reconstruct events greatly reduced the computing resources needed for successive filtering stages, since the additional analysis for successive stages could be started after merely reading in the DST portion of each event. For this analysis reconstruction chain, the original event data were also written out with the DST, which allowed the original hits and other raw data detector information to be retrieved and re-reconstructed if needed.

The event pool was further reduced by passing the events from the DST through three additional stages of filtering. Information on the tapes was used at each stage to both reduce the number of events passed by applying additional constraints on the events, as well as by collecting events with certain characteristics and topologies into separate output "streams". The data reduction stages are diagrammed in Figure 5.1.

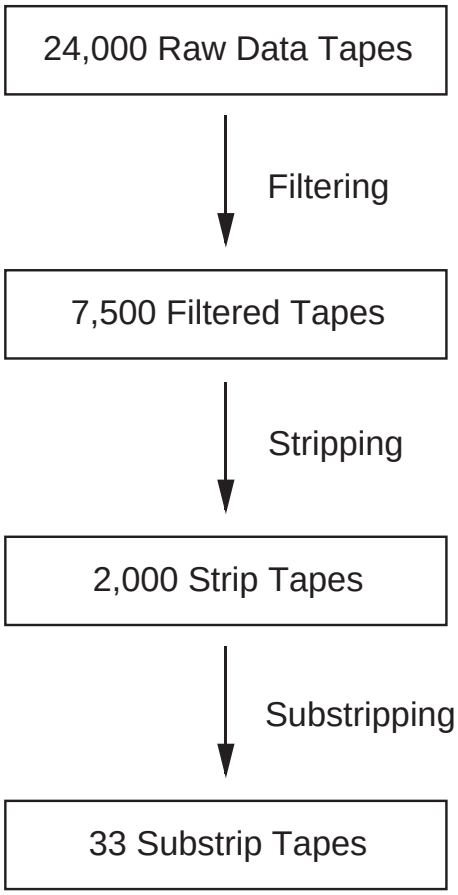

Fig. 5.1: E791 Data Reduction Stages

This chapter discusses the track and vertex reconstruction, the initial filtering cuts and the additional cuts applied in each reconstruction stage to reduce the initial set of 20 billion events to 1.16 million contained on thirty three 8mm tapes.

The methodology used to choose analysis-specific cuts by which the final set of 2,568 events was selected for this analysis is covered in Chapter 6.

5.2 General Track Reconstruction Methodology

Most cuts used to select events somehow involved track or vertex information, so it is useful here to explain how tracks and vertices are created from an event's information (TDC times, which SMD strips were hit, etc.) stored on the data tapes.

Charged tracks were reconstructed from the SMD, PWC and DC hit information recorded from each event. SMD and PWC hit information from upstream of the target was used to reconstruct the beam track. All possible straight lines are formed using these hits (since there was usually only one beam track for almost all events, there were not too many combinations to attempt). The best track, based on the chisquare of the fit and the number of hits was kept. The beam track reconstructed in about 95% of the events. Of that 95%, about 0.5% of the time multiple beam tracks were found to exist within an event.

The seventeen downstream SMD planes provided the hit information for the the charged tracks in each event. The tracking algorithm started by finding straight line segments in each view using a minimum chisquare fit. Figure 2.7 demonstrated how difficult it can be to convert SMD plane hits into straight-line track segments. Each X and Y view required a minimum of four hits, and the V view required three hits to qualify as a segment for that view. The two dimensional tracks from each of the three views were combined to form the three dimensional SMD charged tracks.

Once all possible tracks have been formed, they are ordered by their quality. The ordering function used to assign each track's quality used the total number of SMD hits assigned to a track (more SMD hits mean a better identified track), the number of unique hits in a track (tracks that need to share SMD hits with other tracks are not as well defined as those isolated tracks that do not), and the chisquare of the track (straight lines that go through hit SMD strips are better defined than those with hit SMD strips

near, but not exactly on the SMD strips that projected tracks go through).

Drift chamber track reconstruction used the drift chamber hits (by converting the TDC counts for each wire into position information) from the three drift chamber views. Since the individual X, U and V views in each set of planes within the drift chamber sets (D2, D3 and D4) were placed very close together in Z, the three views could be treated as being at the same Z position. This assumption allowed a "triplet" to be formed, which is composed of the point of intersection of the hit in the three X, U and V views. The drift chamber reconstruction begins by first forming all possible triplets in D2, D3 and D4. Next, the Y component of the SMD tracks are projected as a straight line into the drift chambers, to see if they match with the Y position of any D3 triplet (since the major component of the magnetic field is in the Y direction, the tracks are expected to be straight lines in the Y-Z view). To allow for multiple scattering in the SMD and DC material, a window of about ± 2.5cm in Y is allowed. If any matching triplet is found, the X component of the SMD track is propagated to the DC triplet by using a single bend point approximation for the effect of the magnetic field on the track projection. In the single bend point assumption, the transverse momentum kick of the magnet is assumed to act as if it is concentrated at the Z midpoint of the magnet, and so charged tracks going through the magnet are deflected only once, at that known Z position. The p_T kick and Z position of each magnet's single bend point approximation was determined by reconstructing isolated K_s^0 particles, whose copious production and extremely well known mass easily allow these approximations to be modeled.

Projecting SMD track segments through drift chambers and the magnets, applying the single bend point approximations along the way, defines a road through space that the charged track follows. This defined road can be thought of as several millimeters wide, and was defined as being wider for lower momentum tracks. Once a road is defined, the tracking code searches along it for other triplets and hits in D3. If at least eight hits out of twelve planes in D3 are found to be within the road width around the track projection, the search for additional triplets and hits is extended to D2. If eight hits are found in D2, the tracking code searches D1 and D4 for hits. Once all nearby hits are identified, the track candidates are fitted using a chisquare minimization routine to determine the track slope, intercept and momentum. Tracks with a chisquare per degree of freedom less than 5 are kept. The SMD segments, drift chamber triplets, and hits used to form good tracks are marked as unavailable for the reconstruction code to use for other

Tab. 5.1: E791 Track Categories

Track Hit Location	Category
Only SMD hits	0
SMD hits and D1 hits	1
D1 and D2 hits, possibly SMD hits	3
Only D2 and D3 hits	6
D1, D2 and D3 hits, possibly SMD hits	7
Only D2, D3 and D4 hits	14
D1, D2, D3 and D4 hits, possibly SMD hits	15

potential track formation, while those from the rejected set of tracks are returned to the fitting pool to allow their re-use in additional searches.

For the convenience of identifying tracks with hits in different drift chambers, a track category number was assigned to each charged track. The number was packed into a single byte, and packed out with other track information onto the DSTs. The category number increments as the track leaves hits in chambers farther downstream; in this scheme, the bits 0, 1, 2, and 3 are assigned to tracks with hits in D1, D2, D3, and D4, respectively. A detailed listing of the track categories is in Table 5.1. Tracks used in this analysis are either category 3, 7 or 15.

5.3 Vertex Reconstruction

Vertices are defined as the locations which are the three dimensional common intersection point of two or more tracks. The vertex reconstruction algorithm first used the tracks identified in the previous section to try to form primary beam interaction point vertices. E791's fixed target foils helped to constrain the Z position of any possible primary vertex, and the X and Y position of the well-reconstructed beam track helped to further eliminate spurious primary vertex candidates. Primary vertex reconstruction started by finding the best two-prong vertex in a target foil between the beam track and one

of the reconstructed tracks. Other tracks in the list were then successively added to this "seed" vertex to form a vertex with a good chisquare per degree of freedom. Events which did not have a reconstructed beam track were vertexed by starting with a two-prong "seed" vertex inside of a target foil and again adding additional tracks. If a good primary vertex was found, tracks not used to form the primary were used to search for potential secondary vertices. Note that these secondary vertices need to be downstream of the primary vertex. Secondary vertex finding also proceeded by adding additional tracks to two-prong seed vertices. All possible independent secondary vertices with acceptable chisquare per degree of freedom were formed and, if the event passed criteria discussed in the next section, they were written out to the DSTs. Here the power of the DSTs can be seen—successive analysis steps can merely loop through this set of vertex lists instead of having to re-do all the track and vertex calculations. Again, selection of the events with the three-prong vertices that were used in this analysis is discussed in the next chapter.

5.4 Definition of Cuts

The initial filtering was done as each event was first reconstructed—an event having a primary vertex would be accepted by the filter and written to the Data Summary Tapes (DSTs) if it could be unpacked and successfully reconstructed, and if the event was determined to have a secondary vertex with good separation from the primary vertex. This separation provides the most effective means by which a sample of charm decays can be selected. Cut variables are usually defined using an event's track, vertex or particle ID information. By selecting events with variables whose values are greater or less than some value, one can apply "cuts" to select events with a certain similar characteristic. Care must be taken to understand how the spectrometer geometry, detector efficiency and other equipment and techniques affect the selection of certain events over others. This check is included in the study of systematic errors performed this Dalitz analysis.

Before listing the actual cut values used, a quick description of the parameters used in the event selection stages will be provided.

5.4.1 The SDZ Cut

The separation along the Z-axis of primary and secondary vertices was measured with the variable SDZ. The separation is expressed in terms of the Z separation between the primary vertex and secondary vertex divided by the error added in quadrature on each of the vertices:

$$\mathrm{SDZ} = \frac{\Delta Z}{\sqrt{\sigma_{pri}^2 + \sigma_{sec}^2}}$$

The relatively long lifetime of the D_s gives a physically measurable separation between the production vertex and the secondary decay vertex. Moving at the speed of light, with its lifetime of 0.467×10^{-12}s and average E791 D_s momentum of 60 GeV/c, a D_s particle will travel about 4mm on average before decaying. A 2D schematic of the three dimensional SDZ variable is shown here:

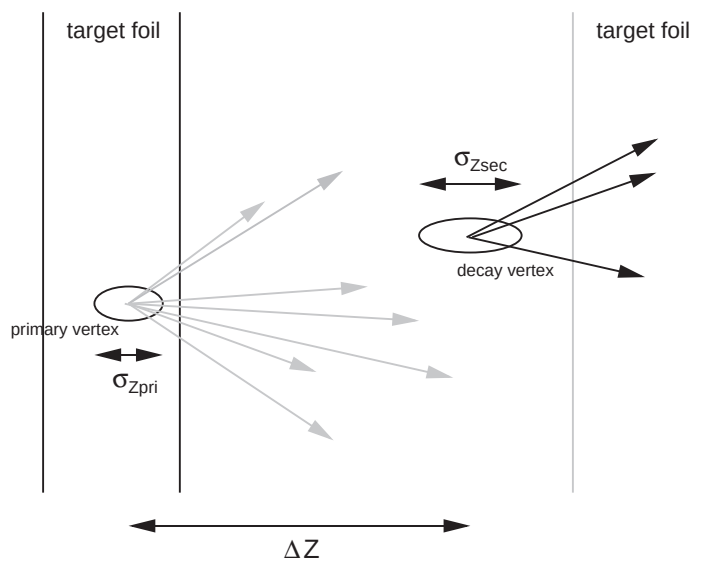

Fig. 5.2: Schematic of SDZ Cut Variable

A well-separated, well-measured set of primary and secondary vertices will make the value of SDZ larger, while poorly measured vertices or a small separation contribute to make the value of SDZ smaller. Since a well-separated

secondary vertex is a good signature for a charm signal, throwing away events lower in SDZ would more efficiently keep charm signal, and throw out events that are not potentially charm signal.

5.4.2 The DIP Cut

The projected transverse separation of the parent D_s track from the primary vertex is characterized by the D impact parameter (DIP). It is measured in the plane perpendicular to the beam direction that includes the Z of the primary vertex. In an ideal event, the reconstructed D_s momentum should point back to the primary vertex and have zero DIP. A 2D schematic of the 3 dimensional DIP variable is shown in Figure 5.3. The dark arrow represents the reconstructed D_s momentum, which is the vector sum of the momenta of the three tracks in the decay vertex. vertex.

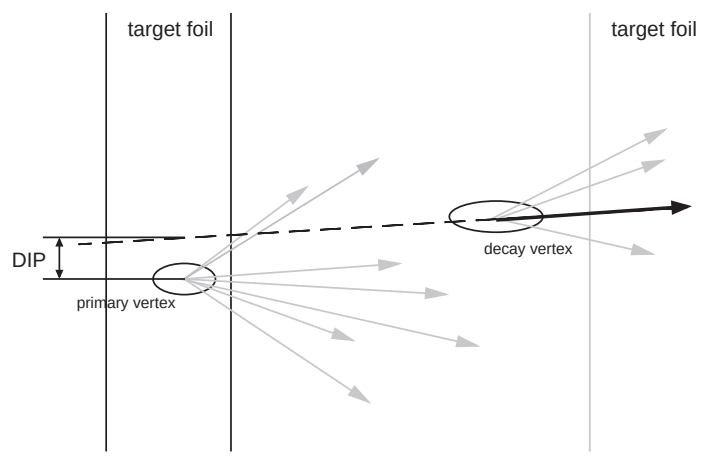

Fig. 5.3: Schematic of DIP Cut Variable

While vertex resolution effects (there is a σ_{pri} and σ_{sec} for the X, Y and Z dimensions) cause the events with actual charm particles to have a DIP that peaks at values below a few tens of microns, background events have a distribution in DIP that is more uniformly distributed. For misidentified charm backgrounds where there are missing tracks or tracks incorrectly identified as belonging to a vertex, DIP can be quite high.

5.4.3 The PTB Cut

PTB is defined as the transverse momentum of the reconstructed D_s relative to the line joining the primary and secondary vertices. A 2D schematic of the 3 dimensional PTB variable is shown in Figure 5.4.

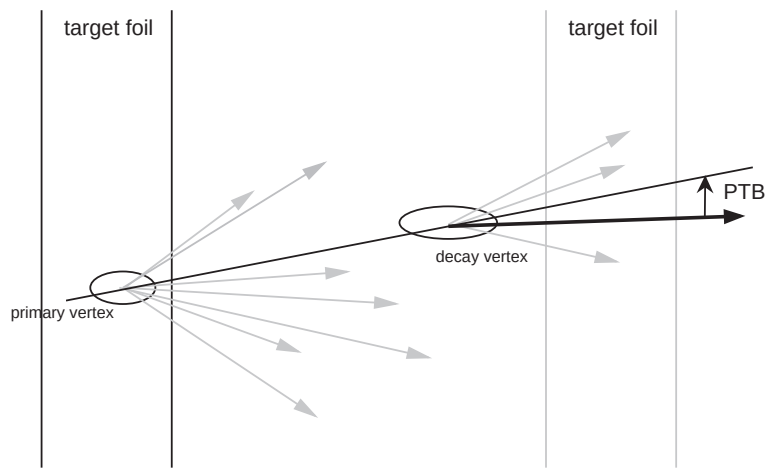

Fig. 5.4: Schematic of PTB Cut Variable

Decays that have missing tracks (somehow only 3 of the 4 (or more) decay products had reconstructed tracks that made it into the vertex list) or included an incorrect track (a track from the primary somehow made it into this secondary vertex's track list) would have higher PTB values, since the reconstructed D_s would no longer point back to the primary vertex.

5.4.4 The SIGMA Cut

The target foils are thin enough to allow a very precise determination of the Z position of the primary vertex to be made. The space between the target foils provides a large volume free of material in which to reconstruct secondary vertices. The SIGMA variable is used to insure that the secondaries are reconstructed in the volume outside of the target foils, and that they are reconstructed downstream of the true primary vertex. A 2D schematic of the 3 dimensional SIGMA variable is shown in Figure 5.5.

Each secondary vertex has an error associated with its reconstruction, due to resolution errors on the tracks from which it is composed. The Z-

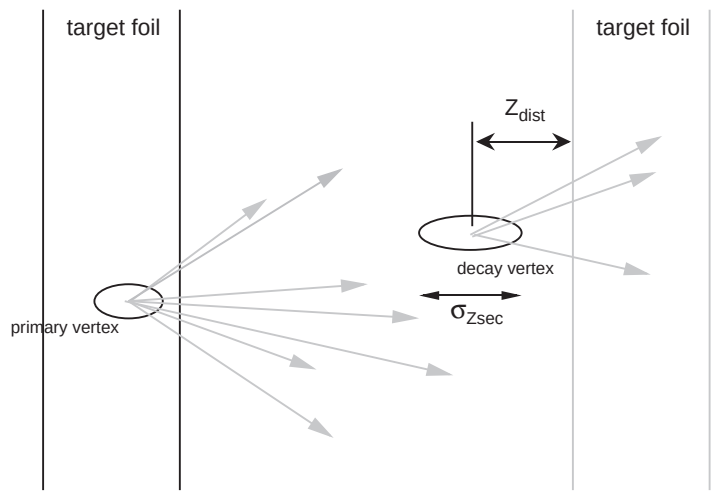

Fig. 5.5: Schematic of SIGMA Cut Variable

component of this error provides a scale by which we can determine the significance of the measured distance, Z_{dist}, between the secondary vertex and the nearest target foil edge. SIGMA is therefore defined as Z_{dist}/σ_{Zsec}.

5.4.5 The PISO Cut

Each track in the secondary vertex, when projected back to the Z position of the primary vertex, has a certain value of DCA.

The variable PISO is defined as the smallest of those DCAs, allowing one to choose a value of PISO and to understand that all other secondary vertex tracks point still farther away from the primary vertex than the value chosen. A 2D schematic of the 3 dimensional PISO variable is shown in Figure 5.6.

Again, while demanding a minimum PISO eliminates some events with true secondary vertex tracks that happen to point back to the primary vertex, it is a cut that eliminates events that potentially include primary vertex tracks in their secondary vertices.

5.4.6 The PISE Cut

The variable PISE is determined much like PISO, except that the track and vertex error are now folded into the calculation:

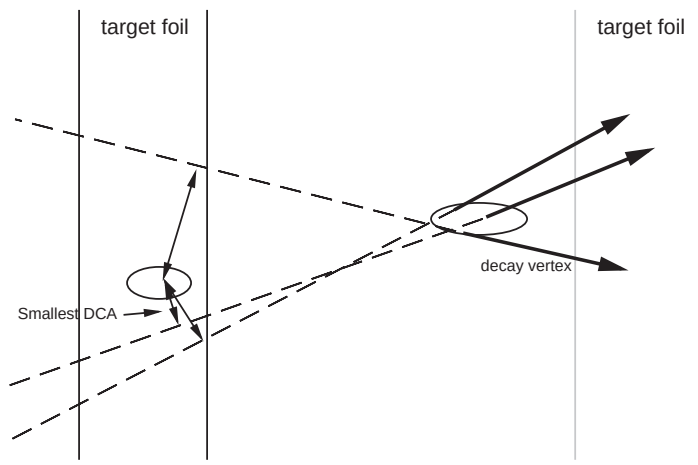

Fig. 5.6: Schematic of PISO Cut Variable

$$\text{PISE} = MIN(\frac{DCA_{pri}}{ERR_{DCA}})$$

This error inclusion is an attempt to parameterize that well-measured tracks absolutely cannot point back to the primary, while poorly measured tracks may not actually be pointing back to the primary as much as their imprecise values project them. The above formula shows that including the measurement error causes more poorly measured tracks to have a smaller value of PISE than well-measured tracks, for the same DCA.

5.4.7 The RATIO Cut

The schematics in this chapter have thus far had their primary and secondary vertex tracks join at a single point in the center of the elipse representing the X, Y and Z error on the vertices. Due to resolution limits from the finite widths of the SMD strips and reconstruction code, the primary and secondary tracks do not join exactly at the reconstructed secondary vertex X, Y and Z position. Each of the tracks in the secondary vertex has a distance of closest approach (DCA) to both the secondary vertex, and, if projected back, to the primary vertex. The 2D schematic for the 3 dimensional PISO variable in Figure 5.6 showed these DCAs.

Another cut used to reduce the number of events that have primary vertex tracks that pass through or near the secondary vertex is the RATIO cut. The

ratio DCA_{sec}/DCA_{pri} is calculated for each track in the secondary vertex, and the three ratios are multiplied to form the variable RATIO:

$$RATIO = \prod_{trk=1}^{3} \frac{DCA_{sec}}{DCA_{pri}} \tag{5.1}$$

While this eliminates some real D_s events with secondary vertex tracks that happen to project back to the primary vertex, it is a cut that also helps to eliminate the events with primary vertex tracks that pass through the secondary vertex. It is strongly correlated with the PISO and PISE cuts, which were found to provide signal events with better statistical significance than those from using RATIO. A loose RATIO cut was used in the initial filtering stages. The PISO and PISE cuts were used to select the final events for this analysis.

5.5 Filtering and Stripping

As mentioned in the previous section, the 24,000 E791 8mm tapes were filtered by selecting events using SDZ—those with SDZ > 6 for two-prong secondaries and those with SDZ > 4 for secondaries with three or more tracks. This was a loose but very general and effective cut to use—most charm analyses that require a secondary vertex will use an even tighter SDZ cut. For example, the final SDZ cut used in this analysis was 8—a 4σ greater separation than the initial filtering cut.

Once filtered, the events on the approximately 7,500 DSTs were put through further selection criteria to reduce the number of tapes and enrich the percentage of "interesting" events in the data set. Stripping reduced the data set to approximately 2,000 DSTs. The stripping selection criteria used for the three-prong events in this analysis are shown in Table 5.2 in this section.

Since the stripped data output still contained events that were not of interest for this analysis, further selection criteria were applied to the 2,000 tapes to create a data set appropriate for this physics analysis. Tighter cuts on various event parameters reduced the number of events which were not relevant for this analysis without biasing the event sample towards providing any particular outcome. That the cuts used do not bias the sample will be

Tab. 5.2: Summary of Cuts at Each Stage of the Analysis

Cut	Filter/DST	Strip	Substrip
SDZ	> 4	> 6	> 8
PTB (GeV/c)	< 1	< 1	< 0.35
TAU (ps)	< 5	< 5	< 5
Z_{sec} (cm)	-	-	$<$ -0.35
DCA (cm)	-	-	> 0.01

demonstrated in the next chapter. The substripping cuts were still general enough to allow the final output events to be used for many different analyses. The final column in Table 5.2 lists the cut variables used to reduce the data set to events on 33 DSTs.

The method outlining how the final thesis analysis cuts were chosen and applied to these 33 tapes is discussed in the next chapter.

6. EVENT SELECTION FOR THE ANALYSIS

6.1 Introduction and Overview

This analysis utilizes the elements of the E791 spectrometer which can be used to measure charged track parameters and to determine the existence of secondary vertices. More specifically, the analysis uses three-track secondary vertices that have a combined charge of +1 or −1. This means that the three-track vertex either has two positively charged tracks and one negatively charged track, or two negatively charged tracks and one positively charged track. Since the analysis is to be done on three-prong vertices, the final analysis cuts were chosen to provide an unbiased set of events that have very clean, well-defined secondary vertices.

While this analysis inherits all earlier cuts made by starting with the 1.16 million events on the 33 sub-stripped tapes, it will be shown that most inherited cut values were actually tightened in arriving at the final data sample.

6.2 Motivation of Cut Selection Methodology

All cuts bias an event sample in some way; for this analysis, it is important to make sure that the final cuts selected do not affect the acceptance across the Dalitz plot in a non-uniform way. The determination of the efficiency function across the Dalitz plot performed in section 8.4 shows that the chosen cuts do not.

The method presented here to choose the final set of cuts for the analysis was to apply each cut to two different sets of events—a set of Monte Carlo (MC) events from the region ± 50 MeV/c^2 around the 1.97 GeV/c^2 D_s mass in the MC $\pi\pi\pi$ mass distribution to represent signal, and a set of data events from the wings of the D_s region (events above 2.006 GeV/c^2) in the data $\pi\pi\pi$ mass distribution to represent background. The cut was stepped

through all of its possible values, and the value of the number of MC signal events remaining (S) and the value of the number of data background events remaining (B) were determined by fitting the Monte Carlo signal and Data wing 1-dimensional mass histogram obtained for the D_s mass hypothesis continuum at each cut value.

6.3 Final Cut Selection Methodology

A large sample of MC $D_s^+ \to \pi^+\pi^-\pi^+$ events was generated to represent background-free D_s signal events for the study. As discussed in Chapter 4, Monte Carlo event properties and variable distributions were tuned to closely match the observed data signal events, which any selection cuts should retain with high efficiency. The non-resonant $D_s^+ \to \pi^+\pi^-\pi^+$ MC decay mode was chosen so that the three pions would be isotropically distributed and would adequately populate all regions of phase space. A sample of 750,000 MC events with only one $D_s^+ \to \pi^+\pi^-\pi^+$ per event was generated and put through the same analysis stages as the data events. There were 22,660 MC events left in the final substripped MC sample which were used to represent the signal events (S).

Events in the data wing region are not likely to be real $D_s^+ \to \pi^+\pi^-\pi^+$ events and are therefore used to simulate the properties of events that should not pass the selection cuts. Even though these events do not come from the signal region, they are used to simulate the background that is actually under the signal region. This can be done since the background distribution seems to be well represented by a smoothly varying distribution (the exponential in the $\pi\pi\pi$ mass plot in Figure 1.2) and because the events above the D_s signal region come from the same sources as those under the D_s signal. Note that there are actually two wing regions—the one above the D_s mass in the $\pi\pi\pi$ mass hypothesis plot will be called the highwing region, and the one between the D_s mass and the D^+ mass in the $\pi\pi\pi$ mass hypothesis plot will be called the midwing region. Included for illustration purposes, the upper left plot in Figure 6.1 shows the final $\pi\pi\pi$ data mass hypothesis plot with its signal, midwing and highwing regions shaded to highlight these three regions.

Specifically, the region

$$1.89 GeV/c^2 \leq m(\pi\pi\pi) \leq 1.933 GeV/c^2$$

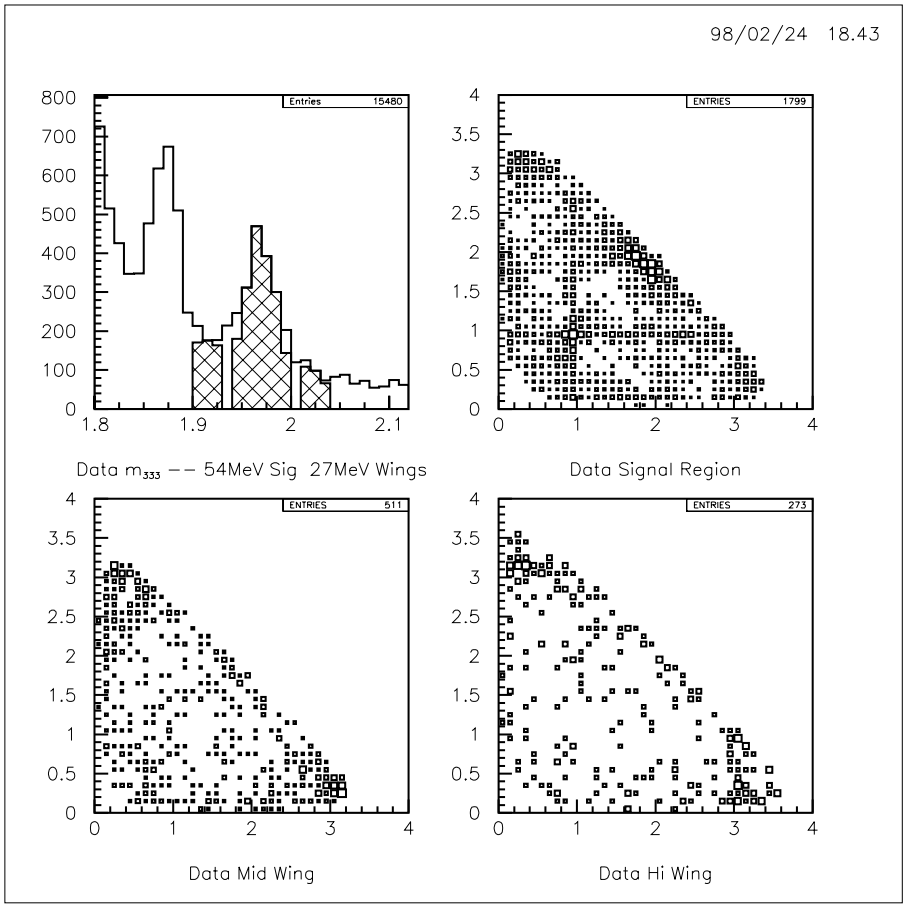

Fig. 6.1: Data $\pi^+\pi^-\pi^+$ Mass Hypothesis

will be called the midwing region. It contains 511 data events. The region

$$m(\pi\pi\pi) \geq 2.006 GeV/c^2$$

will be called the highwing region. It contains 273 events. Since the midwing region contains events from the $D^+ \rightarrow \pi^+\pi^-\pi^+$ decayand the signal region will not contain any such contamination, the highwing region was used to provide the characteristics of the background under the D_s signal region.

Cuts that were studied as possible candidates to increase signal event statistical significance (i.e., increase S/$\sqrt{B}$) were:

- SDZ
- PTB
- DIP
- SIGMA
- RATIO
- τ_{D_s} (the lifetime of the reconstructed D_s)
- CHVX
- Event Primary Vertex Multiplicity
- PISO
- PISE

The effect each cut has on the MC signal and the data highwing event samples is plotted for values over each cut's range in the following pages. In each figure, the two right-hand plots show the distribution of the particular cut variable for the MC signal region events and for the data highwing events. The bottom left plot shows the effect o fapplying the cut—at each value of the cut variable, the number of MC signal regions events remaining is expressed in terms of the fraction of the original number of MC signal events)e.g., at SDZ = 20, ≈70% of the original 22,660 MC signal events are left). The upper right plot in each figure shows the distribution of S/$\sqrt{B}$ for that cut. At each value of the cut, the value of the remaining number of MC signal events is divided by the square root of the number of remaining data highwing events. A peak in the distribution of S/$\sqrt{B}$ indicates the best cut value to use—it maximizes the amount of MC signal events kept for the amount of background events that also remain.

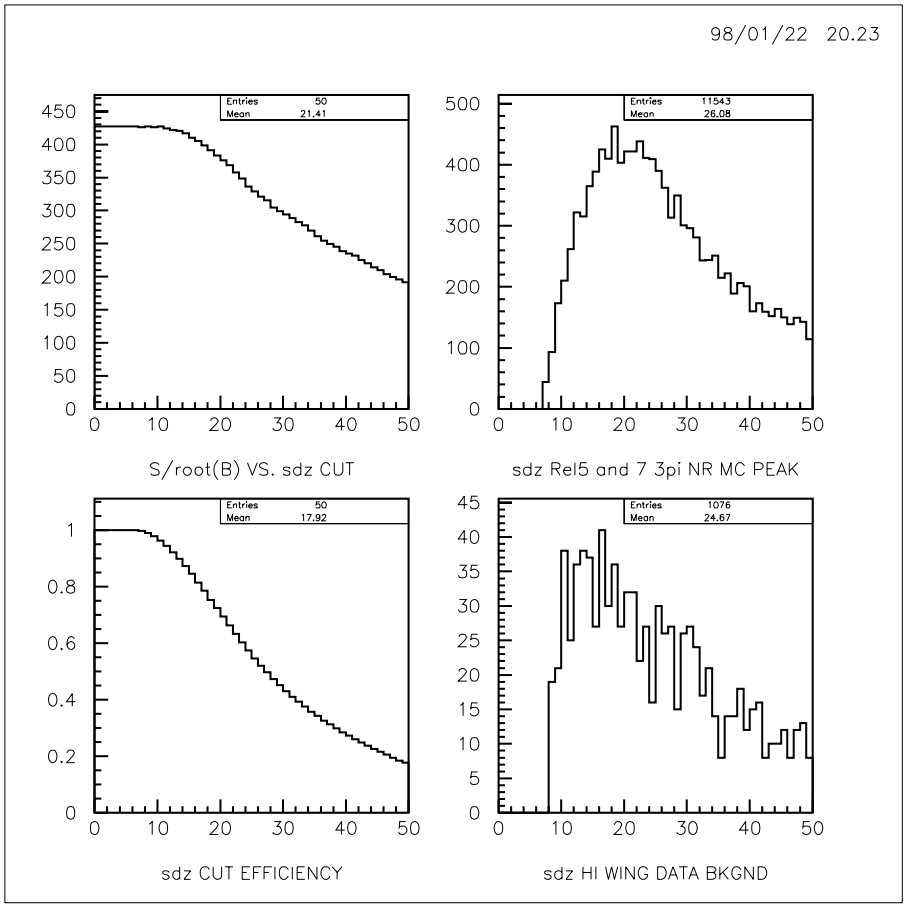

Fig. 6.2: Final Cut Selection Dependence on SDZ

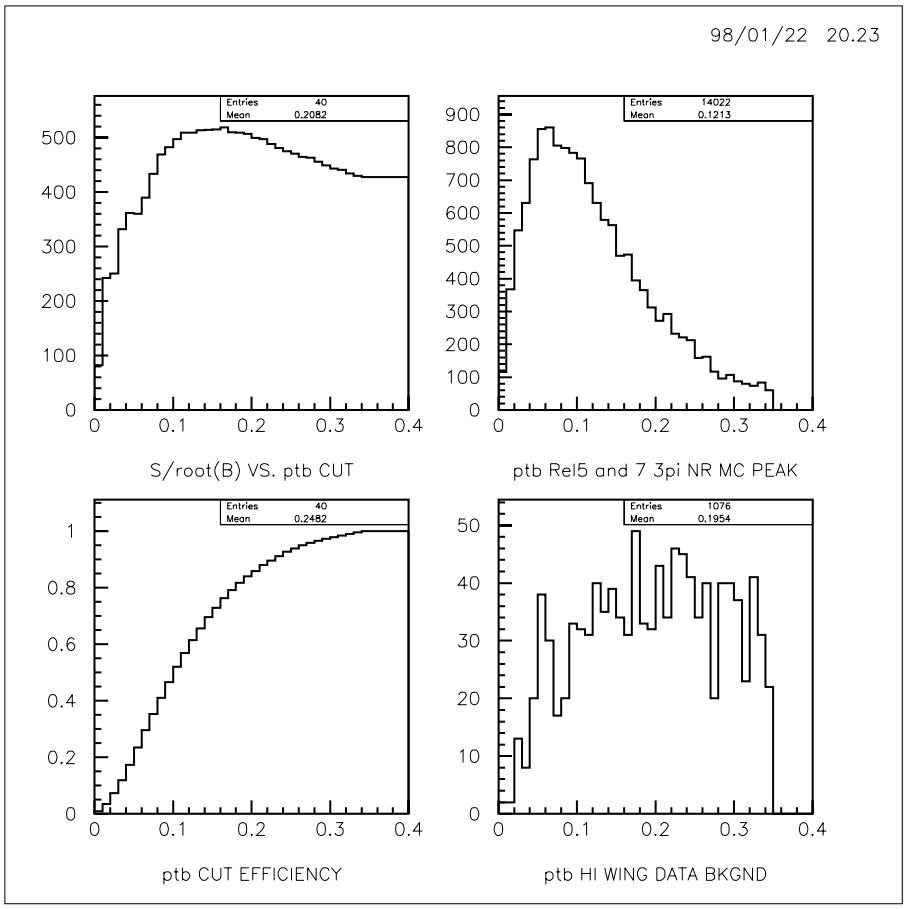

Fig. 6.3: Final Cut Selection Dependence on PTB

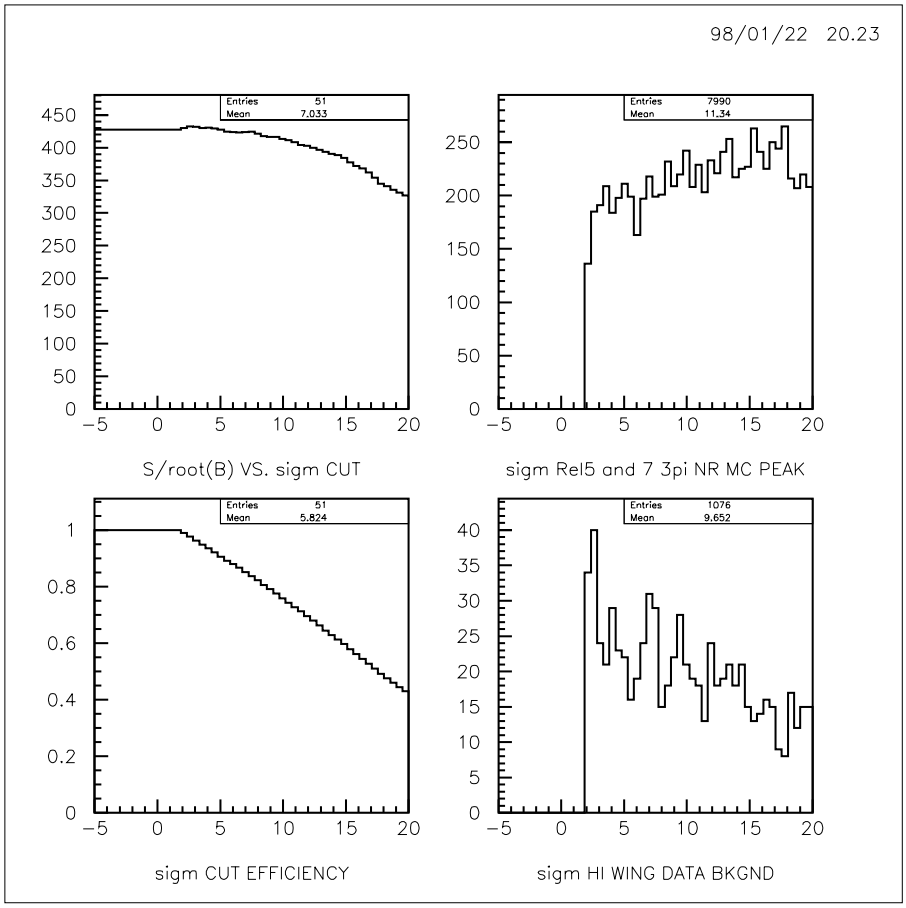

Fig. 6.4: Final Cut Selection Dependence on SIGMA

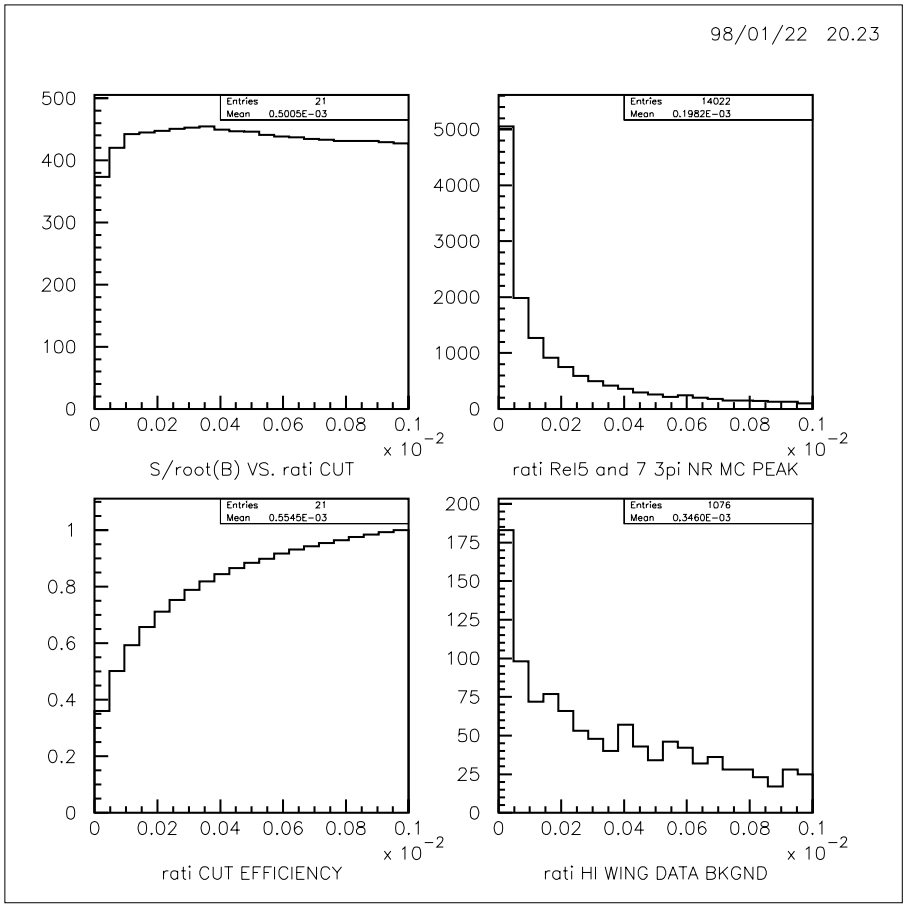

Fig. 6.5: Final Cut Selection Dependence on RATIO

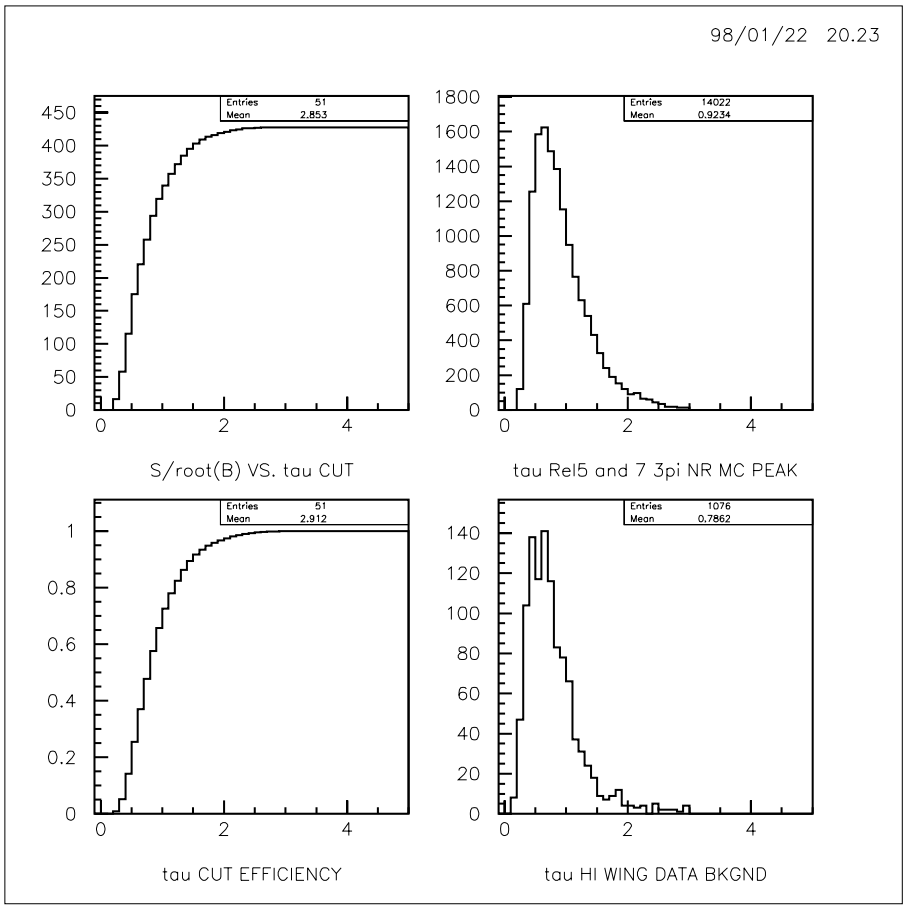

Fig. 6.6: Final Cut Selection Dependence on D_s lifetime

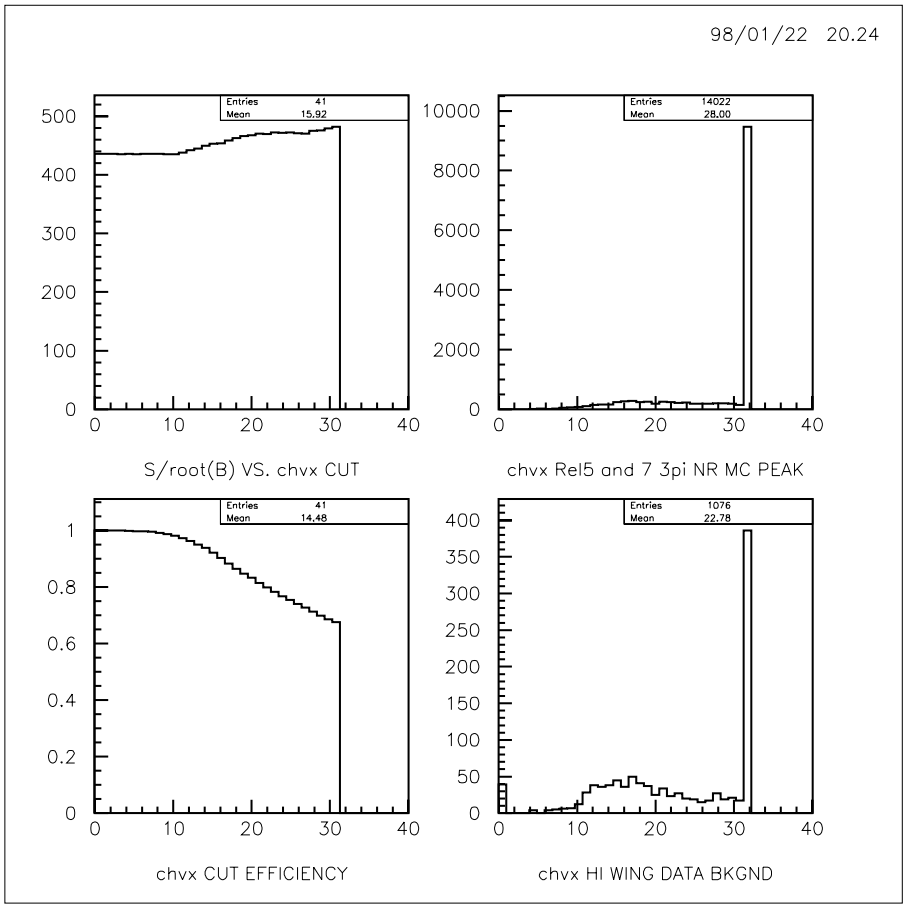

Fig. 6.7: Final Cut Selection Dependence on Minimum Decay Track χ^2 Contribution to Primary Vertex

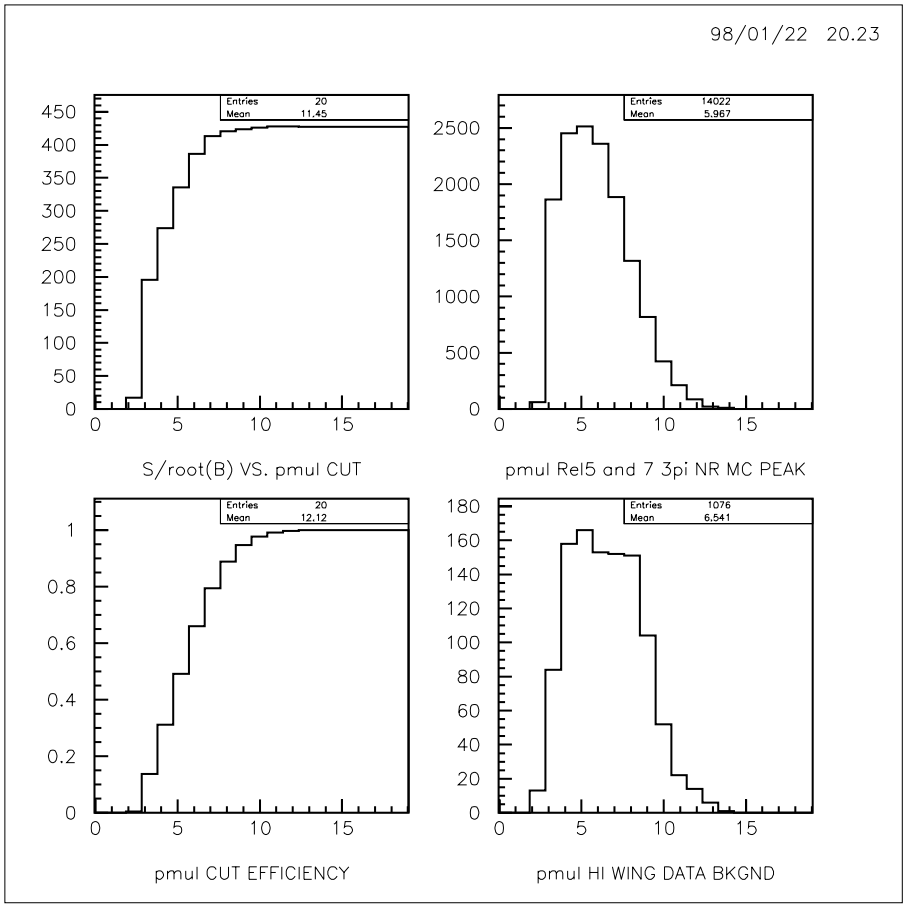

Fig. 6.8: Final Cut Selection Dependence on Event Primary Vertex Multiplicity

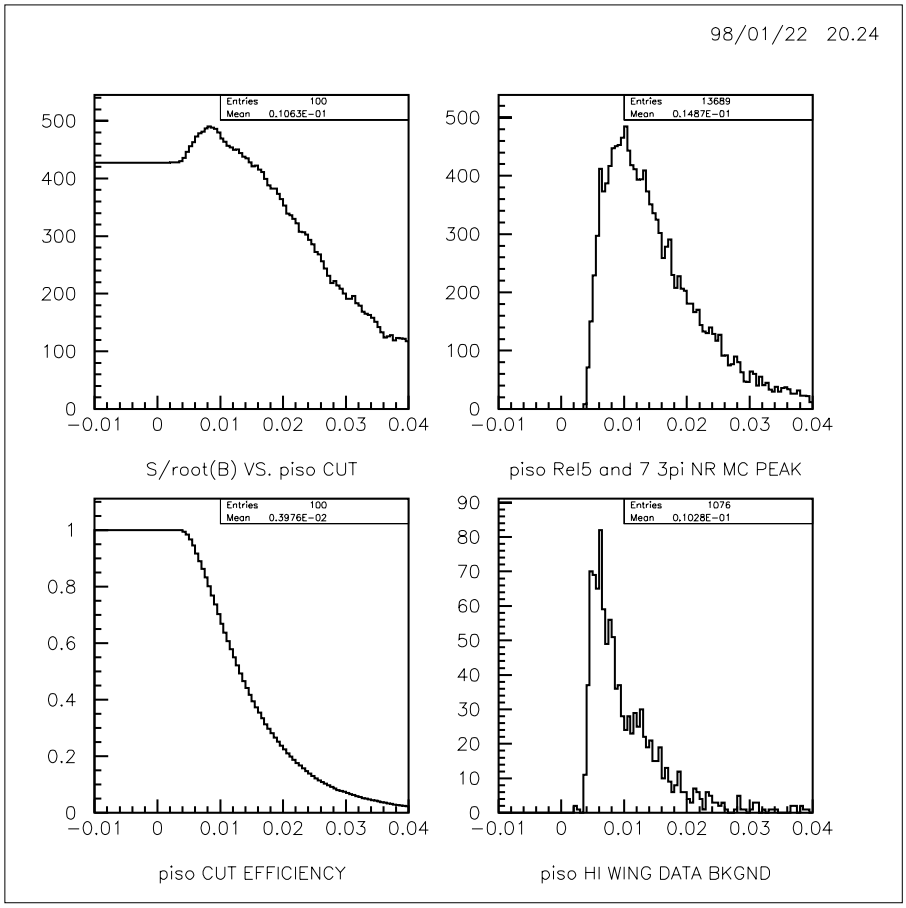

Fig. 6.9: Final Cut Selection Dependence on PISO

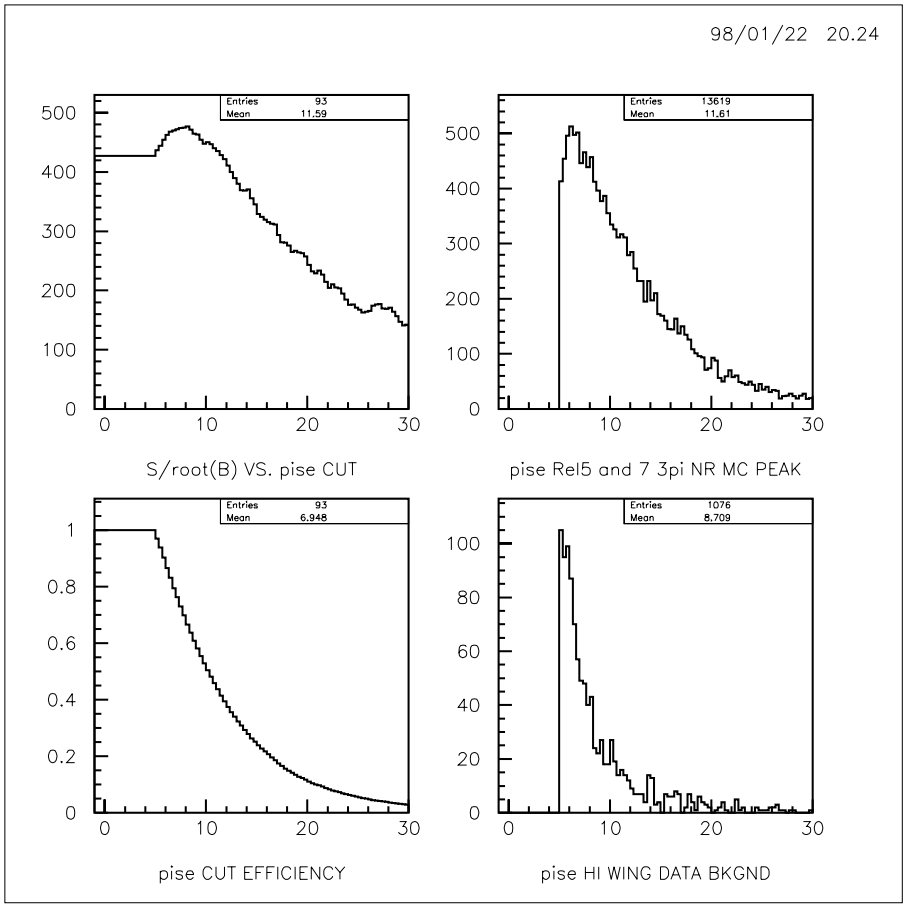

Fig. 6.10: Final Cut Selection Dependence on PISE

The largest $S/\sqrt{B}$ gain can be seen to come from the PISO and PISE cut variables. To test that the cut starting values of these two contributors did not bias the ability to find $S/\sqrt{B}$ gains in other variables, a looser PISO cut was applied to the nano-stripped MC and data samples, and the $S/\sqrt{B}$ minimizations was re-performed. The peak values of $S/\sqrt{B}$ remained the same for all cuts studied. A similar test was performed with the PISE cut variable, and again no $S/\sqrt{B}$ peak value changes were noted for any other cut variables.

6.4 Final Cut Selection

One additional methodology was then applied to improve upon the set of cuts obtained in the previous section. The methodology is motivated by the desire to get rid of events with poorer mass resolution and to have less background present in the Dalitz plot to be modeled in the maximum likelihood fit. Since the location of an event on the Dalitz plot does not depend on its reconstructed mass, using data to perform a final tune on the $S/\sqrt{B}$ peaks to improve the significance of the data D_s signal sample will not bias the Dalitz plot. The methodology used PAW to fit the data three pion mass hypothesis histogram with two exponents and two gaussians between 1.72 and 2.12 GeV/c^2. The coefficients of the exponents and the number of D_s and D^+ were floated in the fit.

The value of error(D_s)/number(D_s) was used to further examine gains or losses in significance as the cuts were stepped tighter than those obtained by the previous section's methodology. Cuts were stepped tighter, first one at a time, and then in combinations, to map out and search for the lowest value of error(D_s)/number(D_s) that could be obtained. The changes were slight, resulting in only a small extra data D_s signal significance being obtained. The final values of the cuts used in this analysis are presented in Table 6.1.

6.5 Background Studies

Note that the cuts used in this analysis do not result in the keeping of all signal events and the removal of all background events—they were chosen because they maximized the ratio $S/\sqrt{B}$. This section looks more closely at the numbers and the properties of these "background" events to try to determine their actual makeup. The use of the MC will again greatly assist in this ef-

Tab. 6.1: Final Analysis Cut Values

Cut	Filter/DST	Strip	Substrip	**Final**
SDZ	> 4	> 6	> 8	> 8
PTB (GeV/c)	< 1	< 1	< 0.35	< 0.35
TAU (ps)	< 5	< 5	< 5	< 3
Z_{sec} (cm)	-	-	$<$ -0.35	$<$ -0.4
DCA (cm)	-	-	> 0.01	> 0.01
RATIO	-	-	< 0.001	< 0.001
SIGMA	-	-	-	> 2
DIP (cm)	-	-	-	< 0.0040
CHVX	-	-	-	> 2
PISO (cm)	-	-	-	> 0.0060
PISE	-	-	-	> 4

fort. It is very important to be able to identify all the significant background sources that might appear in the final sample, because a parameterization of each of them will explicitly appear in the maximum likelihood fit—each source needs to be accurately known so it can be accurately modeled.

6.5.1 Visible Structure in the D_s Mass Plot

Figure 1.2 shows two peaks over a smooth exponential function used to represent the background distribution. The $\pi\pi\pi$ mass spectrum was fit using two gaussians—one to represent the D_s, and one to represent the D^+. Another component in the $\pi\pi\pi$ mass spectrum fit was an exponential to represent the $D^+ \to K^-\pi^+\pi^-$ events where the kaon has been incorrectly identified as a pion. The difference in mass between the charged kaon and charged pion creates a "reflection" into the $\pi\pi\pi$ mass hypothesis plot, visible as a much broader peak below the known D^+ mass of 1.87 GeV/c^2.

To study this possibility, a sample of E791 $D^+ \to K^-\pi^+\pi^+$ events was used and the invariant mass recalculated assuming that all three decay tracks are pions. Figure 6.11 demonstrates that by plotting data $D^+ \to K^-\pi^+\pi^+$ events that survive the final analysis cuts, no $D^+ \to K^-\pi^+\pi^+$ reflection events need to be considered as background events for the $D_s \to \pi^-\pi^+\pi^+$ analysis.

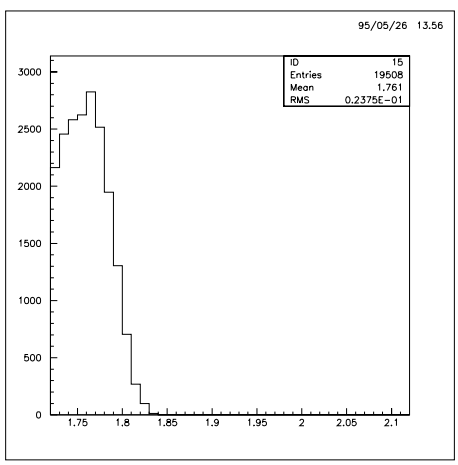

Fig. 6.11: Data $D^+ \to K^-\pi^+\pi^+$ events, plotted as $\pi^+\pi^-\pi^+$ events, after Final Selection Cuts

In Figure 1.2, the D^+ peak has been well fit by a gaussian with a width of 14 MeV at the known D^+ mass of 1.87 GeV/c^2. This width guarantees that minimal $D^+ \to \pi^-\pi^+\pi^+$ events will exist in the D_s signal region, since the signal region begins at 1.92 GeV/c^2, which is over 3.6σ away from the D^+ peak. This is in contrast to the midwing region in Figure 6.1, which begins at 1.89 GeV/c^2, only 1.4σ away from the D^+ peak.

No other obvious sources of background visibly peak the three pion mass hypothesis plot. Other reflections and background from other D_s decays are discussed in subsequent subsections.

6.5.2 Visible Structure in the Background Dalitz Plot

Sideband "wing" events from data were used to represent the properites of the combinatoric background events under the D_s signal region in the study of S/$\sqrt{B}$. Figure 6.1 showed the Dalitz plots of the midwing and highwing regions. No clear structures are noted in the highwing Dalitz plot, other than the ones near the symmetric corners of the plot. The structures at the corners will be associated to a specific charm background, and discussed in Section 6.5.3. The rest of the background events in the Dalitz plot are assumed to be uniformly distributed.

Having determined that there are no individual sources of combinatoric background with distributions that peak exactly at the D_s mass, there is no reason to assume that the distribution observed on either side of the D_s mass cannot be smoothly joined. Being able to fit the background with a smooth function over a wide mass range (the exponential represents the background distribution over the entire range 1.82 GeV/c^2 - 2.12 GeV/c^2 provides further confidence in this assumption. The number of events under this smooth exponential curve represents the number of background events under the D_s signal peak for the particular fit parameters being used to describe the curve. One set of contributions to the systematic error that will need to be understood is how much the particular number of background events and the particular background shape parameterization affects the final maximum likelihood answer obtained. This and other background contributions to the systematic error are covered in the error analysis chapter.

6.5.3 Analysis of Visible Structure in Background Dalitz Plot

It will be shown that the structure in the corners of the Dalitz Plot can be described by contributions from the D^0 two-prong decays. The D^0 decays can appear in the $\pi\pi\pi$ spectrum by combining another random pion from the event's primary vertex with the two prong vertex from the D^0 decay.

The general method to study the D^0 background was to generate 375,000 Monte Carlo events for each background mode studied and to examine their distributions when plotted as $\pi\pi\pi$ events. The samples were put through the same filtering and stripping stages as the data. The final analysis cuts were applied to the surviving Monte Carlo events, and the yields obtained were used to estimate the number of each mode that should be expected in the final data sample. The modes studied, chosen for their kinematic similarities or high branching ratios, are presented here:

$$
\begin{aligned}
&D^* \to D_0\pi, D^0 \to Ke\nu \\
&D^* \to D_0\pi, D^0 \to K\mu\nu \\
&D^* \to D_0\pi, D^0 \to \pi\pi \\
&D^* \to D_0\pi, D^0 \to \pi\pi\pi^0 \\
&D^* \to D_0\pi, D^0 \to K\pi\pi^0 \\
&D^* \to D_0\pi, D^0 \to K\pi\pi^0\pi^0 \\
&D^* \to D_0\pi, D^0 \to K^0\pi\pi \\
&D^* \to D_0\pi, D^0 \to K\rho \\
&D^* \to D_0\pi, D^0 \to K\pi \\
&D^0 \to K\pi, \text{ no } D^* \\
&D^0 \to K\rho, \text{ no } D^*
\end{aligned}
$$

Track matching was used to insure that the secondary vertex tracks corresponded to the background decay mode tracks in the Monte Carlo truth table. This was acomplished by requiring reconstructed track parameters to closely agree with their thrown values. Table 6.2 lists the three track parameters used to make the comparison and the value of the parameters used to decide there was a match between thrown and reconstructed tracks. The requirement was that one charged track in the background mode's secondary vertex has its truth table values match those for one of the reconstructed tracks. All three matching criteria must be met or exceeded for a match to occur.

Tab. 6.2: Track Matching Criteria

Matching Parameter	Value
Maximum Allowed X or Y Slope Difference	< 0.0003
Maximum Allowed X or Y Intercept Difference	< 50 microns
Maximum Allowed Fractional Momentum Difference	< 0.02

For this study,the $\pi\pi\pi$ mass hypothesis spectrum of each background mode was divided into three regions to allow a broader comparison to be made. While similar to what was done to calculate $S/\sqrt{B}$, in this case the regions are chosen to be slightly different in size. The Signal region was defined as ± 27 MeV/c^2 around the D_s mass of 1.970 GeV/c^2. With the fit D_s gaussian width of 13.5 MeV/c^2, this is a $\pm 2\sigma$ window. The Midwing region was defined as a 27 MeV/c^2 window between 1.902 GeV/c^2 and 1.929 GeV/c^2. The mass value 1.929 GeV/c^2 is 3σ below the D_s mass peak. The highwing region was defined as a 27 MeV/c^2 window between 2.011 GeV/c^2 and 2.038 GeV/c^2. The mass value 2.011 GeV/c^2 is 3σ above the D_s mass peak.

There are two $\pm$ combinations in each three track vertex. The distributions of the two $M^2_{\pi^+\pi^-}$ hypotheses can be plotted against each other for MC events with an $M_{\pi\pi\pi}$ hypothesis that falls into one of the three defined regions. This division can also be performed on the data event sample. Furthermore, since the D^0 events bunch in the corners of the Dalitz plot, a region in the Dalitz plot corners can be defined to allow a comparison of the number of data events seen with the number of background events expected. The number fo background events expected is estimated by the number of Monte Carlo background events seen in the corners of each region. The Dalitz corners are defined as the two regions > 2.7 (GeV/c^2)^2 and < 0.85 (GeV/c^2)^2 on the Dalitz plot. Figure 6.12 shows the shaded Signal, Midwing and Highwing regions in the $M_{\pi\pi\pi}$ plot for the final data sample, and the Dalitz corners for each region—the events above 0.85 (GeV/c^2)^2 and below 2.7 (GeV/c^2)^2

have been cut out of the Dalitz plot. The numbers left in each Dalitz corner plot represent the number of data events for which the D^0 background contributions have to account.

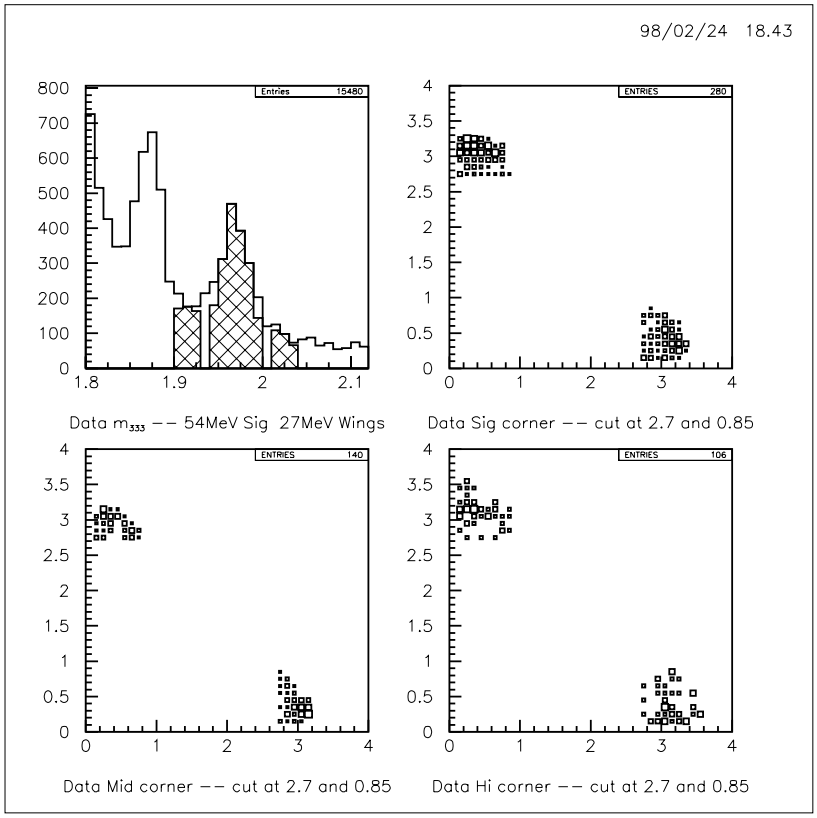

Fig. 6.12: E791 Data Events in the Dalitz Corners for Signal, Midwing and Highwing Regions

The following pages present the same plot as Figure 6.12 for each of the D^0 background modes. Table 6.3 summarizes the number of Monte Carlo events seen in the Dalitz corners for each D^0 background plot. Empty plots indicate that no events populate the Dalitz corners.

Tab. 6.3: Summary of Surviving Monte Carlo Events in Dalitz Corner Plots

Monte Carlo D^0 Decay Mode	Number Observed Midwing	Signal	Highwing
$Ke\nu$	0	1	0
$K\mu\nu$	0	0	0
$\pi\pi$	0	14	81
$\pi\pi\pi^0$	2	0	0
$K\pi\pi^0$	0	0	0
$K^0\pi\pi$	0	1	0
$K\pi\pi^0\pi^0$	1	0	0
$K\rho$	1	1	1
$K\pi$	24	41	6
$K\rho$ (no D^*)	1	0	0
$K\pi$ (no D^*)	47	94	22

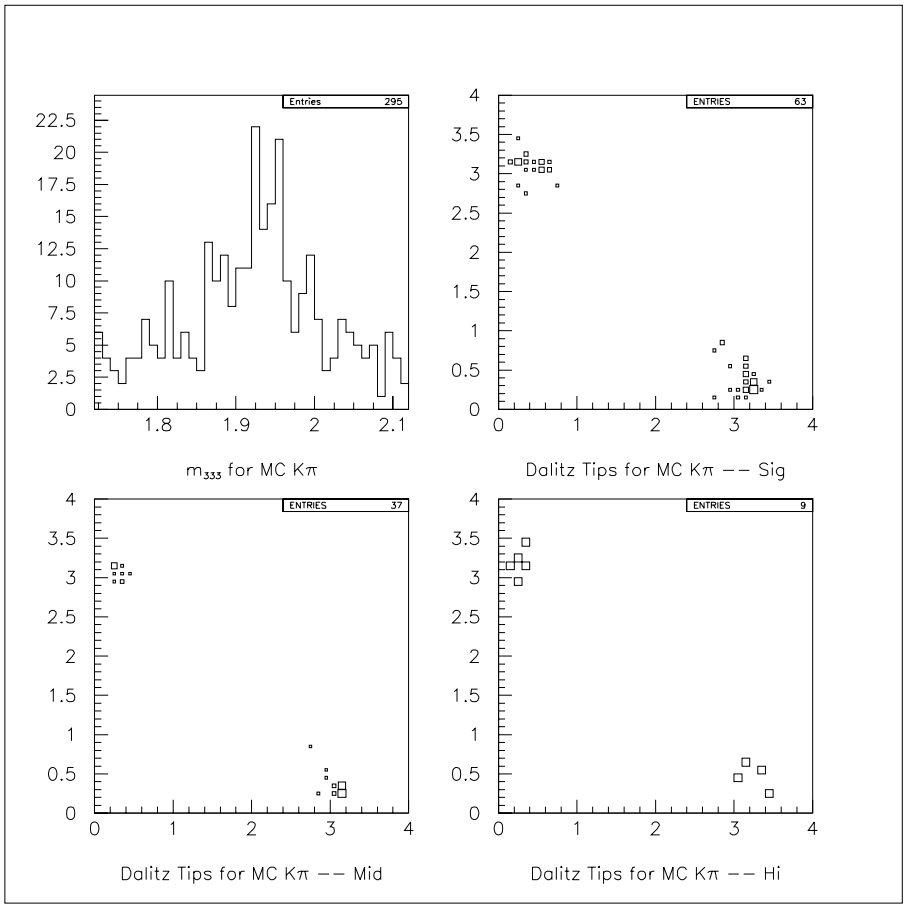

Fig. 6.13: Monte Carlo $D^* \to D^0\pi, D^0 \to K\pi$ Events in the Dalitz Corners for Signal, Midwing and Highwing Regions

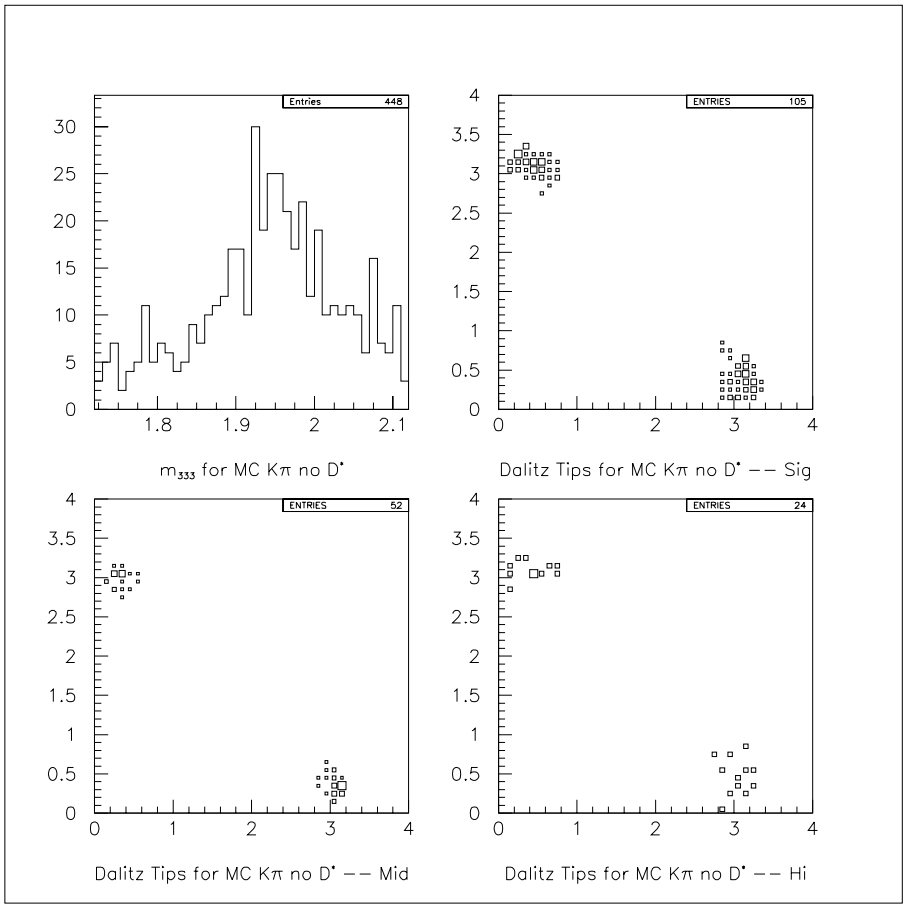

Fig. 6.14: Monte Carlo $D^0 \to K\pi$ (no D^*) Events in the Dalitz Corners for Signal, Midwing and Highwing Regions

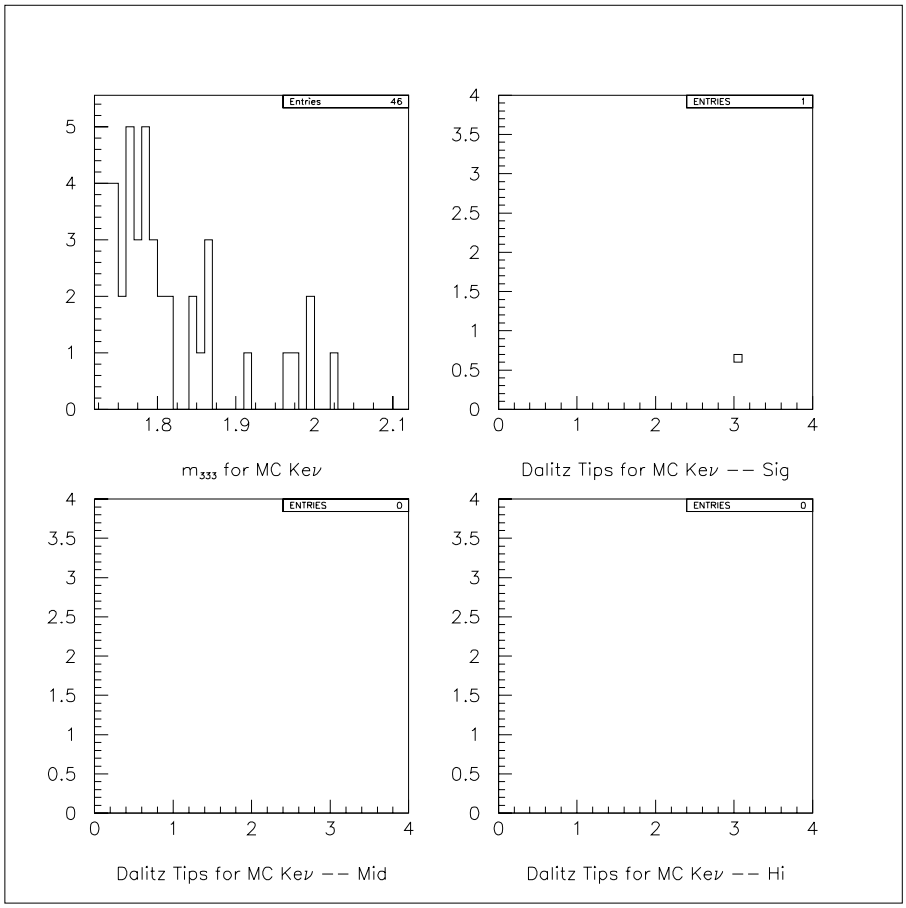

Fig. 6.15: Monte Carlo $D^0 \to Ke\nu$ Events in the Dalitz Corners for Signal, Midwing and Highwing Regions

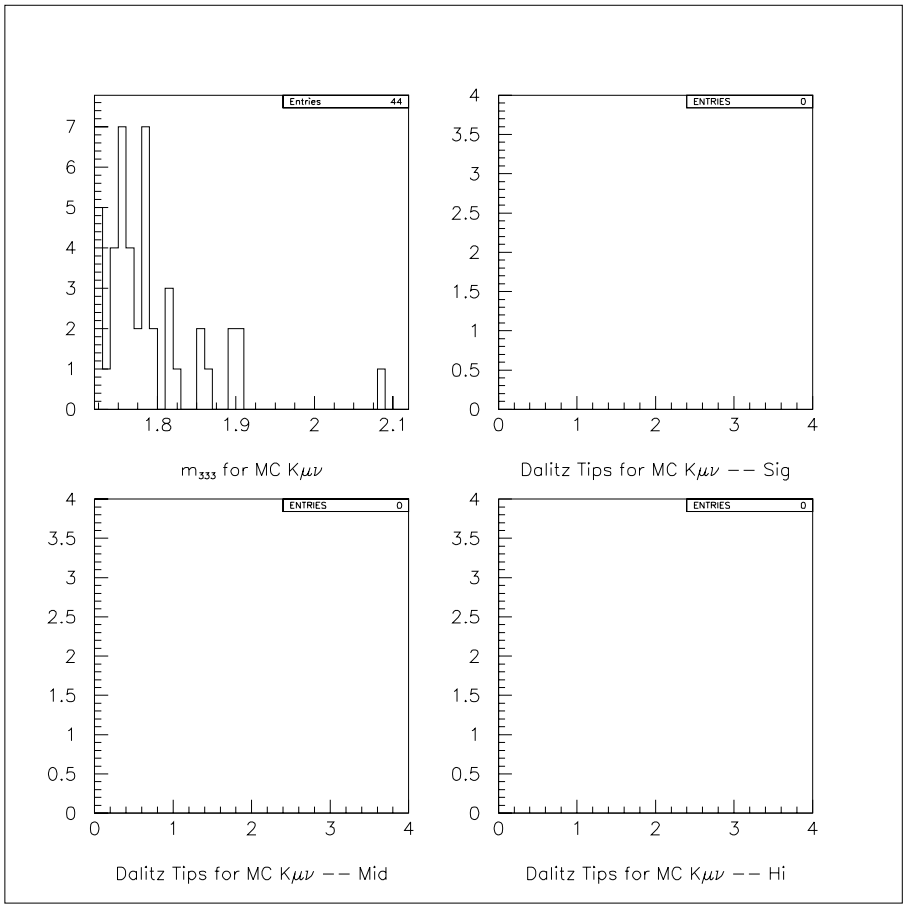

Fig. 6.16: Monte Carlo $D^0 \to K\mu\nu$ Events in the Dalitz Corners for Signal, Midwing and Highwing Regions

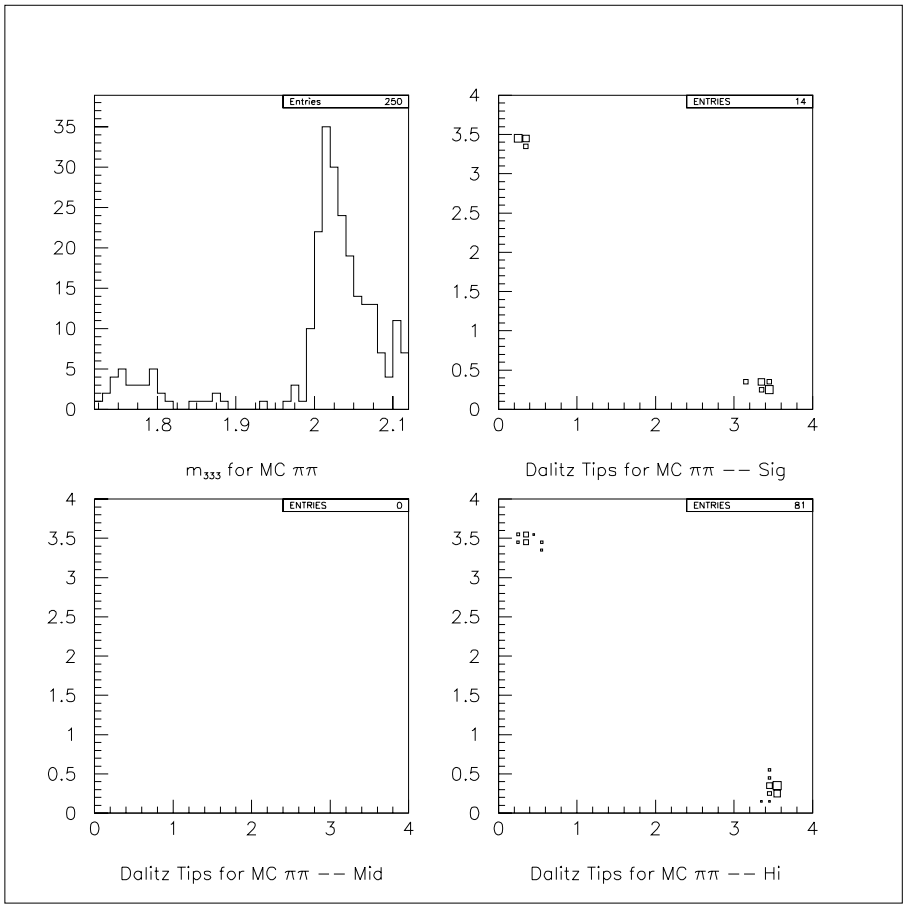

Fig. 6.17: Monte Carlo $D^0 \to \pi\pi$ Events in the Dalitz Corners for Signal, Midwing and Highwing Regions

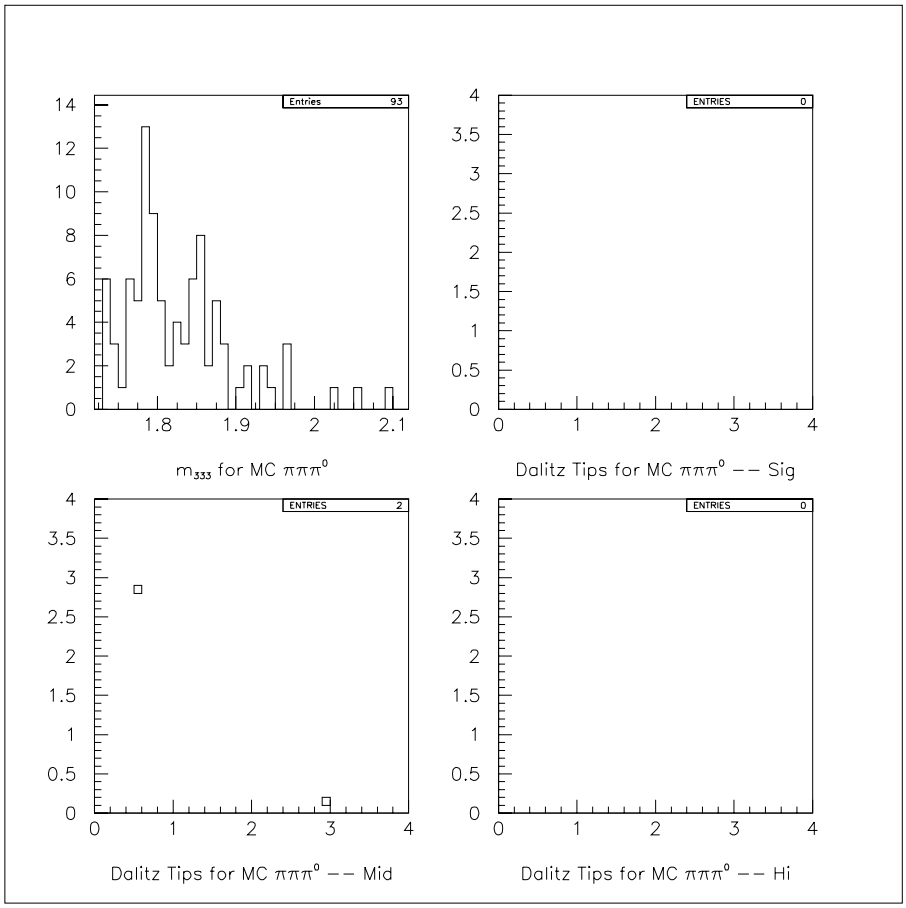

Fig. 6.18: Monte Carlo $D^0 \to \pi\pi\pi^0$ Events in the Dalitz Corners for Signal, Midwing and Highwing Regions

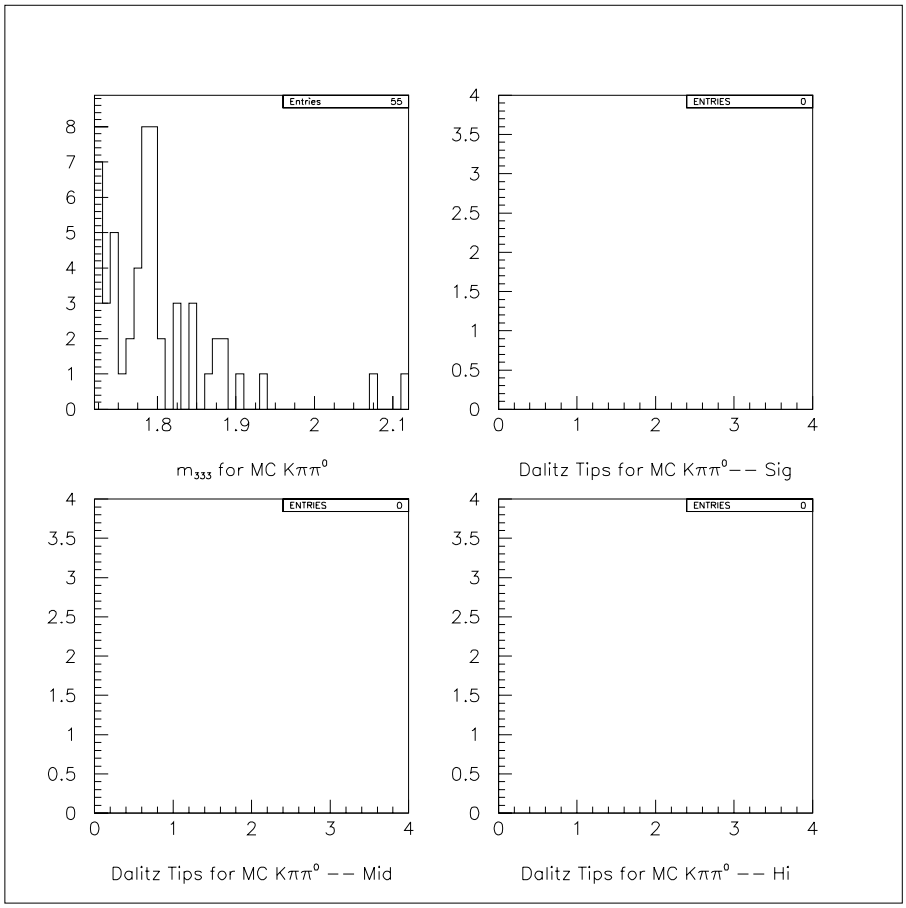

Fig. 6.19: Monte Carlo $D^0 \to K\pi\pi^0$ Events in the Dalitz Corners for Signal, Midwing and Highwing Regions

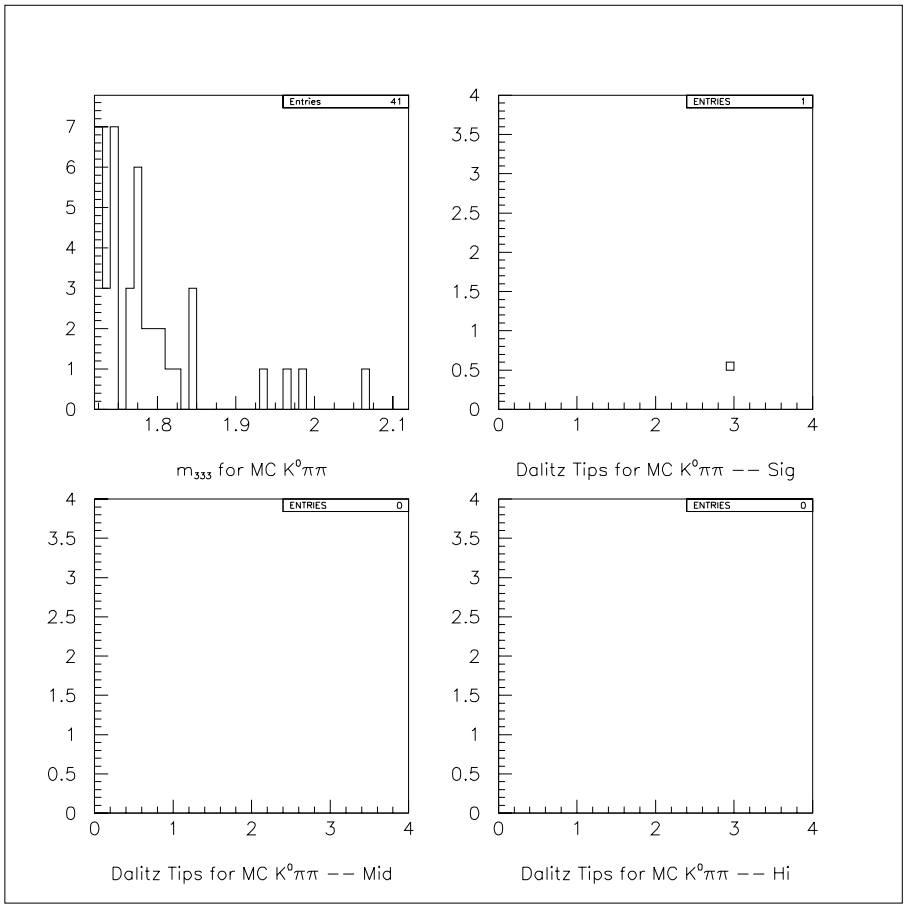

Fig. 6.20: Monte Carlo $D^0 \to K^0\pi\pi$ Events in the Dalitz Corners for Signal, Midwing and Highwing Regions

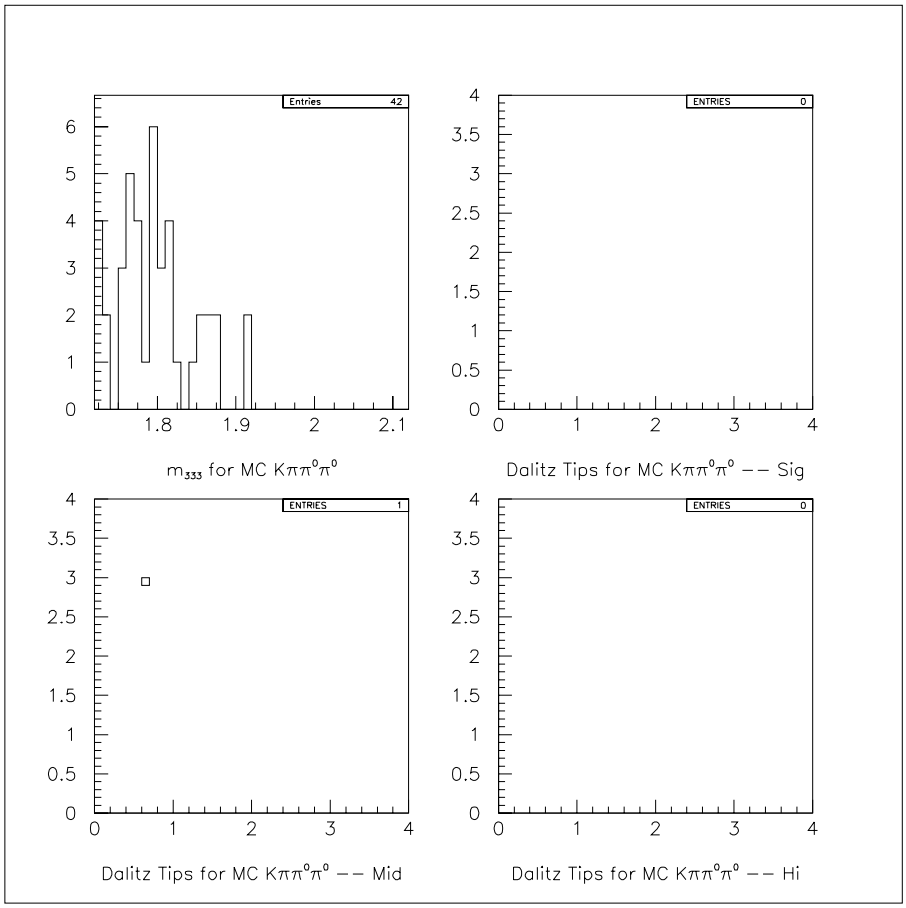

Fig. 6.21: Monte Carlo $D^0 \to K\pi\pi^0\pi^0$ Events in the Dalitz Corners for Signal, Midwing and Highwing Regions

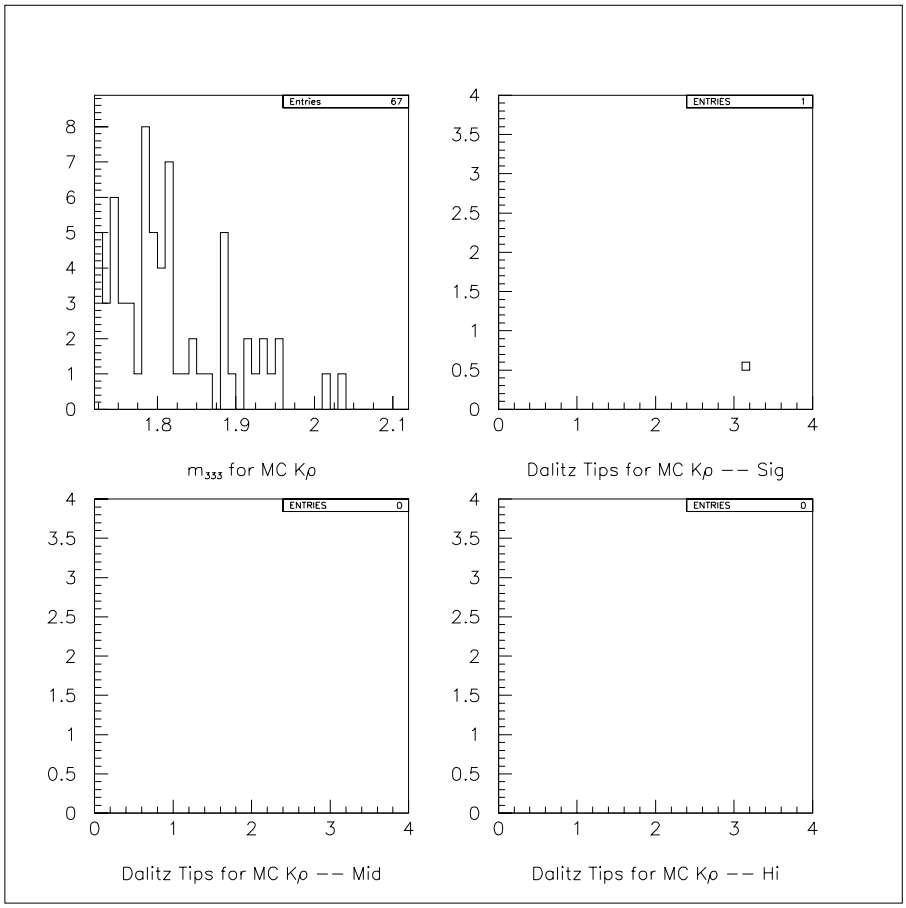

Fig. 6.22: Monte Carlo $D^0 \to K\rho$ Events in the Dalitz Corners for Signal, Midwing and Highwing Regions

An E791 analysis [36] studied the production of the D^0 by examining the number of $D^0 \to K\pi$ data events seen. The study found that there were 477,089 $D^* \to D^0\pi$, with $D^0 \to K\pi$ produced in E791, for all x_F. This analysis will use that number to calculate the number of background events expected in data from the number of Monte Carlo events seen in this study. An example of how this was done for all D^0 background modes will be presented for the case of the $D^* \to D^0\pi, D^0 \to K\rho$ background mode. The method first calculates the ratio of the number of $D^0 \to K\rho$ produced to the number of $D^0 \to K\pi$ measured by calculating the ratio of their D^0 branching ratios (BR):

$$\frac{BR(D^0 \to K\rho)}{BR(D^0 \to K\pi)} = 2.8$$

From Table 6.3 or from the Dalitz corner plot for the Signal region in Figure 6.22 it can be seen that only one event survived. Next, knowing that there were 375,000 $D^* \to D^0\pi, D^0 \to K\rho$ events initially produced and that there were 477,089 $D^* \to D^0\pi, D^0 \to K\pi$ produced in E791, the number of events expected in the E791 Dalitz corner plot for the Data Signal region can be calculated:

$$\frac{1\ D^0 \to K\rho\ surviving}{375000\ D^0 \to K\rho\ thrown} \cdot 2.8 \cdot 477089 = 3.6$$

expected events

Table 6.4 presents the results of using this method to calculate the number of expected events for each D^0 background mode studied.

Releasing the requirement that one reconstructed track be matched to one of the thrown Monte Carlo tracks only affects one D^0 background mode. Relaxing the match criteria allows eight more $D^0 \to K\pi$, no D^* events to show up in the Dalitz corner for the Signal region.

One additional background that contributes to the Dalitz corner is the flat background modeling the events with mis-reconstructed secondary vertices. To analyze the number of these events that might show up in the Dalitz corner, 250,000 non-resonant $D_s \to \pi\pi\pi$ Monte Carlo events were put through the filtering and stripping stages as data. The number of events in the ± 50 MeV/c^2 Signal region around the 1.970 GeV/c^2 D_s mass pasing these stages and the final analysis cuts was seen to be 13,504. Of those

Tab. 6.4: Calculated Number of Expected Background Events in Data Dalitz Corner Plot

D^0 Decay Mode	BR(mode) / $BR(D^0 \to K\pi)$	Produced in E791	Expected Event Number Midwing	Signal	Highwing
$Ke\nu$	0.95	453,000	0	0	0
$K\mu\nu$	0.84	401,000	0	0	0
$\pi\pi$	3.9×10^{-2}	186,000	0	0	0
$\pi\pi\pi^0$	0.41	196,000	0	0	0
$K\pi\pi^0$	0.18	85,800	0	0	0
$K^0\pi\pi$	1.4	668,000	0	1.8	0
$K\pi\pi^0\pi^0$	3.9	1,800,000	4.8	0	0
$K\rho$	2.8	1,300,000	3.6	3.6	3.6
$K\pi$	1.0	453,000	24	41	6
$K\rho$ (no D^*)	2.8	1,300,000	3.6	0	0
$K\pi$ (no D^*)	1.0	453,000	47	94	22
Totals	-	-	83	140.4	31.6

13,504 events, 1384 are in the Dalitz corner plot. Observing that there are 1046 signal events over 1515 background events in Figure 1.2 and that in this thesis the flat background contribution is fit to be about 75.6% of the total, the number of expected flat background events in the Dalitz corners yields

$$\frac{1384}{13504} \cdot 1515 \cdot 0.756 \approx 115 \; expected \; events$$

Combining this value with the total of 140 events in the Signal region from Table 6.4, the resulting 265 events well match the number of data events seen in the Dalitz corner plot of the Signal region (280 events). Factoring in the contributions from $f_2(1270)$ and the $\rho(1450)$, signal amplitudes which also marginally populate the Dalitz Corner region, and the number even more closely approaches the 280 events seen. This study, which was motivated by the appearance of structure in the Highwing region of Figure 6.1, would seem to indicate that the D^0 background completely describes the structure seen in the Dalitz corners of the Signal region.

6.5.4 Other Sources of Charm Background

Since the D_s is the heaviest ground state charm meson, the sources of possible charm background for events in the D_s region are not numerous. While there are a number of charm decays that contribute to the mass spectrum from 1.72 - 2.12 GeV/c^2, few actually contribute to D_s region. It is useful to first eliminate the possible sources that might peak in the D_s mass region. First among these might be any other D_s decays that could mimic the $D_s^+ \to \pi^+\pi^-\pi^+$ topology. Since these events would have the same parent particle mass, they would of course show up in the same mass region. That they have a similar topology is necessary so that they can pass the analysis cuts. The decay $D_s^+ \to \eta^{'}\pi^+$, with the subsequent decay $\eta' \to \rho^0\gamma$, is one such candidate.

One could expect the ρ^0's from this background to be represented by a Breit-Wigner, like the ρ^0's coming from the $D \to \pi^+\pi^-\pi^+$ decay. There is, however, an interesting effect due to the particular kinematics of the $\eta' \to \rho^0\gamma$ decay.

The $D_s^+ \to \eta'\pi^+$ produces a real $\pi\pi\pi$ final state whose invariant mass, because of the undetected γ, is distributed from 1.4 to 2.05 GeV/c^2, as shown in figure 6.23.

In Figure 6.24a we see a scatter plot of $m^2_{\pi_1\pi_2}$, $m^2_{\pi_2\pi_3}$ for MC $D_s^+ \to \eta'\pi^+$ events that passed all analysis cuts, with $M_{\pi\pi\pi}$ between 1.4 and 2.05 GeV/c^2. In Figure 6.24b we see the $m^2_{\pi_1\pi_2}$ projection, which can be fit to a Breit-Wigner function. However, Figures 6.24c and d show what happens when the three-pion mass is restricted to be within the D^+ and D_s windows. It was discovered that the $D_s^+ \to \eta'\pi^+$ events appearing in the D_s mass region are actually those having a very low energy γ. In this case, the ρ^0 mass will be very close to the η' mass. In other words, looking only at events near the D_s mass is equivalent to picking the ρ^0 from a thin slice at the upper tail of the original ρ^0 Breit$-$Wigner.

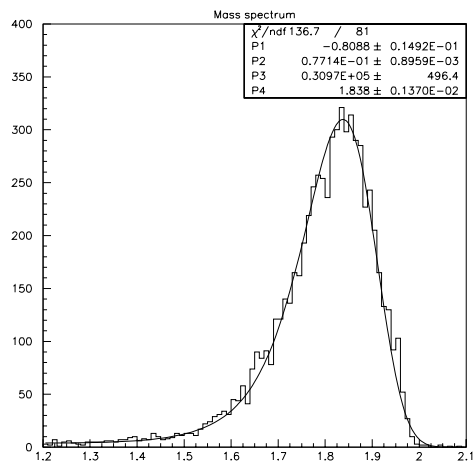

Fig. 6.23: Distribution of the $D_s^+ \to \eta'\pi^+$ MC events in the $\pi^+\pi^-\pi^+$ invariant mass spectrum.

As seen in Figure 6.24d, the result is a much narrower $\pi^+\pi^-$ distribution. This effect is less dramatic when we look at the events within the D^+ mass window, but, still, it results in a narrower $\pi^+\pi^-$ distribution compared to the original Breit-Wigner, and is best represented by a Gaussian form.

All other known D_s decay products listed in the PDG either have long-lived intermediate resonances (over 39% of the D_s decays contain a K^0) so they would not pass the three-prong vertex cut, would require three-prong vertices with non-detected neutrals (many of the copious modes contain a π^0) so they would not pass the PTB cut, or have a kaon as one of the charged

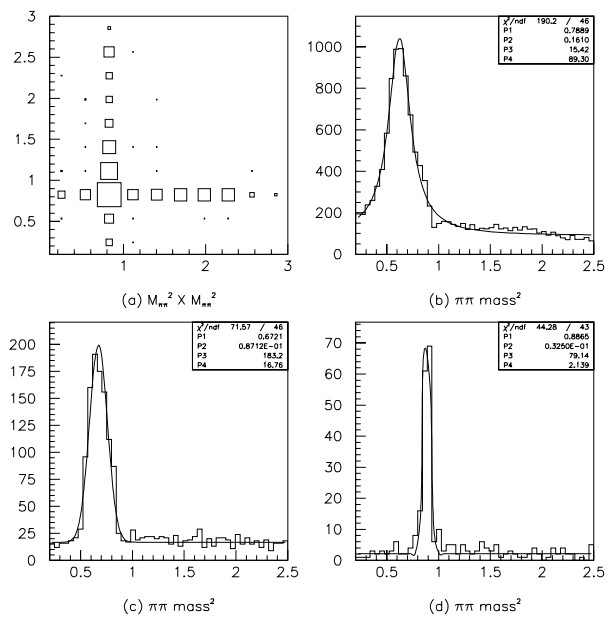

Fig. 6.24: $D_s \to \eta'\pi^+$, $\eta' \to \rho^0\gamma$, $\rho^0 \to \pi^+\pi^-$ MC events.a) all events with 1.4< $M_{\pi\pi\pi}$ <2.05 GeV/c^2; b) $m^2_{\pi_1\pi_2}$ projection of all events from a); c) $m^2_{\pi_1\pi_2}$ projection of events within D^+ mass window; d) $m^2_{\pi_1\pi_2}$ projection of events within D_s mass window.

tracks (over 33% of the D_s decays contain a charged kaon) which would reflect out of the D_s mass region when the three pion mass hypothesis is calculated.

Since there are no other known mesons or baryons with masses at or above the D_s mass, the next thing to understand or eliminate would be particles that have mass peaks close to that of the D_s, so that the tails of their mass distributions might extend into the D_s mass region. Only the D^+ meson is close to the D_s in mass. The earlier discussion of the D^+ width already demonstrated that there are no D^+ signal events that need to be considered as background events for this analysis.

As discussed in a previous subsection, contributions to D_s background can come from something known as reflection. Missing or misidentifying one (or several) of the decay products of a charm particle that is heavier or lighter than the D_s can cause the particle's mass distribution to be shifted from its true value. It is obvious that missing a particle (either a neutral that was not

detected, or a charged particle that did not get included into the secondary vertex) is simply a more extreme example of inserting a lighter particle for a heavier one, and so has the same effect—the mass is shifted downward from its true value.

Since the pion is the lightest meson, reflections into the D_s mass region are minimized from below. There simply are no possible lighter hadronic decay products that can cause their decay to be "reflected up" through having a decay particle be misidentified as a "heavier" pion. Additionally, since the beauty mesons and the charm baryons are so much heavier than the D_s, reflections are also minimized from above.

A study to examine the charm baryon decays with high enough branching fractions to possibly show up in the data final mass hypothesis spectrum resulted in the $\Lambda_c \to pK\pi$ as the only candidate. The E791 Monte Carlo (MC) was used to produce the charm baryon events used in this background study. For the study, appropriate MC events were generated, and then put through the exact same analysis steps as the data sample. After cuts, the events that remained were examined to see if their distributions extended into the D_s mass region. Note that in addition to the mass difference, the Λ_c decay contains a baryon as well as only one pion in its decay products. As demonstrated in Figure 6.25, plotting the $pK\pi$ as $\pi\pi\pi$ after analysis cuts shows that because of the large proton-pion and kaon-pion mass differences there is no reflection of the Λ_c into the D_s mass region.

Other charm baryons were shown to either have lifetime differences that would prevent them from passing the analysis cuts or even poorer topologies to attempt to reflect. The low production cross section at E791 energies also removes bottom mesons (B_c,B_s,B_d,B_u) as possible contributors to background in the D_s mass region.

6.5.5 Sum of Contributions of Background Sources

A careful study of the $D_s^+ \to \pi^+\pi^-\pi^+$ background has identified only three likely sources. Since this analysis floats the percent contribution of each of the three backgrounds in the maximum likelihood fit, no additional rigorous counting analysis will be performed, other than what was done to determine if the D^0 plus π background could be completely accounted for from its various sources. The number of each background type obtained in the fit and the effect of varying those numbers will be discussed in the error analysis chapter.

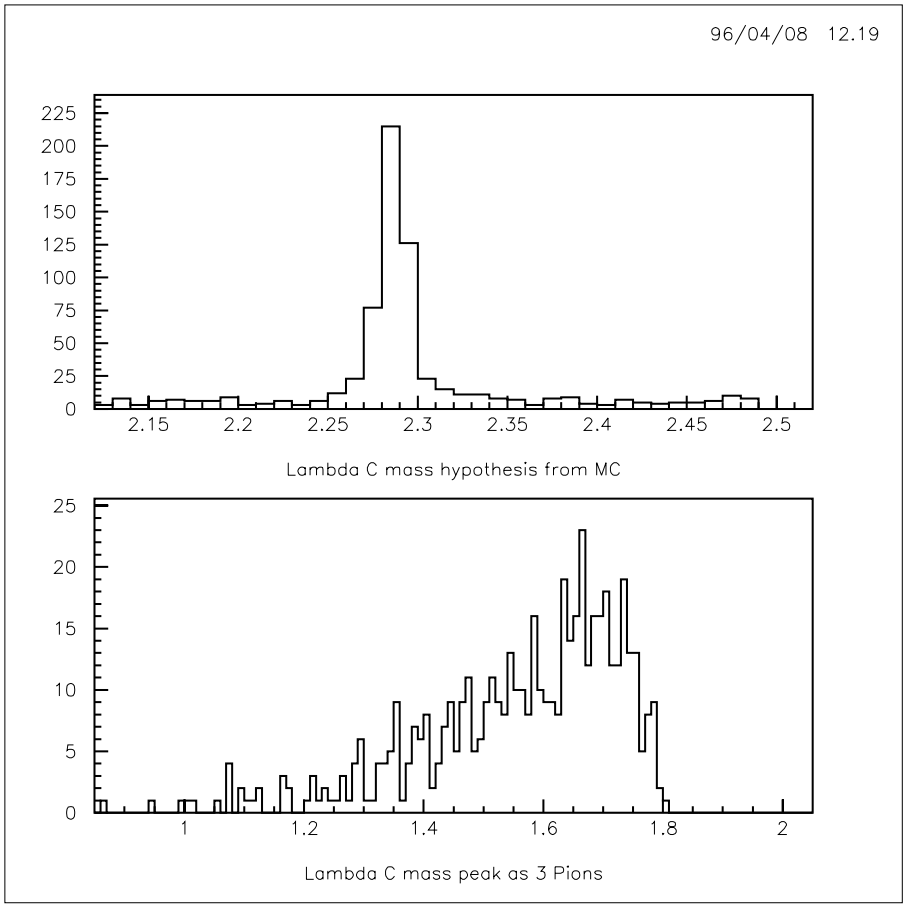

Fig. 6.25: Plotting $\Lambda_c \to pK\pi$ as $\pi\pi\pi$ and Looking in the D_s Mass Window

7. THE MAXIMUM LIKELIHOOD FITTING TECHNIQUE

7.1 Introduction and Overview

This chapter describes the methodology used to study the substructure of the decay $D_s^+ \to \pi^+\pi^-\pi^+$. A maximum likelihood technique which allowed coherent interference among different signal amplitudes was used to estimate the contributions from the different modes included in the fit. The likelihood function is defined in terms of a probability density function (PDF) for the data sample to have the given substructure. It is maximized with respect to the parameters (amplitudes, phases, etc.) which define the substructure.

The likelihood function $\mathcal{L}$ has the following form:

$$\mathcal{L} = \prod_{i=1}^{n} \mathcal{P}_i \tag{7.1}$$

where n is the total number of events in the data sample. $\mathcal{P}_i$ is the probability density function for the ith event. It can be written in terms of a signal term $\mathcal{P}_{iS}$ and a background term $\mathcal{P}_{iB}$ for each event i

$$\mathcal{P}_i = \frac{S \cdot \mathcal{P}_{iS} + B \cdot \mathcal{P}_{iB}}{S + B} \tag{7.2}$$

The extended maximum likelihood [37] method uses the number of events found, S+B, as one more determination to be made by the fit. The number is assumed to obey Poisson statistics. This makes the likelihood function

$$\mathcal{L} = \frac{e^{\nu}\nu^n}{n!} \prod_{i=1}^{n} \mathcal{P}_i \tag{7.3}$$

where n is the total number of events in the data sample and ν is the number of events estimated by the fit: ν = S+B.

Tab. 7.1: Properties of Possible Intermediate Resonances

Resonance	Mass (GeV/c^2)	Width (GeV/c^2)	Source
$f_0(980)\pi^+$	0.976	0.042	from fit
$\rho^0(770)\pi^+$	0.769	0.150	PDG
$f_2(1270)\pi^+$	1.275	0.185	PDG
$f_0(1370)\pi^+$	1.438	0.165	from fit
$\rho^0(1450)\pi^+$	1.465	0.351	PDG

7.2 Resonant Mass Distributions

The decay $D_s^+ \to \pi^+\pi^-\pi^+$ can occur through a rather large number of intermediate decay modes—a non-resonant $\pi\pi\pi$ mode and combinations of the resonances in Table 7.1 with an additional π. The relevant properties of the possible intermediate resonances are also provided in the table.

Figure 7.1 shows the Dalitz distribution (i.e., square of the $\pi\pi$ invariant mass distributions) of possible resonant components using Monte Carlo events that passed analysis cuts.

Comparing these distributions with the data Dalitz plot repeated in Figure 7.2, there are clear indications for $f_0(980)$, $f_0(1370)$ and $f_2(1270)$ in the D_s mass region (i.e., there are scalar and vector resonances that must be modeled).

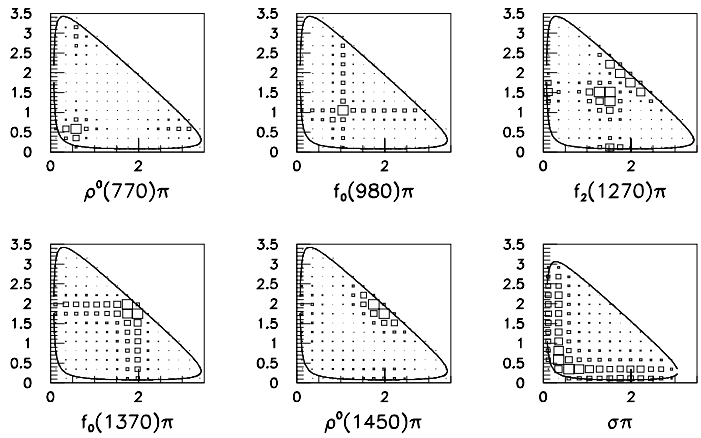

Fig. 7.1: Possible Resonance Contributions

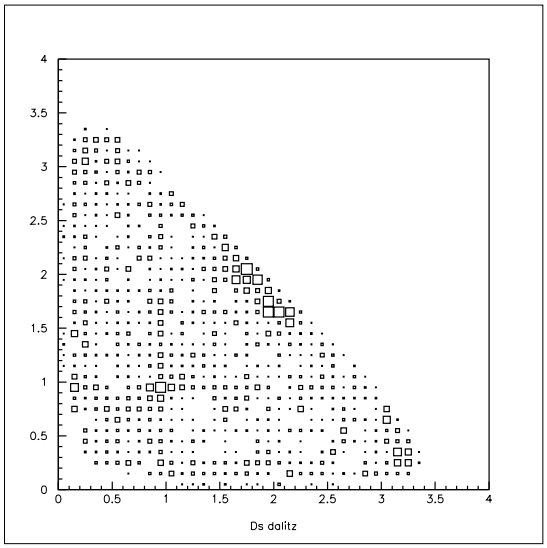

Fig. 7.2: Analysis Dalitz Plot

7.3 Maximum Likelihood Function

The signal and background probability density functions are developed in the subsections that follow.

7.3.1 Signal Probability Distribution Function.

The transition probability, $\mathcal{P}_S$, of the transition $D_s \to X$ occurring with final state at the point ϕ in the phase space is

$$\mathcal{P}_S(\phi) = | < D_s|T|X > |^2 d\phi. \tag{7.4}$$

The expression $< D_s|T|X >$ is used to represent the transition matrix for the $D_s \to X$ decay, and $d\phi$ is used for the phase space density. The point ϕ simply represents an $(m^2_{\pi_1^+\pi_2^-}, m^2_{\pi_3^+\pi_2^-})$ point on the Dalitz plot.

If this transition T can occur via t intermediate modes T_i, the transition matrix T can be written as a sum of transition matricies (individually normalized), so that

$$T = a_1T_1 + a_2T_2 + ... + a_tT_t \tag{7.5}$$

Here, the a_i are the complex amplitudes proportional to the contribution of the transition matrix T for the ith decay mode. If each a_i is expressed in terms of a magnitude A_i and phase δ_i, the signal probability density function becomes:

$$\mathcal{P}_S(\phi) = | < D_s|A_1e^{i\delta_1}T_1 + A_2e^{i\delta_2}T_2 + ... + A_te^{i\delta_t}T_t|X > |^2 d\phi \tag{7.6}$$

Although the exact form of the matrix elements are not known, some of their features can be deduced from known conservation laws and phenomenology.

Our still-general S_i is defined as the phenomenologically deduced transition matrix of the decay $D_s \to X$:

$$< D_s|T_i|X >= \frac{S_i}{\sqrt{N_i}}. \tag{7.7}$$

The normalization of S_i is defined by

$$N_i = \int_{phase\ space} S_iS_i^* d\phi. \tag{7.8}$$

Using this form, the probability density function can be written:

$$\mathcal{P}_S(\phi) \propto \left| A_1 e_1^{i\delta} \frac{S_1}{\sqrt{N_1}} + A_2 e^{i\delta_2} \frac{S_2}{\sqrt{N_2}} + ... + A_t e^{i\delta_t} \frac{S_t}{\sqrt{N_t}} \right|^2 d\phi \tag{7.9}$$

For each event in the phase space there is an efficiency $\epsilon(\phi)$ for that event to be detected, reconstructed and pass the analysis cuts. Additionally, since a detected event must have been originated somewhere in phase space:

$$\sum i = 1^n \int_{phase\ space} S_i S_i^* d\phi = 1 \tag{7.10}$$

Therefore N_S the overall normalization is defined by

$$N_s = \sum_{i=1}^{m} \sum_{j=1}^{m} A_i A_j \mathcal{R}e(e^{i(\delta_i - \delta_j)} E_{ij}) \tag{7.11}$$

where

$$E_{ij} = \int_{phase\ space} \epsilon(\phi) S_i S_j^* d\phi. \tag{7.12}$$

Taking this efficiency and normalization into account, and modulating the function with the normalized three pion D_s gaussian $G(M_{3\pi})$, the final signal probability density function is

$$\mathcal{P}_S = \frac{1}{N_S} \frac{G(M_{3\pi})}{N_G} \epsilon(\phi) \sum_{i=1}^{m} \sum_{j=1}^{m} A_i A_j \mathcal{R}e \left[e^{i(\delta_i - \delta_j)} \frac{S_i S_j^*}{\sqrt{N_i N_j}} \right] d\phi \tag{7.13}$$

Equation 7.12 gives the probability for a $D_s^+ \to \pi^+\pi^-\pi^+$ event to decay at ϕ, given the particular resonant substructure model we choose to use. The form for the individual signal functions S_i used in this analysis are developed in Section 7.4.

7.3.2 Background Probability Distribution

Backgrounds may come to the event sample as a random combinatoric background or as a misidentified charm background. Background probability distribution functions need to account for all these contributions.

Since this model assumes there are no resonant background components, the background amplitudes are not coherent. The background probability density function can therefore be expressed as

$$\mathcal{P}_B = \frac{1}{N_b} \sum_{i=1}^{k} b_i \cdot B_i d\phi \tag{7.14}$$

where k is the number of possible backgrounds, b_i are numbers proportional to the fraction of each background and B_i are the fluctuations which describe the backgrounds. They are normalized such that

$$\int_{phase\ space} B_i d\phi = 1 \tag{7.15}$$

and N_b is the overall normalization of the background

$$N_b = \int_{phase\ space} \mathcal{P}_B d\phi \tag{7.16}$$

Similar to the signal probability density function, the background probability density function is the product of the probability of observing a background event and the probability of the background event to have a particular background structure. The background distribution in $\pi\pi\pi$ mass was well described by an exponential function in Figure 1.2, and is included in the background PDF as the normalized exponential function $E(M_{3\pi})$.

$$\mathcal{P}_B = \frac{1}{N_b} \frac{E(M_{3\pi})}{N_E} \sum_{i=1}^{k} b_i \cdot B_i d\phi \tag{7.17}$$

Note that since the background parameterization of $E(M_{3\pi})$ is made directly from data, there is no need to include an efficiency correction term in the above equation as was done in Equation 7.12 for the signal PDF.

7.3.3 Form of the Likelihood Function

The maximum likelihood method will insert the P_S and P_B developed in the previous two subsections into the probability density function used to describe the n data events in the final sample:

$$\mathcal{L} = \frac{e^{\nu}\nu^{n}}{n!}\prod_{i=1}^{n}\left[\frac{S\cdot\mathcal{P}_{iS}+B\cdot\mathcal{P}_{iB}}{S+B}\right] \tag{7.18}$$

It is more convenient to use $\ln\mathcal{L}$ instead of $\mathcal{L}$ in the fit because multiplication over events then becomes a sum over events. Eliminating multiplication of terms reduces the impact of very large or very small numerical values that enter into the calculation. Taking the natural logarithm of both sides and expanding,

$$-\ln\mathcal{L} = -\sum_{i=1}^{n}\ln\left[\epsilon(\phi)\cdot\frac{S\cdot\mathcal{P}_{iS}+B\cdot\mathcal{P}_{iB}}{S+B}\right]d\phi - n\ln\nu - \nu + \ln n! \tag{7.19}$$

The function $\epsilon(\phi)$ and $\mathrm{d}\phi$ do not depend on the parameterization of the signal and background probabilities, so they can be factored out before the minimization. Thus, defining $\mathcal{P}_{iS} = \epsilon(\phi)\cdot P_{iS}$ and $\mathcal{P}_{iB} = \epsilon(\phi)\cdot P_{iB}$,

$$-\ln\mathcal{L} = -\sum_{i=1}^{n}\ln\left[\frac{S.P_{iS}+B.P_{iB}}{S+B}\right] - n\ln\nu - \nu + \sum_{i=1}^{n}\ln\epsilon(\phi)d\phi + \ln n! \tag{7.20}$$

The terms $\ln\epsilon(\phi)d\phi$ and $\ln n!$ are constant for a particular data sample and can be ignored in the minimization of $-\ln\mathcal{L}$. In the minimization process, the parameters A_i, δ_i, b_i and any other floating parameters used to model the decay are allowed to float to give the maximum probability using the set of parameters that were used to describe the data according to the physical model of the decay assumed.

7.3.4 Evaluation of Integrals

Phase space integrals can be numerically calculated (up to a constant factor) by summing over a large number of phase space Monte Carlo events generated according to the three body decay. Thus, the normalization condition becomes

$$\sum_{MC\ events\ generated} S_i S_j^* = 1 \tag{7.21}$$

The E_{ij}'s are also calculated using phase space Monte Carlo events.

$$E_{ij} = \sum_{MC\ events\ generated} \epsilon S_i S_j^* \tag{7.22}$$

which is well-approximated by

$$E_{ij} = \sum_{MC\ events\ accepted} S_i S_j^* \tag{7.23}$$

Using this method to calculate the N_i, N_{ij} and N_S, the terms $d\phi$ and $\epsilon(\phi)$ never explicitly need to be evaluated since they are entirely taken into account by Monte Carlo in determining the normalizations for the fit functions.

7.3.5 Normalized Physical Fractions

After finding the set of parameters which maximize the probability distribution function for a given data sample, the parameters A_i can be uncertain up to a common scale factor. Normalizing the fractions allows the actual physical values to be obtained.

Since the sum of the signal probability distribution function over all available statuses should be one, it implies that, before acceptance effects,

$$\int \mathcal{P}_S d\phi = 1 \tag{7.24}$$

where

$$\mathcal{P}_S = \frac{1}{N_P} \left| \sum_{i=1}^{m} A_i e^{i\delta_i} \frac{S_i}{\sqrt{N_i}} \right|^2 d\phi. \tag{7.25}$$

This requires

$$N_P = \sum_{i=1}^{m} \sum_{j=1}^{m} A_i A_j \mathcal{R}e(e^{i(\delta_i - \delta_j)} N_{ij}) \tag{7.26}$$

where, from before,

$$N_{ij} = \int_{phase\ space} S_i S_j^* d\phi \tag{7.27}$$

Since in evaluating integrals the phase space was assumed to be represented by the Monte Carlo sample used to calculate the integrals, numerically,

$$N_P = \sum_{MC\ events\ generated} \frac{S_i S_j^*}{\sqrt{N_i N_j}}. \tag{7.28}$$

The physical fractions f_i are then defined as

$$f_i = \frac{A_i^2}{N_p} \tag{7.29}$$

The error on N_P is given by

$$(\text{Error N}_\text{P})^2 = \sum_{i,j} \frac{\partial N_P}{\partial x_i} \frac{\partial N_P}{\partial x_j} Var(x_i, x_j) \tag{7.30}$$

where x_i includes A_i and δ_i and $Var(x_i, x_j)$ is the error matrix of x_i. Evaluating derivatives,

$$\frac{\partial N_p}{\partial A_k} = \sum_i A_i \mathcal{R}e(e^{i(\delta_i - \delta_j)} N_{ij}) \tag{7.31}$$

and

$$\frac{\partial N_p}{\partial \delta_k} = -2 \sum_{j=k} A_k A_j \mathcal{I}m(e^{i(\delta_k - \delta_j)} N_{ki}) \tag{7.32}$$

These formulae allow the physical fractions and their errors to be extracted from the error matrix and the values of A_i and δ_i returned by the maximum likelihood fit.

7.4 Signal Matrix Elements

The signal elements, S_i, are usually written in terms of Breit-Wigner functions with momentum-dependent partial widths, form factors, and angular distribution functions [38, 39]. Figure 7.3 pictorially represents the Zemach formalism outlined in the following section.

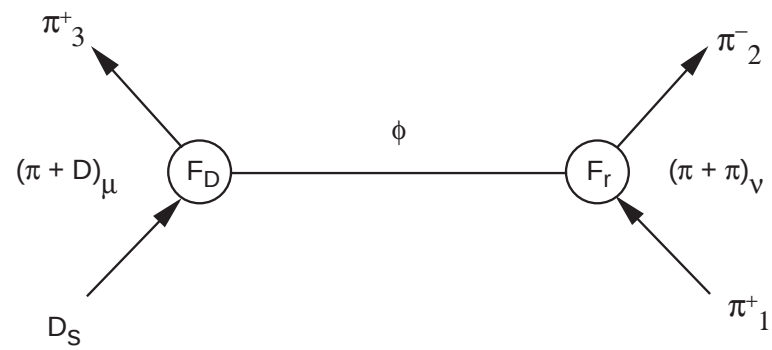

Fig. 7.3: Feynman Diagram for the process $D \to (r)\pi_3 \to \pi_1\pi_2\pi_3$

7.4.1 Breit Wigner Functions

The relativistic Breit Wigner function of the form

$$\frac{1}{m^2 - m_0^2 + i m_0, (m)} \tag{7.33}$$

is used for each resonant state. In the above equation, m_0 is the on-shell mass of the resonance and m is the invariant mass of the two final state particles from the resonance (i.e., the $\pi^+\pi^-$ that comes from the resonance). $, (m)$ is the partial width of the resonance which is assumed to have the following momentum dependence:

$$, (m) = , _0 \frac{m_0}{m} \left(\frac{p^*}{p_0^*}\right)^{2J+1} \frac{F_J^2(p^*)}{F_J^2(p_0^*)} \tag{7.34}$$

Here, p is the momentum of the decay particles in the resonance rest frame and J is the spin of the resonance particle.

7.4.2 Form Factors

The Blatt and Weisskoff form factors (F_J) are defined [40] for two body decays of a resonance with spin J:

$$F_0 = 1 \tag{7.35}$$

for $J = 0$,

$$F_1 = \frac{1}{\sqrt{1 + R^2 p^2}} \tag{7.36}$$

for $J = 1$ and

$$F_2 = \frac{1}{\sqrt{9 + 3R^2 p^2 + (R^2 p^2)^2}} \tag{7.37}$$

for J=2. The appropriate form factor is used for each D meson and intermediate resonance decay vertex. In the above equations, R represents the meson or resonance radius which has typical values of 5 GeV^{-1} for D_s and 1.5 GeV^{-1} for our intermediate resonances.

7.4.3 Angular Distributions

Each decay has a characteristic angular distribution depending on the spin and angular momentum of the decay particles. For example, a non-resonant decay of a pseudo scalar particle into pseudo scalers is isotropic in space—its angular distribution is uniform.

The Zemach formalism uses tensor products of the effective hadronic matrix elements to model the angular portion of the decay of the resonance. The currents are constructed from the 3-momenta of the particles, and in the rest frame of the resonance, take the form

$$c_J |\vec{p}_{\pi_2}|^J |\vec{p}_{\pi_1}|^J P_J(cos\theta^r_{12}) \tag{7.38}$$

Here, θ^r_{12} is the angle between π_1 and π_2 in the resonance rest frame, and P_J is a Legendre polynomial. The value of the normalization constant c_J is by convention set to $(-2)^J$.

Table 7.2 summarizes the generalized amplitudes for the decay $D_s \rightarrow r\pi_3 \rightarrow \pi_1\pi_2\pi_3$.

Tab. 7.2: Zemach Amplitudes for the decay $D \to r\pi_3 \to \pi_1\pi_2\pi_3$

$J^P(r)$	Example	Zemach Amplitude $\mathcal{M}(\pi_1\pi_2\pi_3\|\mathrm{r})$
Nonresonant	-	1
0^+	$f_0(980)$	$F_D F_r \times$ BW
1^-	$\rho^0(770)$	$F_D F_r \times -2\|\vec{p}_{\pi_2}\|\|\vec{p}_{\pi_1}\|cos\theta^r_{12} \times$ BW
2^+	$f_2(1270)$	$F_D F_r \times (-2\|\vec{p}_{\pi_2}\|\|\vec{p}_{\pi_1}\|)^2 \frac{1}{2}(3cos^2\theta^r_{12} - 1) \times$ BW

7.4.4 Symmetrization of the Signal Amplitudes

A final step in the calculation of each resonance's signal amplitude (S_i) was to Bose-symmetrize the contributions from the two $\pi^+\pi^-$ combinations. The decay $D_s^+ \to \pi_1^+\pi_2^-\pi_3^+$ involves two identical bosons in the final state, requiring the amplitude to be Bose-symmetrized under the exchange of the two pions

$$S_i = \frac{\mathcal{M}_i(\pi_1^+\pi_2^-\pi_3^+|r) + \mathcal{M}_i(\pi_3^+\pi_2^-\pi_1^+|r)}{2}$$

where the notation $\mathcal{M}_i$ denotes the appropriate Zemach Amplitude (as developed in the previous subsections) for each signal resonance i.

7.5 Background Amplitudes

The background amplitudes are simple functions which are derived from data and Monte Carlo distributions. The specific derivation of the background and signal amplitudes is described in the next chapter.

8. THE MAXIMUM LIKELIHOOD FIT IMPLEMENTATION

8.1 Introduction and Overview

The previous chapter provided an outline of the maximum likelihood fitting technique and described the general form of the amplitudes and probability density functions. This chapter describes the actual implementation of the technique, presents specific forms of the amplitudes and density functions and presents the fit results.

8.2 Signal PDF

As developed in the previous chapter, the signal amplitudes for each resonance included in the fit were written as a product of a relativistic Breit Wigner propagator and a function depending on the spin of the resonance. These amplitudes were expressed in terms of three variables which completely describe the kinematics of each event—the $\pi_1^+\pi_2^-\pi_3^+$ invariant mass $M_{3\pi}$, and the Lorentz invariants $s_{12} \equiv m^2_{\pi_1^+\pi_2^-}$ and $s_{23} \equiv m^2_{\pi_3^+\pi_2^-}$ (a reminder that this thesis always labels the odd charged pion as particle 2). Table 7.1 lists the intermediate states that were included in the fit for the D_s decay. The states were chosen because they comprise the well established $\pi\pi$ resonances that can contribute to the $D_s^+ \to \pi^+\pi^-\pi^+$ decay.

The signal functions are calculated using modular functions to describe their individual components. The Breit Wigner component is described by a function dependent on three variables—the square of the $\pi\pi$ invariant mass for the event, and the mass and width of the Breit Wigner for the particular signal amplitude. This allowed a single function to be used for each resonance, with individual resonances simply passing appropriate arguments to the function.

The form of the Breit Wigner function used in the analysis code is provided here:

$$
\begin{aligned}
&real*8\ function\ bw(x,y,z)\\
&real*8\ x,\ y,\ z\\
&complex*16\ im,re\\
&re=(y^2-x)/((x-y^2)^2+(x\cdot z)^2)\\
&im=(y\cdot z)/((x-y^2)^2+(y\cdot z)^2)\\
&bw=(re\cdot(1.0,0.0)-im\cdot(0.0,1.0))\\
&return\\
&end
\end{aligned}
$$

The values of the mass (m_0) and width ($,_0$) of the resonance are passed to the function call, along with the value of the Lorentz invariant for the particular $\pi^+\pi^-$ combination in the event.

The angular component of each resonance is calculated using the appropriate formulae as derived in Section 7.4.3. The formulae are also further compacted through the use of a kinematical function that commonly describes all pion lab momenta in terms of the event Lorentz invariants [41]. The form of this function is

$$\lambda(x,y,z)\equiv(x-y-z)^2-4.0\cdot y\cdot z.$$

The final form of the six signal amplitudes is presented here:

For the non-resonant amplitude

$$sig(1)=1.0$$

For the $D_s\rightarrow\rho^0(770)\pi$ amplitude

$$
\begin{aligned}
&m_0=0.769\\
&,_0=0.150\\
&p3=0.5\cdot(\sqrt{\lambda(s,s12,m3sq)}/s12)\\
&p2=0.5\cdot(\sqrt{\lambda(s12,m1sq,m2sq)}/s12)\\
&f21=-2\cdot p3\cdot p2\cdot cos\theta_{32}\\
&sig21=bw(s12,m_0,,_0)\cdot f21
\end{aligned}
$$

$$p1 = 0.5 \cdot (\sqrt{\lambda(s, s23, m1sq)}/s23)$$
$$p2 = 0.5 \cdot (\sqrt{\lambda(s23, m2sq, m3sq)}/s23)$$
$$f23 = -2 \cdot p1 \cdot p2 \cdot cos\theta_{12}$$
$$sig23 = bw(s23, m_0, , _0) \cdot f23$$

$$sig(2) = sig21 + sig23$$

For the $D_s \to f_0(980)\pi$ amplitude

$$m_0 = 0.979$$
$$, _0 = 0.044$$
$$f21 = 1.0$$
$$sig21 = bw(s12, m_0, , _0) \cdot f21$$
$$f23 = 1.0$$
$$sig23 = bw(s23, m_0, , _0) \cdot f23$$

$$sig(3) = sig21 + sig23$$

For the $D_s \to f_2(1270)\pi$ amplitude

$$m_0 = 1.275$$
$$, _0 = 0.185$$
$$p3 = 0.5 \cdot (\sqrt{\lambda(s, s12, m3sq)}/s12)$$
$$p2 = 0.5 \cdot (\sqrt{\lambda(s12, m1sq, m2sq)}/s12)$$
$$f21 = 2 \cdot (p3 \cdot p2)^2 \cdot (3. \cdot cos^2\theta_{32} - 1.)$$
$$sig21 = bw(s12, m_0, , _0) \cdot f21$$
$$p1 = 0.5 \cdot (\sqrt{\lambda(s, s23, m1sq)}/s23)$$
$$p2 = 0.5 \cdot (\sqrt{\lambda(s23, m2sq, m3sq)}/s23)$$
$$f23 = 2 \cdot (p1 \cdot p2)^2 \cdot (3. \cdot cos^2\theta_{12} - 1.)$$
$$sig23 = bw(s23, m_0, , _0) \cdot f23$$

$$sig(4) = sig21 + sig23$$

For the $D_s \to f_0(1370)\pi$ amplitude

$$m_0 = 1.442$$
$$, _0 = 0.167$$

$$f21 = 1.0$$
$$sig21 = bw(s12, m_0, , _0) \cdot f21$$
$$f23 = 1.0$$
$$sig23 = bw(s23, m_0, , _0) \cdot f23$$

$$sig(5) = sig21 + sig23$$

For the $D_s \to \rho^0(1465)\pi$ amplitude

$$m_0 = 1.465$$
$$, _0 = 0.310$$
$$p3 = 0.5 \cdot (\sqrt{\lambda(s, s12, m3sq)}/s12)$$
$$p2 = 0.5 \cdot (\sqrt{\lambda(s12, m1sq, m2sq)}/s12)$$
$$f21 = -2 \cdot p3 \cdot p2 \cdot cos\theta 32$$
$$sig21 = bw(s12, m_0, , _0) \cdot f21$$
$$p1 = 0.5 \cdot (\sqrt{\lambda(s, s23, m1sq)}/s23)$$
$$p2 = 0.5 \cdot (\sqrt{\lambda(s23, m2sq, m3sq)}/s23)$$
$$f23 = -2 \cdot p1 \cdot p2 \cdot cos\theta 12$$
$$sig23 = bw(s23, m_0, , _0) \cdot f23$$

$$sig(6) = sig21 + sig23$$

Plots of Monte Carlo distributions representing each of these signal amplitudes have been previously presented in Figure 7.1.

8.3 Background PDF

The background probability density function is written as an incoherent sum of real amplitudes. Like the signal amplitudes, these real background amplitudes can also be completely described by the values of s_{12} and s_{23} for a given event. The sources of background were discussed in Section 6.5, resulting in only three contributing sources. The first source is the combinatoric distribution, which is assumed to be uniformly distributed across the Dalitz plot, so the amplitude for this source is a constant. The second source is the reflection of the $D^0 \to K^-\pi^+$ decay with an additional track, which was seen to be concentrated in the corners of the Dalitz plot. The amplitude used for this source is a two-dimensional gaussian in each corner of the Dalitz plot,

whose mass centroids and widths on the s_{12} and s_{23} axes have been measured from E791 Monte Carlo events containing a D^0 plotted as $D_s \to \pi\pi\pi$. The distributions of these events are plotted in Figure 8.1. The plots show the projection of the Dalitz plot onto the each of the $M^2_{s_{12}}$ and $M^2_{s_{23}}$ axes (think of this as rotating the Dalitz plot by 90 degrees and looking at it on its edge). It can be seen that the projections are well fit by gaussians, whose values are then used in the likelihood fit. Each peak is fit in turn, to show the mean and width of the gaussian.

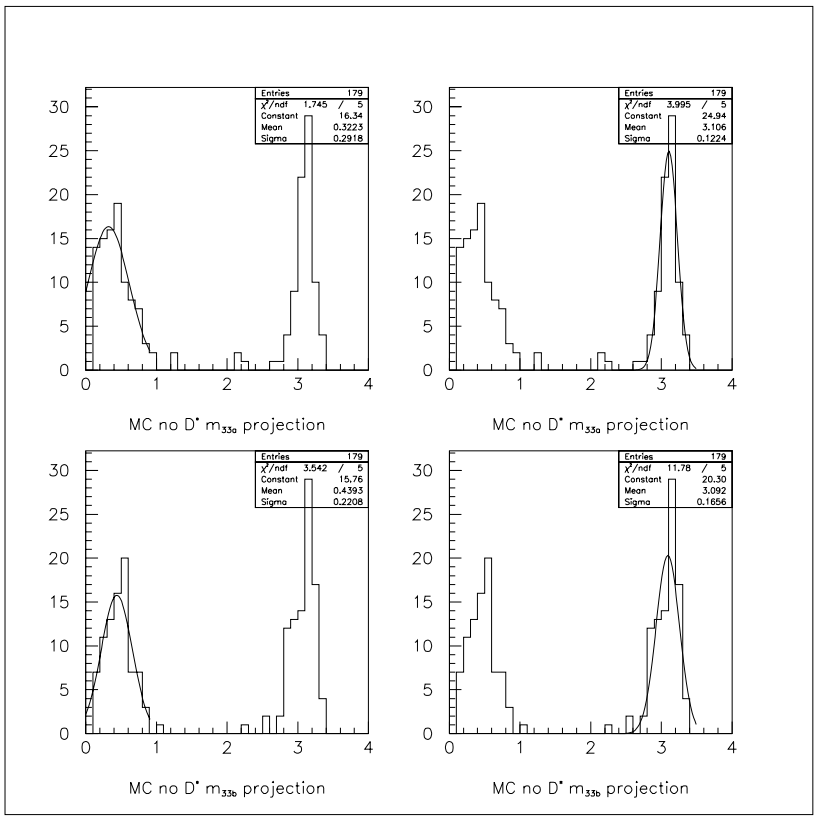

Fig. 8.1: Fit to Projection Gives Centroid and Width of Double Gaussian Representing D^0 plus π Background

The masses and widths in the $D^0 \to K\pi$ projection fits were averaged to provide one x_m, x_w, y_m and y_w for the function that was used to model the double gaussian background in the maximum likelihood fit.

The final background contribution comes from the reflection of the decay $D_s \to \eta'\pi$, with $\eta' \to \rho^0\gamma$. As was outlined in section 6.5.4, Monte Carlo events were used to provide a mass centroid and the gaussian width. The fit values were input into the function that was used model the $D_s \to \eta'\pi$ gaussian in the maximum likelihood fit.

The final form of the three background amplitudes is developed below.

For the flat continuum

$$bkg(1) = 1.0$$

For the symmeterized $D^0 \to K\pi$ double gaussian
(parameters fixed by fit to Monte Carlo)

$$bkg(2) = (gaussd0(s12, s23) + gaussd0(s23, s12))/2$$

where

```
real function gaussd0(x, y)
real * 8 x, y, rnorm, expon, pi
data pi/3.141592653589/
c taken from fits to MC distributions in Figure 8.1
data xm/0.40/
data xw/0.25/
data ym/3.10/
data yw/0.16/

expon = 0.5d0 · (((xm − x)/xw)^2 + ((ym − y)/yw)^2)
rnorm = xw · yw · (2 · pi)
gaussd0 = dexp(−expon)/rnorm
return
end
```

For the gaussian function for $D_s \to \eta'\pi, \eta' \to \rho^0\gamma$
(parameters fixed by fit to Monte Carlo)

$bkg(3) = rhods(s12, s23)$

where

$real\ function\ rhods(x, y)$
$real * 8\ x,\ y,\ rm,\ g,\ gsx,\ gsy$
$rm = 0.89$
$g = 0.044$

$gsx = exp(-(rm - x)^2/(2 \cdot g^2))$
$gsy = exp(-(rm - y)^2/(2 \cdot g^2))$
$rhods = gsx + gsy$
$return$
end

8.4 Efficiency Calculation

The efficiency correction is applied on an event by event basis. It is a weight applied to each event, depending only on the event's Dalitz plot coordinates.

The Monte Carlo was used to test that there were no areas in the Dalitz plot that were enhanced because of the method used to select the $\pi\pi\pi$ events or in the making of the Dalitz plot. A sample of 750,000 Monte Carlo non-resonant $D_s^+ \to \pi^+\pi^-\pi^+$ events were generated for this purpose. Since non-resonant events are generated with the phase space density constant, the distribution of the generated events is flat. That this is true can be seen in Figure 8.2. The events are divided into 20 bins for the range 0–4.0 GeV^2/c^4 along each $M^2_{\pi^+\pi^-}$ axis for the plot.

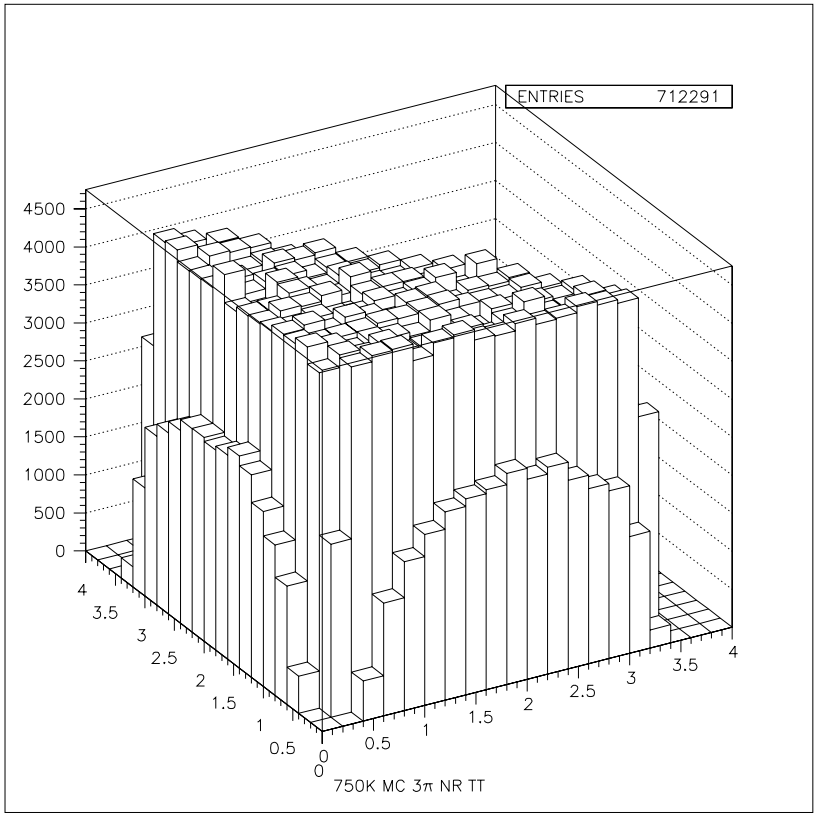

Fig. 8.2: Generated Non-resonant $D_s^+ \to \pi^+\pi^-\pi^+$ Monte Carlo Dalitz Plot

The 750,000 Monte Carlo events were next put through the exact same set of filtering, stripping and substripping selection procedures that were used on the data sample. The final analysis cuts (in Table 6.1) were then applied to the MC sample. Figure 8.3 presents the Dalitz plot made from the two $\pi^+\pi^-$ combinations in each event that survived all selection and analysis cuts. Again, the events are divided into 20 bins for the range 0–4.0 GeV^2/c^4 along each $M^2_{\pi^+\pi^-}$ axis for the plot.

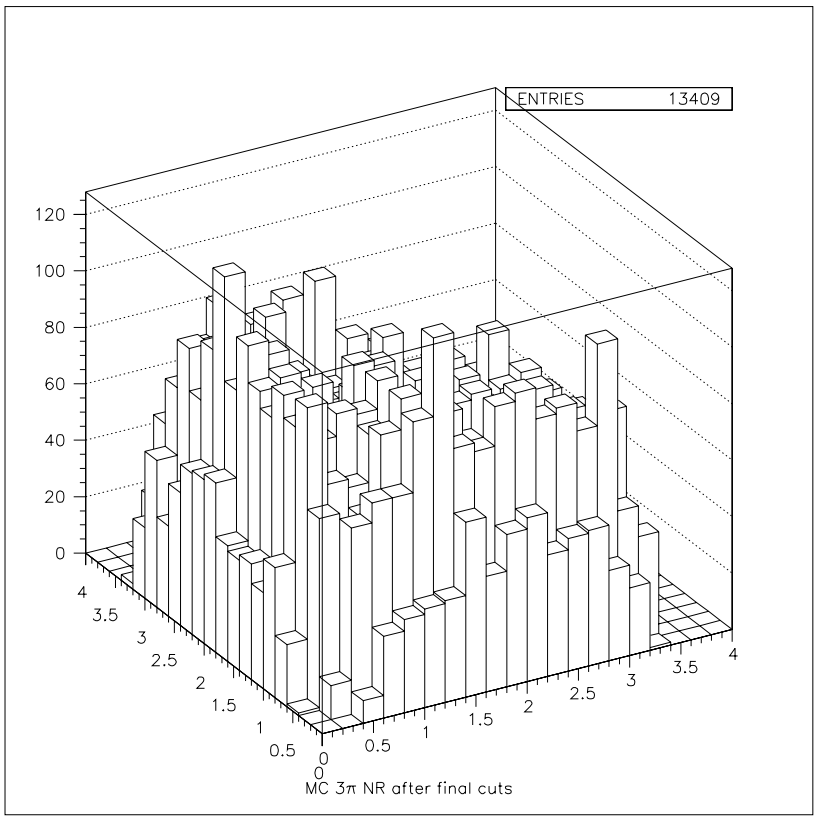

Fig. 8.3: Surviving Non-resonant $D_s^+ \to \pi^+\pi^-\pi^+$ Monte Carlo Dalitz Plot

The efficiency function is derived from the observed Dalitz plot distribution of these surviving events, and is defined by the division of the two histograms in Figures 8.1 and 8.2. The efficiency function obtained is presented in Figure 8.4.

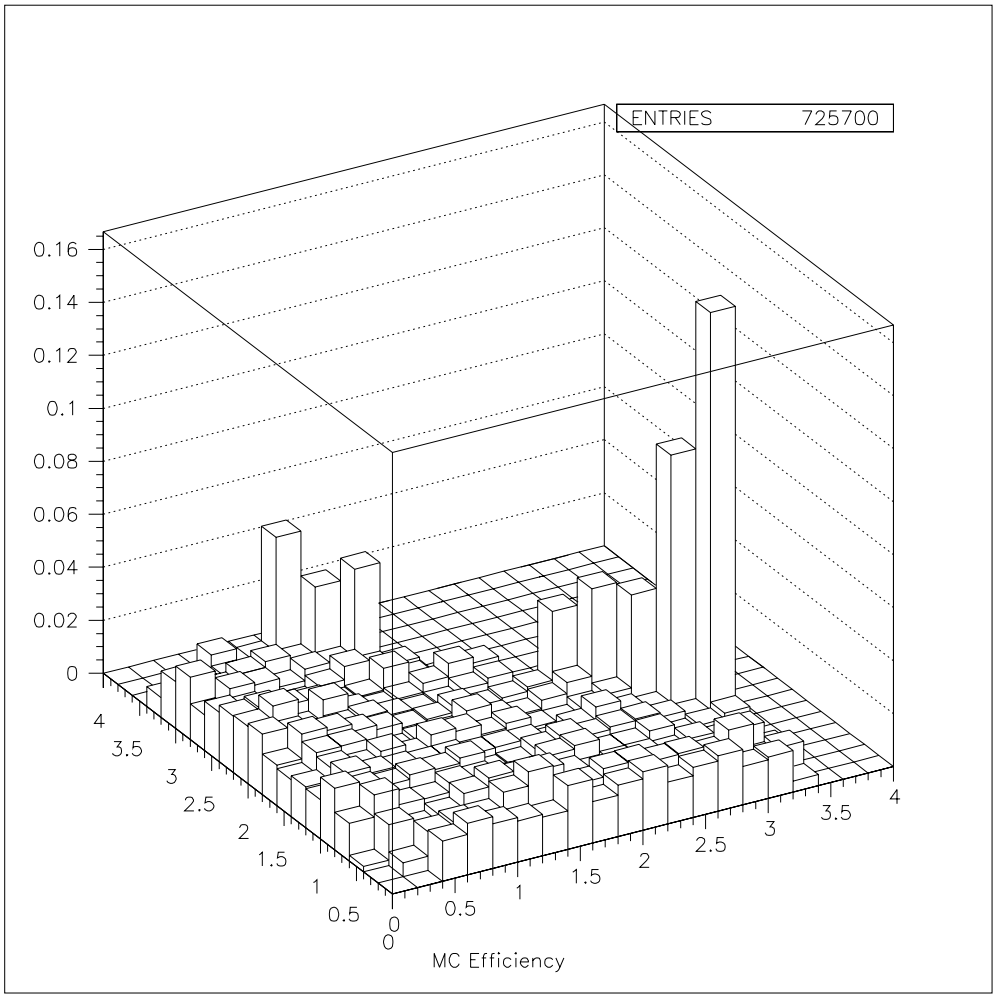

Fig. 8.4: Binned Efficiency Function

Except for some of the edge bins, the variation in efficiency across the Dalitz plot is seen to be fairly uniform. The value of the efficiency function for each bin is stored in a file for use in the maximum likelihood fit. The values in the file are the values of $\epsilon(\phi)$ for a given bin.

The edge bin fluctuations can be seen to be caused by the very small number of events in some bins of the Dalitz plot made from the thrown $D_s^+ \rightarrow \pi^+\pi^-\pi^+$ Monte Carlo sample. Dividing the number of surviving Monte Carlo events in a bin by the very small number of events in a bin from the thrown sample creates an artificially large weighting for those bins which is entirely the result of the binning used to striate the Dalitz plot. In Figure 8.5, a rotated view of Figure 8.2 shows these hardly-populated edge bins (n.b., the ones populated with 100 events, not the ones with 3000).

In this analysis, the edge bins that have fluctuated larger or smaller that the other neighboring bins are dealt with in two ways. The first is to actually use the efficiency function as is. Doing this will cause the bins that have fluctuated larger to provide a larger weight to data events in those bins than data events in near-by bins. However, it can be seen that these bins do not contain many data events. The final data sample Dalitz plot, divided into 20 bins for the range 0–4.0 GeV^2/c^4 along each $M^2_{\pi^+\pi^-}$ axis for the plot, is presented in Figure 8.6. The numbers of events in each bin is included in the plot. The edge bins on the diagonal all have seven or fewer events in them; some edge bins have no events.

The second method used is to simply remove events in the bins that have fluctuated when doing the fit. While this method certainly throws away fit information, it should not bias the the fit against any particular decay, and it certainly reduces the fluctuation in the efficiency function. It is assumed that there is not much information in a bin with 10% of its area in the allowed phase space region of the Dalitz plot. The two methods cover the two possible extremes—the first method is the one used in the analysis, and the second method is used to provide a systematic error in the error analysis chapter.

Regardless of the method used to address the few fluctuating bins, on an event by event basis, the analysis uses the stored value of the efficiency from the bin that contains the event's Dalitz point as the value of $\epsilon(\phi)$ for that event's contribution to the likelihood function.

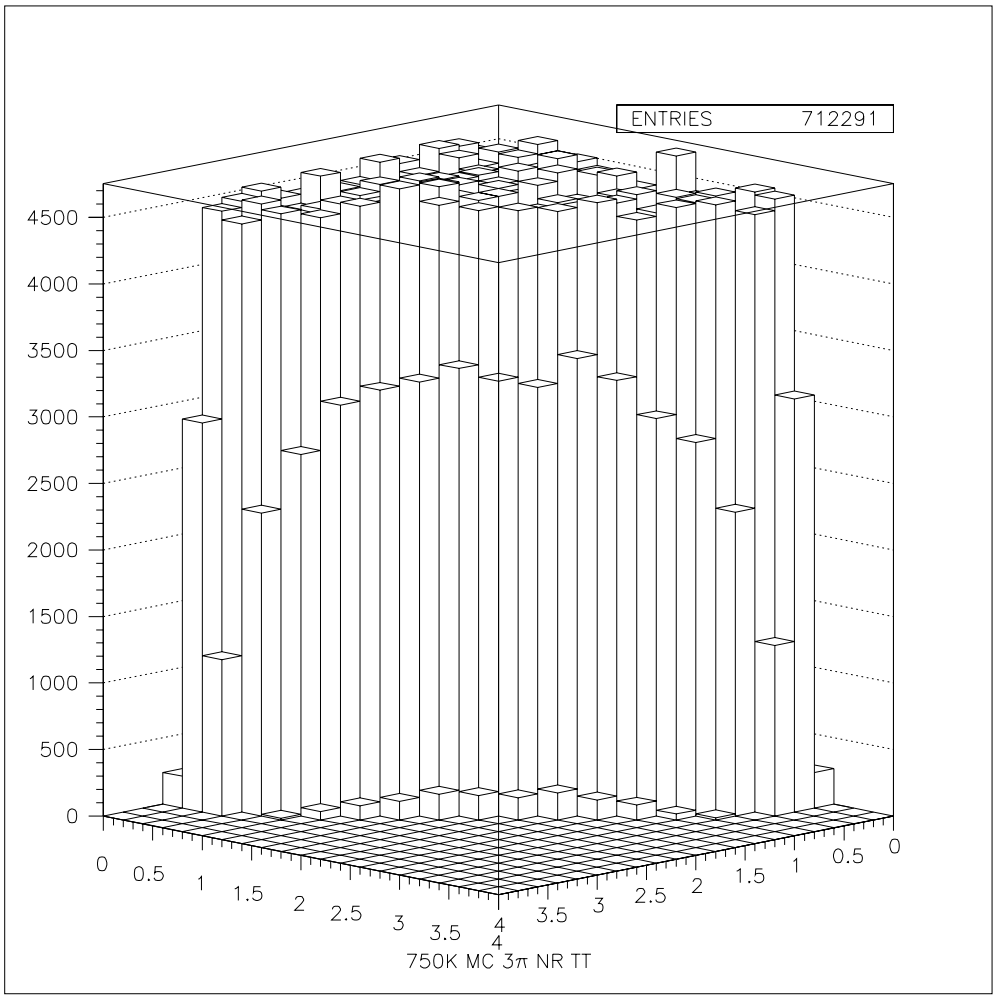

Fig. 8.5: Rotated View of Figure 8.2 Showing Low-Population Edge Bins

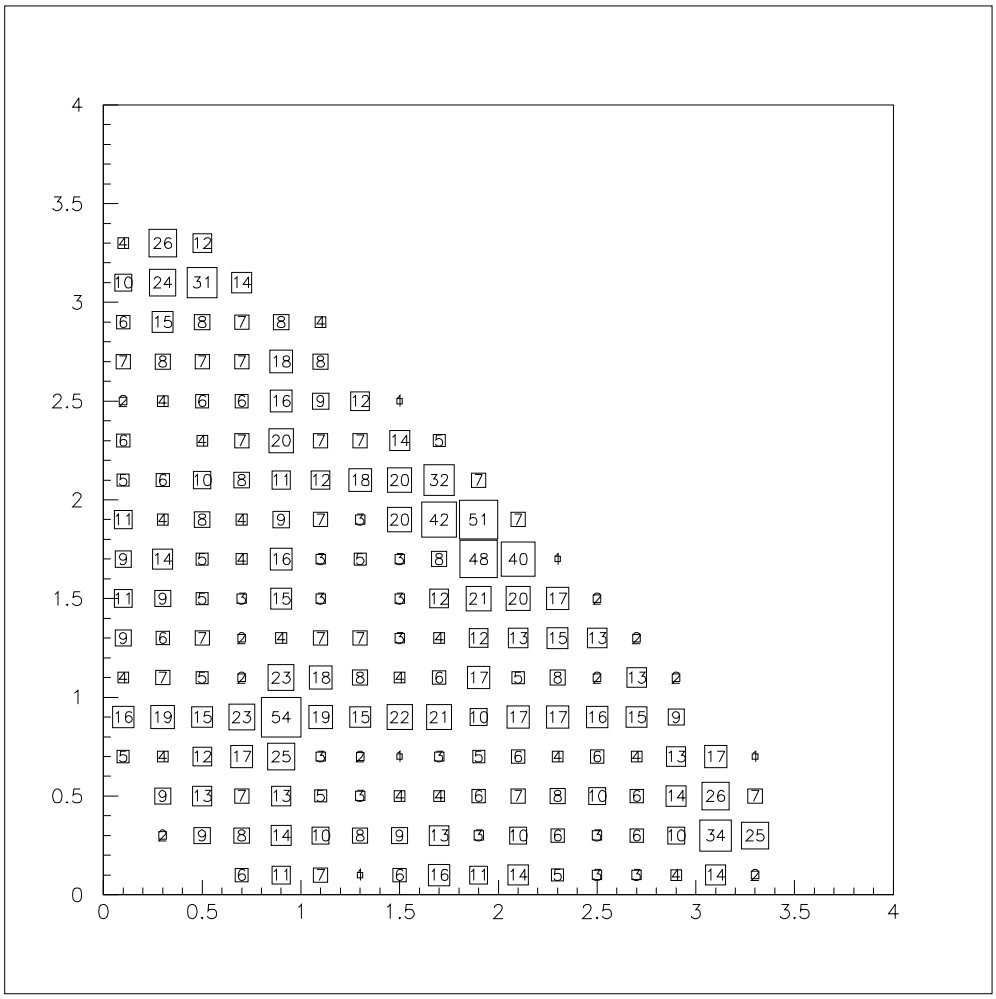

Fig. 8.6: Binned Data Dalitz Plot

8.5 Fit Formalism

This section outlines the fit formalism, and describes how the results of the previous three sections are combined to perform the maximum likelihood fit. The amplitude functions and efficiency calculations in the previous sections provide a complete set of building blocks to create the signal and background probability density functions as outlined in Chapter 7.

As a reminder, the form of the likelihood function is again provided here:

$$-\ln\mathcal{L} = -\sum_{i=1}^{n}\ln\left[\frac{S\cdot P_{iS}+B\cdot P_{iB}}{S+B}\right] - n\ln\nu - \nu + \sum_{i=1}^{n}\ln\epsilon(\phi)d\phi + \ln n! \tag{8.1}$$

along with the Signal PDF:

$$\mathcal{P}_S = \frac{1}{N_S}\frac{G(M_{3\pi})}{N_G}\epsilon(\phi)\sum_{i=1}^{m}\sum_{j=1}^{m}A_iA_j\mathcal{R}e\left[e^{i(\delta_i-\delta_j)}\frac{S_iS_j^*}{\sqrt{N_iN_j}}\right]d\phi \tag{8.2}$$

and the Background PDF:

$$\mathcal{P}_B = \frac{1}{N_b}\frac{E(M_{3\pi})}{N_E}\sum_{i=1}^{k}b_i\cdot B_i d\phi \tag{8.3}$$

The signal amplitudes (S_i) and background amplitudes (B_i) were were written to be independent of the fit parameters, and so had to be calculated only once in the beginning of the fit. These amplitudes were then used to calculate the normalization and phase space integrals, as well as being used in the respective probability density functions. However, if the mass or width of one of the resonances was allowed to float, some of the signal amplitudes are no longer independent of the fit parameters. Since the normaliations are dependent on the form of the signal amplitudes, the normalizations have to be re-calculated every time a new mass or width value is returned by the fitting code. The masses and widths were floated in the initial fits, but once found, were kept constant for the fits performed in the error analysis chapter.

The normalizations and other phase space integrals in the fit were calculated using Monte Carlo events generated according to $D_s \to \pi^+\pi^-\pi^+$ phase

space. For each signal resonance i, the normalization N_i was calculated using Equation 7.20. For each pair of resonances i and j, the coefficient E_{ij} used in the probability density functions was calculated using Equation 7.22, with Monte Carlo events which were reconstructed and passed all the analysis cuts (i.e., events that were accepted).

Once the normalizations are calculated and the starting values of the individual fit parameters are read in from a file, the fit program loops through the 2,568 events in the final data sample. For each event, the fit program uses the values of $M^2_{\pi_1^+\pi_2^-}$ and $M^2_{\pi_3^+\pi_2^-}$ for the three pions to calculate the P_{iS} and P_{iB} for the event using the Equations 8.2 and 8.3, and then uses Equation 8.1 to add the event's Signal and Background PDFs to the sum that is -ln$\mathcal{L}$. The total of the contributions from all events gives the value of -ln$\mathcal{L}$ for the particular set of input fit parameters.

The fit program next uses MINUIT [42] to vary the individual fit parameters in an ordered way, and recalculates -ln$\mathcal{L}$ by using the current set of fit parameters in another sum over all data events. This ordered varying of fit parameters and recalculation of -ln$\mathcal{L}$ procedure is repeated until the absolute minimum of -ln$\mathcal{L}$ is reached. Arriving at fit parameters that provide the most negative value of -ln$\mathcal{L}$ (those that minimize -ln$\mathcal{L}$) means that MINUIT has found the fit parameters that have maximized $\mathcal{L}$, the maximum likelihood function.

The signal amplitudes (A_i), relative phase angles (δ_i), the mass and width of the $f_0(980)$, the mass and width of the $f_0(1370)$ and the background probabilities (b_i) were the parameters determined in the fit. Although this is a large number of fit parameters (19), the fits were fairly stable, and minimization was usually reached in about 900–1000 interations.

One point of note is that since amplitudes and phases are only relative quantities, the signal amplitude for the $f_0(980)$ resonance was held constant to 1.0, and the signal phase for the $f_0(980)$ resonance was held constant to 0.0. The rest of the amplitudes and phases returned were expressed in relation to the fixed values of the $f_0(980)$ resonance input into MINUIT. Fixing one amplitude and one phase also had the additional benefit of reducing the number of fit parameters passed to MINUIT by two, to 17.

From the fit results, normalized physical fractions were calculated, which were used to compare results from different fits.

8.6 Fit Results

It was found that there were two solutions to the likelihood fit of the data sample. The two solutions were seen to have distinct minima. A procedure was developed to further examine the two solutions, consisting of performing one hundred fits with one hundred distinct sets of initialization parameters. For all resonance components but the reference component $f_0(980)$, the intensities A_i were randomly generated to have any value between 0 and 1, and the phases δ_i were randomly generated to have any value between 0 and 2π. The results of the procedure presented two and only two minima, with two and only two sets of reported final fit parameters. Though the minima reached in the fit depended on the initialization values for the fit parameters, no exact correllation was noted in the results of the fitting procedure. The solution with fcn = -41307.75 was found 71 times:

mode	intensity	phase (radians)	fraction
$f_0(980)\pi^+$	1(fixed)	0(fixed)	0.430 ± 0.026
non-resonant	0.278 ± 0.090	4.52 ± 0.451	0.011 ± 0.012
$\rho^0(770)\pi^+$	0.272 ± 0.064	4.69 ± 0.310	0.032 ± 0.015
$f_2(1270)\pi^+$	0.857 ± 0.051	3.75 ± 0.149	0.316 ± 0.028
$f_0(1370)\pi^+$	0.892 ± 0.070	2.71 ± 0.150	0.343 ± 0.042
$\rho^0(1450)\pi^+$	0.446 ± 0.046	2.74 ± 0.263	0.085 ± 0.017

Tab. 8.1: Final Solution

The solution with fcn = -41267.59 was found 29 times:

mode	intensity	phase (radians)	fraction
$f_0(980)\pi^+$	1(fixed)	0(fixed)	0.287 ± 0.024
non-resonant	0.156 ± 0.094	0.208 ± 0.342	0.022 ± 0.014
$\rho^0(770)\pi^+$	0.493 ± 0.097	4.179 ± 0.285	0.070 ± 0.025
$f_2(1270)\pi^+$	0.737 ± 0.091	0.264 ± 0.247	0.156 ± 0.031
$f_0(1370)\pi^+$	0.965 ± 0.098	5.777 ± 0.257	0.267 ± 0.046
$\rho^0(1450)\pi^+$	1.192 ± 0.126	0.481 ± 0.212	0.408 ± 0.080

Tab. 8.2: Second Final Solution

Both results reported accurate error matricies, but they present very different interpretations of physical reality. One solution has a dominant $f_0(980)\pi^+$ component, where the other has a more dominant $\rho^0(1450)\pi^+$ component. Both solutions are seen to indicate the presence of constructive interference. The solution found 71% of the time has

$$\Sigma(fractions) = 1.22$$

and the solution found the other 29% of the time has

$$\Sigma(fractions) = 1.21$$

In both solutions, the phases of the states $f_0(1370)\pi^+$ and $\rho^0(1450)\pi^+$ are relatively close to each other, but it can be seen that in the two solutions the phases of the two states with respect to the $f_0(980)\pi^+$ phase differ by a factor of π.

Two solve this ambiguity and select the true physical solution, a subset of the final data sample was created by tightening cuts. The tighter cut values used were SDZ $>$ 20, PTB $<$ 0.25 GeV/c and DIP $<$ 0.0020 cm. The cuts produced a sample with 672 signal events over a background of 430 events, as seen in Figure 8.7.

The procedure to perform 100 fits was repeated, again resulting in two distinct solutions, which are presented here. The fit with fcn = -13859.80 was found 70 times:

mode	intensity	phase (radians)	fraction
$f_0(980)\pi^+$	1(fixed)	0(fixed)	0.450 ± 0.030
non-resonant	0.235 ± 0.077	5.952 ± 0.401	0.025 ± 0.017
$\rho^0(770)\pi^+$	0.261 ± 0.064	4.689 ± 0.311	0.031 ± 0.015
$f_2(1270)\pi^+$	0.779 ± 0.058	3.936 ± 0.156	0.273 ± 0.033
$f_0(1370)\pi^+$	0.916 ± 0.086	3.027 ± 0.175	0.377 ± 0.054
$\rho^0(1450)\pi^+$	0.378 ± 0.055	2.872 ± 0.303	0.064 ± 0.018

Tab. 8.3: Final Solution—Tight Cuts

The fit with fcn = -13833.51 was found 30 times:

mode	intensity	phase (radians)	fraction
$f_0(980)\pi^+$	1(fixed)	0(fixed)	0.353 ± 0.032
non-resonant	0.131 ± 0.101	3.924 ± 1.143	0.006 ± 0.009
$\rho^0(770)\pi^+$	0.685 ± 0.090	0.076 ± 0.198	0.166 ± 0.037
$f_2(1270)\pi^+$	0.384 ± 0.079	2.499 ± 0.275	0.052 ± 0.021
$f_0(1370)\pi^+$	0.638 ± 0.123	1.383 ± 0.244	0.144 ± 0.056
$\rho^0(1450)\pi^+$	1.431 ± 0.125	2.075 ± 0.167	0.722 ± 0.083

Tab. 8.4: Second Final Solution—Tight Cuts

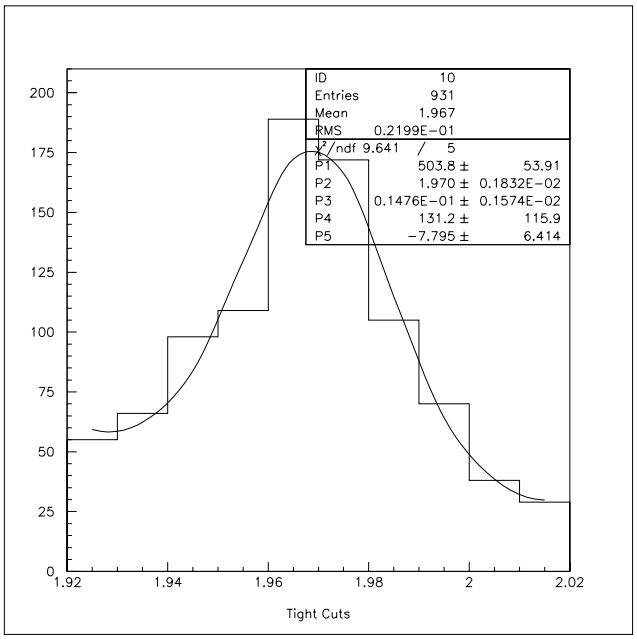

Fig. 8.7: Final Data Sample After Tight Cuts

It can be seen that within errors, solution 1 from the tight set of cuts (Table 8.3) matches all fit parameters and the calculated physical fractions of solution 1 from the original fit (Table 8.1). From this exercise, solution 1 is taken to be the correct solution. It is heartening that the matching solutions each have the lower fcn of their pair, and that they were the solution found

more than twice as often.

The fit values of the background fractions and of the masses and widths of the two f_0 resonances for solution 1 are presented in Table 8.5.

Fit Parameter	Fit Value
NR Background	75.6 ± 2.8
$D^0 \to K\pi$ Background	18.7 ± 1.1%
$D_s \to \eta\pi$ Background	5.2 ± 0.6%
$f_0(980)$ mass (GeV/c^2)	974 ± 4
$f_0(980)$ width (MeV/c^2)	44 ± 5
$f_0(1370)$ mass (GeV/c^2)	1442 ± 20
$f_0(1370)$ width (MeV/c^2)	167 ± 32

Tab. 8.5: Fit Background Fractions and Resonance Masses and Widths

8.7 Goodness of Fit

To test how well the obtained fit matches data, 10,000 Monte Carlo events were generated, setting the contributions from each mode by inputting the amplitude and phase values obtained in the fit. The Monte Carlo and final data sample Dalitz plots are binned, and the number of events in each bin compared to provide a χ^2 distribution, with contributions from each bin summing to give the total χ^2/DOF. The Monte Carlo sample is scaled before making the comparison, with

$$N = \frac{Number\ in\ Final\ Data\ Sample}{Number\ Monte\ Carlo\ Events\ Generated}$$

To calculate the χ^2 distribution, χ_i^2 is defined for each bin:

$$\chi_i^2 = \left[\frac{n_i^{data} - N \cdot n_i^{MC}}{\sqrt{N \cdot n_i^{MC}}}\right]^2$$

where n_i^{MC} is the number of Monte Carlo events in bin i and n_i^{data} is the number of data events in bin i. The overall χ^2/DOF is then defined as the sum over the N_{bins} bins in the Dalitz plot:

$$\chi^2/DOF = \sum_{i=1}^{N_{bins}} \chi_i^2/N_{bins}$$

The folded Dalitz plot of the final data sample, the folded Dalitz plot of the Monte Carlo events, the contribution of each bin to the total χ^2/DOF and the projections of the Monte Carlo and data event Dalitz plots plotted together, can be seen in Figure 8.8.

The plots show that there is good agreement between the fit and the data that the fit is trying to represent.

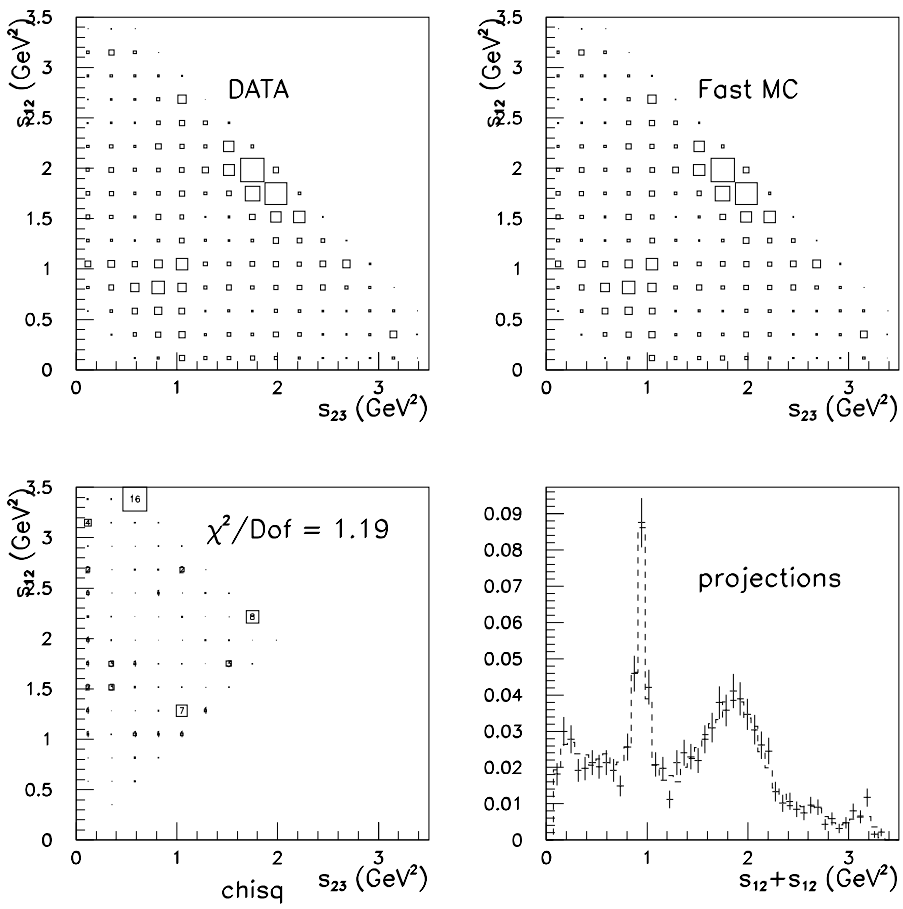

Fig. 8.8: a) Final Data Sample Distribution; b) Monte Carlo Distribution; c) χ^2/bin comparing MC and fit; d) s_{12} and s_{23} projections for data (plotted) and MC (points with error bars)

9. MEASUREMENT ERRORS

9.1 Introduction and Overview

This chapter examines the statistical and systematic errors associated with the measurements made in this thesis. Statistical errors are effects in data that originate because of fluctuations that arise from the finite number of events in the fit.

Systematic errors are effects that originate because of the methodology used to make the measurement. If an alternate method was used, or a different model of the data employed, the result might change. Some of the techniques used to determine the systematic errors are to individually vary factors used in the model or to split the data sample into specific subsets. The variations in fit parameters obtained from the changed model or split data sample provide a measurement of the systematic errors associated with the fit technique.

Table 9.1, the final table of fit parameter results, includes the statistical and systematic errors as separate errors to the fit.

9.2 Check of Statistical Errors Reported by MINUIT

This section examines the statistical errors reported from the fitter. MINUIT uses the matrix equation

$$\left[\frac{\partial^2(-ln\mathcal{L})}{\partial\alpha_i\partial\alpha_j}\right]^{-1}$$

evaluated at the final value of the fit parameters (those that maximize $\mathcal{L}$) to estimate the matrix of statistical errors. At the end of the fit, the values of those errors are accessible via an include file (and are used in the calculation of the physical fractions, as seen in Section 7.3.5). As a check that these

values are an accurate representation of the parameter variations, a test using separate sets of generated Monte Carlo data was performed. Events in the individual sets were generated according to the final fit parameter values (including background), and then fit with the fitting program. The number of events in each individual set was taken from a gaussian distribution, centered around the total number of events in the data sample (2,568), with a width of $\sqrt{2568}$. There were 500 individual sets generated. The output of the fit parameters was used to check that the distribution of each fit parameter for the 500 individual fits was reasonable, by comparing the RMS of the parameter distributions from the 500 fits with the output errors for the fit parameters from MINUIT. The distributions were gaussian, and the results of this study demonstrate that the fitting procedure does not introduce any bias—for all 15 signal amplitude fit parameters, the mean of the fit parameter distributions from the 500 fits was centered very near the mean of the MINUIT fit parameter.

It was also seen that the errors in the MINUIT data fit were well matched to the RMS of the gaussian distribution of the 500 sets of Monte Carlo fit parameters, although in all 15 fit parameter cases, the data fit errors were slightly larger than the RMS of the distributions. Instead of those obtained by the above method, the final statistical errors in Table 9.1 conservatively report the larger data fit errors obtained for each parameter.

9.3 Systematic Studies

The systematic errors are estimated by determining the differences in the data fit parameters obtained with different fitting techniques, as well as examining the non-statistical differences in the data fit parameters obtained by fitting separate subsamples of the data set. Each of the following subsections provides an overview of the method used to alter the original fit, and then presents a table of the results of the fit for the six signal amplitudes. The final set of systematic errors reported in Table 9.1 are the sum of the systematic errors obtained from each of the following studies added in quadrature. The systematic errors are seen to be smaller than the statistical errors for almost all parameters.

Tab. 9.1: Final Result with Statistic and Systematic Errors

mode	intensity	phase (radians)	fraction
$f_0(980)\pi^+$	1(fixed)	0(fixed)	$0.430 \pm 0.026 \pm 0.042$
non-resonant	$0.278 \pm 0.090 \pm 0.030$	$4.52 \pm 0.45 \pm 0.59$	$0.011 \pm 0.012 \pm 0.004$
$\rho^0(770)\pi^+$	$0.272 \pm 0.064 \pm 0.172$	$4.69 \pm 0.31 \pm 0.07$	$0.032 \pm 0.015 \pm 0.032$
$f_2(1270)\pi^+$	$0.857 \pm 0.051 \pm 0.013$	$3.75 \pm 0.15 \pm 0.46$	$0.316 \pm 0.028 \pm 0.005$
$f_0(1370)\pi^+$	$0.892 \pm 0.070 \pm 0.024$	$2.71 \pm 0.15 \pm 0.45$	$0.343 \pm 0.042 \pm 0.017$
$\rho^0(1450)\pi^+$	$0.446 \pm 0.046 \pm 0.008$	$2.74 \pm 0.26 \pm 0.26$	$0.085 \pm 0.017 \pm 0.002$

9.3.1 Variation of Background Exponential

The background in Figure 1.2 is fit with an exponential over the mass range 1.82 - 2.07 GeV/c^2. Changing the slope of the exponent changes the number of signal and background events in the fit of the three pion mass distribution. The number of signal and background events obtained have errors associated with them due to uncertainties in the exponent and the other fit parameters which are allowed to float in the fit. This section examines how the maximum likelihood fit is affected by varying the slope of the exponent by $\pm 1\sigma$ from the reported mean fit value.

The slope fit value in Figure 1.2 is –5.762±0.328, meaning the original fit used the form

$$e^{-5.762 \cdot M_{\pi\pi\pi}}$$

to describe the background over the $M_{\pi\pi\pi}$ range 1.82 - 2.07 GeV/c^2. Adding the reported 1σ error to the slope gives the value –5.434, while subtracting it results in the value –6.090. A fit of the three pion mass distribution was performed with the slope held constant for each of the $\pm 1\sigma$ values. In each fit, the number of signal and background events were allowed to float. For each fit, the number of signal and background events obtained changed from those originally obtained in Figure 1.2 as a result of the change in the slope of the exponent. The final step in this particular systematic error analysis is to input these new signal and background event values as constants into the maximum likelihood fit. MINUIT converged for the two fits performed, providing accurate error matricies. The changes in the fit parameters for the two changes to the exponent are presented here.

Tab. 9.2: Fit Result With Exponential Slope Fixed at –5.434

mode	intensity	phase (radians)	fraction
$f_0(980)\pi^+$	1(fixed)	0(fixed)	0.438 ± 0.026
non-resonant	0.212 ± 0.097	4.52 ± 0.45	0.010 ± 0.011
$\rho^0(770)\pi^+$	0.274 ± 0.061	4.67 ± 0.33	0.033 ± 0.015
$f_2(1270)\pi^+$	0.859 ± 0.051	3.74 ± 0.15	0.314 ± 0.028
$f_0(1370)\pi^+$	0.883 ± 0.069	2.72 ± 0.15	0.339 ± 0.043
$\rho^0(1450)\pi^+$	0.447 ± 0.046	2.74 ± 0.26	0.085 ± 0.017

Tab. 9.3: Fit Result With Exponential Slope Fixed at –6.090

mode	intensity	phase (radians)	fraction
$f_0(980)\pi^+$	1(fixed)	0(fixed)	0.426 ± 0.025
non-resonant	0.240 ± 0.089	4.72 ± 0.62	0.008 ± 0.014
$\rho^0(770)\pi^+$	0.278 ± 0.064	4.61 ± 0.30	0.034 ± 0.015
$f_2(1270)\pi^+$	0.859 ± 0.051	3.73 ± 0.15	0.316 ± 0.028
$f_0(1370)\pi^+$	0.892 ± 0.069	2.71 ± 0.15	0.348 ± 0.041
$\rho^0(1450)\pi^+$	0.453 ± 0.047	2.72 ± 0.26	0.089 ± 0.018

Variation of D^0 Background

The percentages of the three incoherent backgrounds were allowed to float in the the maximum likelihood fit. For the model used, it was found that 18.7 ± 1.1% of the background came from the D^0 component. This section examines the effect of varying the percentage of D^0 background from the original values returned from the fit. The number of signal and background events obtained in the original fit were held fixed, and the amount of D^0 background was varied by ± 1σ (i.e., fixed at 19.8% and at 17.6%). For each fit, MINUIT converged, providing accurate error matricies. The changes in the fit parameters for the two fractions of D^0 background are presented here.

Tab. 9.4: Fit Result With 19.8% D^0 Background

mode	intensity	phase (radians)	fraction
$f_0(980)\pi^+$	1(fixed)	0(fixed)	0.438 ± 0.026
non-resonant	0.283 ± 0.094	4.50 ± 0.43	0.009 ± 0.008
$\rho^0(770)\pi^+$	0.270 ± 0.063	4.64 ± 0.34	0.030 ± 0.015
$f_2(1270)\pi^+$	0.842 ± 0.051	3.74 ± 0.16	0.315 ± 0.028
$f_0(1370)\pi^+$	0.888 ± 0.073	2.68 ± 0.14	0.321 ± 0.044
$\rho^0(1450)\pi^+$	0.444 ± 0.046	2.73 ± 0.28	0.085 ± 0.017

Tab. 9.5: Fit Result With 17.6% D^0 Background

mode	intensity	phase (radians)	fraction
$f_0(980)\pi^+$	1(fixed)	0(fixed)	0.421 ± 0.025
non-resonant	0.202 ± 0.084	4.80 ± 0.84	0.004 ± 0.006
$\rho^0(770)\pi^+$	0.277 ± 0.064	4.51 ± 0.32	0.033 ± 0.015
$f_2(1270)\pi^+$	0.863 ± 0.051	3.68 ± 0.15	0.319 ± 0.028
$f_0(1370)\pi^+$	0.904 ± 0.072	2.70 ± 0.15	0.352 ± 0.041
$\rho^0(1450)\pi^+$	0.460 ± 0.048	2.73 ± 0.26	0.089 ± 0.018

Variation of $D_s \to \eta'\pi$ Background

This section proceeds exactly as the previous. For the model used, it was found that 5.2 ± 0.6% of the background came from the $D_s \to \eta'\pi$ component. This section examines the effect of varying the percentage of $D_s \to \eta'\pi$ background from the original values returned from the fit. The number of signal and background events were held fixed, and the amount of $D_s \to \eta'\pi$ background was varied by $\pm 1\sigma$ (i.e., fixed at 5.8% and at 4.6%). For each fit, MINUIT converged, providing accurate error matricies. The changes in the fit parameters for the two changes to the $D_s \to \eta'\pi$ background are presented here.

Tab. 9.6: Fit Result With 5.8% $D_s \to \eta'\pi$ Background

mode	intensity	phase (radians)	fraction
$f_0(980)\pi^+$	1(fixed)	0(fixed)	0.428 ± 0.026
non-resonant	0.255 ± 0.091	4.47 ± 0.48	0.007 ± 0.010
$\rho^0(770)\pi^+$	0.275 ± 0.063	4.65 ± 0.32	0.031 ± 0.016
$f_2(1270)\pi^+$	0.852 ± 0.051	3.72 ± 0.15	0.318 ± 0.029
$f_0(1370)\pi^+$	0.893 ± 0.071	2.70 ± 0.15	0.346 ± 0.043
$\rho^0(1450)\pi^+$	0.450 ± 0.044	2.73 ± 0.24	0.088 ± 0.018

Tab. 9.7: Fit Result With 4.6% $D_s \to \eta'\pi$ Background

mode	intensity	phase (radians)	fraction
$f_0(980)\pi^+$	1(fixed)	0(fixed)	0.438 ± 0.027
non-resonant	0.270 ± 0.089	4.66 ± 0.48	0.002 ± 0.010
$\rho^0(770)\pi^+$	0.266 ± 0.063	4.69 ± 0.31	0.031 ± 0.015
$f_2(1270)\pi^+$	0.854 ± 0.051	3.75 ± 0.15	0.317 ± 0.028
$f_0(1370)\pi^+$	0.885 ± 0.070	2.70 ± 0.15	0.342 ± 0.042
$\rho^0(1450)\pi^+$	0.451 ± 0.048	2.79 ± 0.28	0.087 ± 0.017

9.3.2 Variation of Blatt Weisskopf Form Factors

The Blatt Weisskopf form factors were used in Equation 7.34 to provide a means to include a phenomenologically deduced momentum scale to the coupling at a vertex. It multiplies the form of each resonance partial width. This section examines the effect of removing this from the model, by performing a maximum likelihood fit with the form factors set to unity. In the fit, MINUIT converged, providing accurate error matricies. The changes in the fit parameters with the removal of the form factors presented here.

Tab. 9.8: Fit Result With $F_D = 1$ and $F_r = 1$

mode	intensity	phase (radians)	fraction
$f_0(980)\pi^+$	1(fixed)	0(fixed)	0.429 ± 0.025
non-resonant	0.301 ± 0.079	4.57 ± 0.46	0.008 ± 0.010
$\rho^0(770)\pi^+$	0.271 ± 0.064	4.70 ± 0.34	0.032 ± 0.015
$f_2(1270)\pi^+$	0.861 ± 0.051	3.74 ± 0.15	0.318 ± 0.028
$f_0(1370)\pi^+$	0.899 ± 0.071	2.68 ± 0.15	0.346 ± 0.041
$\rho^0(1450)\pi^+$	0.453 ± 0.049	2.70 ± 0.27	0.086 ± 0.018

9.3.3 Bins of D_s Charge

This section presents an examination of effects on the analysis that might arise from the experimental apparatus or the event selection and fitting technique. By dividing the final data sample into events containing $D_s^+ \to \pi^+\pi^-\pi^+$ and those containing $D_s^- \to \pi^-\pi^+\pi^-$, any variation of the fit parameters from this effect will be estimated. In each case, MINUIT converged, providing accurate error matricies. The changes in the fit parameters for separate fits to each of two subsamples are presented here.

Tab. 9.9: Fit Result For D_s^+

mode	intensity	phase (radians)	fraction
$f_0(980)\pi^+$	1(fixed)	0(fixed)	0.454 ± 0.022
non-resonant	0.238 ± 0.101	4.48 ± 0.26	0.026 ± 0.021
$\rho^0(770)\pi^+$	0.169 ± 0.075	4.60 ± 0.41	0.013 ± 0.012
$f_2(1270)\pi^+$	0.808 ± 0.058	0.85 ± 0.15	0.296 ± 0.041
$f_0(1370)\pi^+$	0.806 ± 0.079	2.79 ± 0.14	0.295 ± 0.052
$\rho^0(1450)\pi^+$	0.499 ± 0.062	3.15 ± 0.26	0.113 ± 0.026

Tab. 9.10: Fit Result For D_s^-

mode	intensity	phase (radians)	fraction
$f_0(980)\pi^+$	1(fixed)	0(fixed)	0.382 ± 0.042
non-resonant	0.137 ± 0.114	5.42 ± 0.84	0.007 ± 0.013
$\rho^0(770)\pi^+$	0.474 ± 0.083	4.81 ± 0.23	0.086 ± 0.027
$f_2(1270)\pi^+$	0.901 ± 0.090	3.20 ± 0.17	0.310 ± 0.038
$f_0(1370)\pi^+$	0.997 ± 0.121	2.48 ± 0.17	0.380 ± 0.063
$\rho^0(1450)\pi^+$	0.508 ± 0.087	1.86 ± 0.27	0.099 ± 0.034

9.3.4 Bins of D_s Momentum

This section also presents an examination of effects on the analysis that might arise from the experimental apparatus or the event selection and fitting technique. Many acceptance and efficiency corrections are momentum dependent. By dividing the final data sample into subsamples containing events with different D_s momenta (P_{D_s}), any variation of the fit parameters from these effects will be estimated. The data sample was divided into three momentum ranges as described in the titles of the tables. In each case, MINUIT converged, providing accurate error matricies. The changes in the fit parameters for separate fits to each of three subsamples are presented here.

Tab. 9.11: Fit Result For 0 $GeV/c^2 < P_{D_s} < 39$ GeV/c^2

mode	intensity	phase (radians)	fraction
$f_0(980)\pi^+$	1(fixed)	0(fixed)	0.320 ± 0.039
non-resonant	0.502 ± 0.120	5.58 ± 0.67	0.116 ± 0.084
$\rho^0(770)\pi^+$	0.269 ± 0.094	4.69 ± 0.40	0.020 ± 0.017
$f_2(1270)\pi^+$	0.912 ± 0.080	4.87 ± 0.34	0.290 ± 0.051
$f_0(1370)\pi^+$	0.956 ± 0.103	3.97 ± 0.41	0.339 ± 0.069
$\rho^0(1450)\pi^+$	0.720 ± 0.130	4.79 ± 0.59	0.180 ± 0.062

Tab. 9.12: Fit Result For 39 $GeV/c^2 \leq P_{D_s} < 62\ GeV/c^2$

mode	intensity	phase (radians)	fraction
$f_0(980)\pi^+$	1(fixed)	0(fixed)	0.457 ± 0.062
non-resonant	0.340 ± 0.128	2.52 ± 0.44	0.079 ± 0.037
$\rho^0(770)\pi^+$	0.282 ± 0.070	5.69 ± 0.34	0.038 ± 0.016
$f_2(1270)\pi^+$	0.769 ± 0.074	3.20 ± 0.14	0.249 ± 0.037
$f_0(1370)\pi^+$	0.740 ± 0.109	2.04 ± 0.14	0.286 ± 0.050
$\rho^0(1450)\pi^+$	0.555 ± 0.070	2.12 ± 0.25	0.103 ± 0.034

Tab. 9.13: Fit Result For $P_{D_s} \geq 62\ GeV/c^2$

mode	intensity	phase (radians)	fraction
$f_0(980)\pi^+$	1(fixed)	0(fixed)	0.440 ± 0.036
non-resonant	0.212 ± 0.114	3.14 ± 0.92	0.009 ± 0.014
$\rho^0(770)\pi^+$	0.308 ± 0.077	5.02 ± 0.30	0.071 ± 0.020
$f_2(1270)\pi^+$	0.826 ± 0.055	3.36 ± 0.16	0.328 ± 0.041
$f_0(1370)\pi^+$	0.840 ± 0.080	2.37 ± 0.21	0.284 ± 0.060
$\rho^0(1450)\pi^+$	0.552 ± 0.076	2.49 ± 0.20	0.170 ± 0.039

9.3.5 Bins of D_s Transverse Momentum

This section presents another examination of effects on the analysis that might arise from the experimental apparatus or the event selection and fitting technique. The previous section examined total momentum, this section examines the transverse momentum (P_t) component of the D_s, which is defined in terms of the X and Y components of the D_s momentum by the equation $P_t = \sqrt{P_x^2 + P_y^2}$. By dividing the final data sample into subsamples containing events with different D_s transverse momenta, any variation of the fit parameters from these effects will be estimated. The data sample was divided into three transverse momentum ranges as described in the titles of the tables. In each case, MINUIT converged, providing accurate error matricies. The changes in the fit parameters for separate fits to each of three subsamples are presented here.

Tab. 9.14: Fit Result For 0 $GeV/c \leq P_t < 0.65$ GeV/c

mode	intensity	phase (radians)	fraction
$f_0(980)\pi^+$	1(fixed)	0(fixed)	0.343 ± 0.037
non-resonant	0.595 ± 0.133	6.00 ± 0.33	0.122 ± 0.063
$\rho^0(770)\pi^+$	0.267 ± 0.111	4.65 ± 0.43	0.024 ± 0.019
$f_2(1270)\pi^+$	0.905 ± 0.089	5.25 ± 0.37	0.281 ± 0.062
$f_0(1370)\pi^+$	1.021 ± 0.132	4.22 ± 0.45	0.358 ± 0.079
$\rho^0(1450)\pi^+$	0.702 ± 0.175	5.33 ± 0.55	0.169 ± 0.071

Tab. 9.15: Fit Result For 0.65 $GeV/c \leq P_t < 1.15\ GeV/c$

mode	intensity	phase (radians)	fraction
$f_0(980)\pi^+$	1(fixed)	0(fixed)	0.462 ± 0.057
non-resonant	0.383 ± 0.104	1.67 ± 0.45	0.068 ± 0.031
$\rho^0(770)\pi^+$	0.261 ± 0.079	5.62 ± 0.31	0.032 ± 0.018
$f_2(1270)\pi^+$	0.752 ± 0.077	2.70 ± 0.15	0.261 ± 0.041
$f_0(1370)\pi^+$	0.755 ± 0.104	1.82 ± 0.15	0.263 ± 0.055
$\rho^0(1450)\pi^+$	0.535 ± 0.075	1.83 ± 0.26	0.132 ± 0.039

Tab. 9.16: Fit Result For $P_t \geq 1.15\ GeV/c$

mode	intensity	phase (radians)	fraction
$f_0(980)\pi^+$	1(fixed)	0(fixed)	0.456 ± 0.031
non-resonant	0.131 ± 0.105	3.85 ± 0.81	0.008 ± 0.012
$\rho^0(770)\pi^+$	0.404 ± 0.083	5.53 ± 0.27	0.075 ± 0.029
$f_2(1270)\pi^+$	0.818 ± 0.075	3.39 ± 0.17	0.305 ± 0.045
$f_0(1370)\pi^+$	0.755 ± 0.098	2.36 ± 0.23	0.260 ± 0.065
$\rho^0(1450)\pi^+$	0.628 ± 0.086	2.06 ± 0.19	0.180 ± 0.044

9.3.6 Removal of Edge Bins

In section 8.4 it was seen that due to the bin size chosen to divide the Dalitz plot, some of the edge bins were not as populated as other bins. The binning had the effect of creating a large value of efficiency for these edge bins. This section examines the effect of performing the maximum likelihood fit when events in these edge bins are discarded. In the fit, MINUIT converged, providing accurate error matricies. The changes in the fit parameters for the fit is presented here.

Tab. 9.17: Fit Result Removing Edge Bins

mode	intensity	phase (radians)	fraction
$f_0(980)\pi^+$	1(fixed)	0(fixed)	0.432 ± 0.027
non-resonant	0.277 ± 0.088	4.51 ± 0.48	0.009 ± 0.012
$\rho^0(770)\pi^+$	0.274 ± 0.064	4.69 ± 0.33	0.032 ± 0.016
$f_2(1270)\pi^+$	0.852 ± 0.051	3.73 ± 0.15	0.319 ± 0.024
$f_0(1370)\pi^+$	0.893 ± 0.071	2.74 ± 0.15	0.340 ± 0.041
$\rho^0(1450)\pi^+$	0.440 ± 0.046	2.71 ± 0.25	0.085 ± 0.017

9.3.7 Varying Mass and Width of $f_0(980)$

Except for the $f_0(980)$ and $f_0(1370)$, the masses and widths of the signal amplitudes are fixed when the maximum likelihood fit was performed. This section examines the effect of varying the mass and width of the $f_0(980)$ by $\pm 1\sigma$ around the central value returned by the fit. Four separate fits were performed, with the $f_0(980)$ resonance parameters fixed to the values as described in the titles of the tables. In each case, MINUIT converged, providing accurate error matricies. The changes in the fit parameters for the four separate fits are presented here.

Tab. 9.18: Fit Result For $f_0(980)$ Mass at 0.975 GeV/c^2

mode	intensity	phase (radians)	fraction
$f_0(980)\pi^+$	1(fixed)	0(fixed)	0.426 ± 0.026
non-resonant	0.251 ± 0.092	4.01 ± 0.50	0.004 ± 0.009
$\rho^0(770)\pi^+$	0.280 ± 0.063	4.88 ± 0.31	0.029 ± 0.015
$f_2(1270)\pi^+$	0.855 ± 0.052	3.73 ± 0.15	0.289 ± 0.027
$f_0(1370)\pi^+$	0.899 ± 0.070	2.42 ± 0.14	0.354 ± 0.042
$\rho^0(1450)\pi^+$	0.480 ± 0.047	2.57 ± 0.24	0.087 ± 0.018

Tab. 9.19: Fit Result For $f_0(980)$ Mass at 0.983 GeV/c^2

mode	intensity	phase (radians)	fraction
$f_0(980)\pi^+$	1(fixed)	0(fixed)	0.432 ± 0.026
non-resonant	0.260 ± 0.094	4.66 ± 0.48	0.005 ± 0.011
$\rho^0(770)\pi^+$	0.271 ± 0.064	4.68 ± 0.31	0.032 ± 0.015
$f_2(1270)\pi^+$	0.857 ± 0.050	3.74 ± 0.15	0.316 ± 0.028
$f_0(1370)\pi^+$	0.892 ± 0.071	2.76 ± 0.15	0.342 ± 0.042
$\rho^0(1450)\pi^+$	0.455 ± 0.046	2.73 ± 0.25	0.084 ± 0.017

Tab. 9.20: Fit Result For $f_0(980)$ Width at 0.035 GeV/c^2

mode	intensity	phase (radians)	fraction
$f_0(980)\pi^+$	1(fixed)	0(fixed)	0.403 ± 0.022
non-resonant	0.348 ± 0.121	3.87 ± 0.58	0.010 ± 0.012
$\rho^0(770)\pi^+$	0.263 ± 0.064	4.64 ± 0.30	0.032 ± 0.015
$f_2(1270)\pi^+$	0.859 ± 0.052	3.72 ± 0.15	0.328 ± 0.029
$f_0(1370)\pi^+$	0.849 ± 0.067	2.59 ± 0.13	0.353 ± 0.040
$\rho^0(1450)\pi^+$	0.438 ± 0.045	2.74 ± 0.28	0.087 ± 0.017

Tab. 9.21: Fit Result For $f_0(980)$ Width at 0.045 GeV/c^2

mode	intensity	phase (radians)	fraction
$f_0(980)\pi^+$	1(fixed)	0(fixed)	0.436 ± 0.028
non-resonant	0.245 ± 0.118	4.02 ± 0.56	0.006 ± 0.007
$\rho^0(770)\pi^+$	0.264 ± 0.064	4.45 ± 0.31	0.033 ± 0.015
$f_2(1270)\pi^+$	0.867 ± 0.055	3.46 ± 0.15	0.322 ± 0.025
$f_0(1370)\pi^+$	0.894 ± 0.072	2.66 ± 0.15	0.337 ± 0.037
$\rho^0(1450)\pi^+$	0.461 ± 0.044	2.74 ± 0.26	0.084 ± 0.017

9.3.8 Varying Mass and Width of $f_0(1370)$

Like the previous section's examination of the $f_0(980)$, this section examines the effect of varying the mass and width of the $f_0(1370)$ by $\pm 1\sigma$ around the central value returned by the fit. Four separate fits were performed, with the $f_0(1370)$ resonance parameters fixed to the values as described in the titles of the tables. In each case, MINUIT converged, providing accurate error matricies. The changes in the fit parameters for the four separate fits are presented here.

Tab. 9.22: Fit Result For $f_0(1370)$ Mass at 1.422 GeV/c^2

mode	intensity	phase (radians)	fraction
$f_0(980)\pi^+$	1(fixed)	0(fixed)	0.422 ± 0.026
non-resonant	0.331 ± 0.087	4.80 ± 0.48	0.018 ± 0.011
$\rho^0(770)\pi^+$	0.258 ± 0.061	4.38 ± 0.31	0.033 ± 0.017
$f_2(1270)\pi^+$	0.866 ± 0.051	3.66 ± 0.16	0.320 ± 0.031
$f_0(1370)\pi^+$	0.887 ± 0.070	2.78 ± 0.17	0.317 ± 0.035
$\rho^0(1450)\pi^+$	0.445 ± 0.046	2.67 ± 0.26	0.085 ± 0.017

Tab. 9.23: Fit Result For $f_0(1370)$ Mass at 1.460 GeV/c^2

mode	intensity	phase (radians)	fraction
$f_0(980)\pi^+$	1(fixed)	0(fixed)	0.460 ± 0.031
non-resonant	0.301 ± 0.089	4.51 ± 0.45	0.010 ± 0.009
$\rho^0(770)\pi^+$	0.272 ± 0.064	4.66 ± 0.31	0.032 ± 0.015
$f_2(1270)\pi^+$	0.840 ± 0.049	3.78 ± 0.15	0.304 ± 0.025
$f_0(1370)\pi^+$	0.892 ± 0.067	2.70 ± 0.15	0.351 ± 0.037
$\rho^0(1450)\pi^+$	0.453 ± 0.041	2.74 ± 0.26	0.090 ± 0.018

Tab. 9.24: Fit Result For $f_0(1370)$ Width at 0.136 GeV/c^2

mode	intensity	phase (radians)	fraction
$f_0(980)\pi^+$	1(fixed)	0(fixed)	0.441 ± 0.024
non-resonant	0.312 ± 0.096	4.31 ± 0.37	0.002 ± 0.018
$\rho^0(770)\pi^+$	0.271 ± 0.064	4.91 ± 0.33	0.032 ± 0.015
$f_2(1270)\pi^+$	0.855 ± 0.052	3.68 ± 0.14	0.324 ± 0.028
$f_0(1370)\pi^+$	0.847 ± 0.070	2.70 ± 0.17	0.302 ± 0.040
$\rho^0(1450)\pi^+$	0.447 ± 0.045	2.74 ± 0.25	0.083 ± 0.017

Tab. 9.25: Fit Result For $f_0(1370)$ Width at 0.194 GeV/c^2

mode	intensity	phase (radians)	fraction
$f_0(980)\pi^+$	1(fixed)	0(fixed)	0.429 ± 0.022
non-resonant	0.247 ± 0.101	3.88 ± 0.50	0.001 ± 0.009
$\rho^0(770)\pi^+$	0.265 ± 0.065	4.50 ± 0.29	0.031 ± 0.014
$f_2(1270)\pi^+$	0.850 ± 0.051	3.63 ± 0.15	0.312 ± 0.028
$f_0(1370)\pi^+$	0.934 ± 0.071	2.84 ± 0.15	0.351 ± 0.043
$\rho^0(1450)\pi^+$	0.467 ± 0.048	2.71 ± 0.24	0.088 ± 0.017

10. CONCLUSIONS

10.1 Introduction and Overview

This thesis presented an overview of the E791 experimental apparatus, the data collection and reconstruction methodology, and described the event selection used to extract the final $\pi^+\pi^-\pi^+$ sample from 100% of the E791 data set. A model for the Dalitz plot analysis was presented, and a maximum likelihood fit was performed. From the fit, amplitudes and phases were obtained, and the decay fractions were extracted. Further analysis was performed to investigate statistical and systematic errors.

10.2 Comparison of Results With Published Measurements

Table 10.1 presents a comparison of the results of this thesis with the published results of previous experiments for Dalitz analyses of the decay $D_s^+ \to \pi^+\pi^-\pi^+$.

Comparison with previous results is difficult, because this thesis uses several amplitudes that the previous experiments did not. Conversely, the E687 experiment includes an $\mathcal{S}(1475)$ state that this thesis did not. The E791 and E687 analyses agree in several aspects, however: the lack of a statistically significant non-resonant amplitude and the dominance of the $f_0(980)\pi^+$ mode. E791 and E687 differ in that the measured fraction of $f_0(980)\pi^+$ in E687 is much higher than that obtained in this thesis and that E687 did not observe a statistically significant $\rho^0(770)\pi^+$ contribution. Comparison to the E691 result is also difficult, because in addition to the low statistics and fewer amplitudes in their model, the E691 analysis did not allow interference between the signal amplitudes. Additionally, E691 presented their results in terms of a branching fraction with respect to their well-measured $D_s^+ \to \phi\pi^+$ mode. Errors in the table are statistical only.

Tab. 10.1: Comparison of Thesis Results With Published Measurements

Experiment	Events	Decay Mode	Decay Fraction
E791	1029 ± 82	$f_0(980)\pi^+$	0.430 ± 0.026
		non-resonant	0.011 ± 0.012
		$\rho^0(770)\pi^+$	0.032 ± 0.015
		$f_2(1270)\pi^+$	0.316 ± 0.028
		$f_0(1370)\pi^+$	0.343 ± 0.042
		$\rho^0(1450)\pi^+$	0.085 ± 0.017
E691	65.3 ± 12.0	$\frac{BR(D_s^+ \to f_0(980)\pi^+)}{BR(D_s^+ \to \phi\pi^+)}$	0.28 ± 0.10
		$\frac{BR(D_s^+ \to \pi^+\pi^-\pi^+)_{NR}}{BR(D_s^+ \to \phi\pi^+)}$	0.29 ± 0.09
		$\frac{BR(D_s^+ \to \rho^0(770)\pi^+)}{BR(D_s^+ \to \phi\pi^+)}$	< 0.08 (90% C.L.)
E687	97.9 ± 12.2	$f_0(980)\pi^+$	1.070 ± 0.140
		non-resonant	0.121 ± 0.115
		$\rho^0(770)\pi^+$	0.023 ± 0.027
		$f_2(1270)\pi^+$	0.123 ± 0.056
		$\mathcal{S}(1475)\pi^+$	0.274 ± 0.114

10.3 Final Remarks

The fit to the $D_s^+ \to \pi^+\pi^-\pi^+$ Dalitz distribution assuming a model with Breit-Wigner amplitudes for the two-body resonance modes and a constant for the three-body non-resonant channel reproduces the features of the final data sample. The final fit indicates that 43% of the $D_s^+ \to \pi^+\pi^-\pi^+$ decay width is due to the $f_0(980)\pi^+$ decay. If the $f_0(980)\pi^+$ indeed has a large $s\overline{s}$ component, this result indicates the importance of the W-radiation amplitude diagramed in Figure 1.1c. The lack of a statistically significant non-resonant amplitude and the small $\rho^0(770)\pi^+$ and $\rho^0(1450)\pi^+$ contribution (the $\rho^0\pi$ contributions total about 10% of the total decay width), taken by themselves, are evidence that the contributions from the W-annihilation amplitude (Figure 1.1a and 1.1b) are small. However, if it is correct to assume that the $f_0(1370)$ state is a $u\overline{u}+d\overline{d}$ state [5], the combination of the $\rho^0\pi$ contribution with the measured fraction of the $f_0(1370)\pi^+$ (fit to be 34% of the total decay width) indicates that the W-annihilation and the W-radiation diagrams are approximately equivalent in importance. Finally, if the $u\overline{u}+d\overline{d}$ interpretation of the $f_0(1370)$ state is correct, comparison of the $f_0(1370)\pi^+$ and the $\rho^0\pi$ contributions would indicate that the W boson prefers to couple to scalar rather than to vector particles in the W-annihilation amplitude.

In addition to the contribution to the on-going study and interpretation of the scalar particle resonances, this thesis presents results that further constrain the masses and widths of two scalar resonances that were previously relatively poorly measured. The fit values and previously published values are contrasted in Table 10.2.

Tab. 10.2: Presentation of the $f_0(980)$ and $f_0(1370)$ Mass and Width

Resonance	mass (GeV/c^2)		width (MeV/c^2)	
	previous	new fit	previous	new fit
$f_0(980)$	980 ± 10	974 ± 4	40–100	44 ± 5
$f_0(1370)$	1000-1500	1442 ± 20	200–500	167 ± 32

BIBLIOGRAPHY

[1] R. Dalitz. *Phil. Magazine*, 44:1068, 1953.

[2] R. Dalitz. *Physical Review*, 94:1046, 1954.

[3] M. Wirbel M. Bauer, B. Stech. *Zeitschrift für Physik C*, D 36:103, 1987.

[4] M. Diakonou and F. Diakonos. *Physics Letters*, B 216:436, 1989.

[5] Particle Data Group, Caso, et al. Review of Particle Physics. *The European Physical Journal C*, 3, 1998.

[6] C. Amsler et al. High statistics study of $f_0(1500)$ decay into $\eta\eta$. *Physics Letters B*, B 353:571, 1995.

[7] D. Morgan and M.R. Pennington. New Data on the $K\overline{K}$ Threshold Regions and the nature of the $f_0(S^*)$. *Physical Review D*, 48:1185, 1993.

[8] N. Tornqvist, "Understanding the Scalar Meson $q\overline{q}$ Nonet", Univ. of Helsinki Research Institure for High Energy Physics Report Series HU-SEFT-R-1995-05.

[9] N. Tornqvist and M. Roos. *Physical Review Letters*, 76:1575, 1996.

[10] K.L. Au et al. *Physical Review D*, page 1633, 1987.

[11] R. Jaffee. *Physical Review D*, page 267, 1977.

[12] N. Isgur J. Weinstein. *Physical Review D*, page 2336, 1990.

[13] E691 Collaboration, J.C. Anjos, et al. Study of the Decay D_s and $D^+ \to \pi^-\pi + \pi+$ and $\rho\pi^+$. *Physical Review Letters*, 62:125, 1989.

[14] E687 Collaboration. Analysis of the D^+,$D_s^+ \to \pi^+\pi^-\pi^+$ Dalitz Plot. *Fermilab-pub-97/045-E*, 1997.

[15] H. Fenker. A Standard Beam PWC for Fermilab. Technical Report TM-1179, Fermilab, 1983.

[16] P.E. Karchin et al. Test Beam Studies of a Silicon Microstrip Vertex Detector. *IEEE Transactions on Nuclear Science*, NS-32:612, 1985.

[17] J. Dinkel et al. Fermilab Ziptrack Aparratus. *Nuclear Instruments and Methods*, A138:567, 1976.

[18] D. Bartlett et al. Performance of the Cherenkov Counters in the Fermilab Tagged Photon Spectrometer Facility. *Nuclear Instruments and Methods*, A260:55, 1987.

[19] V.K. Bharadwaj et al. A Large Area Liquid Scintillation Multiphoton Detector. *Nuclear Instruments and Methods*, 228:283, 1985.

[20] D.J. Summers. Reconstruction of a Strip Geometry Calorimeter Using Stepwise Regression. *Nuclear Instruments and Methods*, 228:290, 1985.

[21] J.A. Appel, P.M. Mantsch, M.M. Streetman, and R.M. Robertson. Hadron Calorimetry at the Fermilab Tagged Photon Spectrometer Facility. *Nuclear Instruments and Methods*, A243:361, 1986.

[22] S. Amato et al. The E791 Parallel Architecture Data Acquisition System. *Nuclear Instruments and Methods*, A324:535, 1992.

[23] Phillips Scientific, 305 Island Rd., Mahwah, New Jersey 07430, USA.

[24] C. Rush, A. Nguyen and R. Sidwell, Dept. of Physics, The Ohio State University, personal communication.

[25] LeCroy Research, 700 Chestnut Ridge Rd., Chestnut Ridge, NY 10977, USA.

[26] Nanometric Systems, 451 South Park Blvd., Oak Park, IL 60302, USA.

[27] M. Bernett and others, "FASTBUS Smart Crate Controller Manual", Fermilab Technical Document HN96 (1992).

[28] S. Bracker, "Description of the Damn Yankee Controller (DYC)", E791 Internal Document.

[29] M. Purohit, Dept. of Physics, Princetonn University, "Princeton Scanner/Controller Manual", E791 Internal Document.

[30] S. Hanson et al. Fermilab Smart Crate Controller. *IEEE Transactions on Nuclear Science*, NS-34:1003, 1987.

[31] T. Sjöstrand. PYTHIA 5.7 and JETSET 7.4 Physics and Manual. Technical Report CERN-TH.7112/93, CERN, 1995.

[32] H.-U. Bengtsson and T. Sjöstrand. High-energy-physics event generation with PYTHIA 5.7 and JETSET 7.4. *Computer Physics Communications*, 82:74, 1994.

[33] S. Bracker, K. Gounder, K. Hendrix, and D. Summers. A Simple Multiprocessor Management System for Event-Parallel Computing. *IEEE Transactions on Nuclear Science*, NS-43:2457, 1996.

[34] C. Stoughton and D.J. Summers. Using Multiple RISC CPUs in Parallel to Study Charm Quarks. *Computers in Physics*, 6:371, 1992.

[35] F. Rinaldo and S. Wolbers. Loosely Coupled Parallel Processing at Fermilab. *Computers in Physics*, 7:184, 1993.

[36] Kevin Stenson. *A Study of D^0 Production from 500 GeV Pion–Nucleon Interactions.* PhD thesis, University of Wisconsin – Madison, 1997.

[37] L. Lyons. *Statistics for Nuclear and Particle Physicists.* Cambridge University Press, 1985.

[38] C. Zemach. Use of Angular Momentum Tensors. 140:97, 1965.

[39] C. Zemach. Determination of the Spins and Parities of Resonances. 140:109, 1965.

[40] J. M. Blatt and V. F. Weisskopf. *Theoretical Nuclear Physics.* John Wiley & Sons, New York, 1952.

[41] K. Kajantie E. Bycling. *Particle Kinematics.* John Wiley & Sons, New York, 1973.

[42] F. James and CN/ASD Group. MINUIT - *Function Minimization and Error Analysis – Reference Manual,* Version 94.1. CERN, 1994. CERN Program Library D506.